TECHNISCHE UNIVERSITÄT
CHEMNITZ

Zwillingspolymerisation in Gegenwart von Übergangsmetallen

von der Fakultät der Naturwissenschaften
der Technischen Universität Chemnitz genehmigte

Dissertation

zur Erlangung des akademischen Grades

doctor rerum naturalium
(Dr. rer nat.)

vorgelegt von Diplom-Chemiker **Christian Schliebe**
geboren am 20.03.1986 in Wolfen

eingereicht am:	21.05.2015
Erstgutachter:	Prof. Dr. Heinrich Lang
Zweitgutachter:	Prof. Dr. Stefan Spange
Tag der Verteidigung:	07.09.2015

Bibliographische Beschreibung und Referat

Zwillingspolymerisation in Gegenwart von Übergangsmetallen
Technische Universität Chemnitz, Fakultät für Naturwissenschaften, Dissertation 2015, 152 Seiten, 59 Abbildungen,7 Tabellen

Die vorliegende Arbeit befasst sich mit der Inkorporation von Metall-/ Metalloxidnanopartikeln in organisch-anorganischen Hybridmaterialien, dargestellt durch Zwillingspolymerisation. Des Weiteren wurden die Verkapselung von Silber- und Goldnanopartikeln in porösen Kohlenstoffhohlkugeln mittels Zwillingspolymerisation untersucht.

Es wird gezeigt, dass durch Verwendung von Triphenylphosphan-stabilisierten Silber(I)-carboxylaten eine Funktionalisierung von Zwillingspolymeren möglich ist. Außerdem sind aus den so modifizierten Hybridmaterialien nach Karbonisierung sowie dem Herauslösen der anorganischen SiO_2-Komponete entsprechende mikroporöse, silberhaltige Kohlenstoffmaterialien zugänglich, während durch oxidativen Abbau der organischen Polymermatrix mesoporöse mit Ag-Nanopartikeln infiltrierte SiO_2-Materialien dargestellt werden können. Darüber hinaus konnte eine Vielzahl von neuen Zwillingsmonomeren dargestellt und charakterisiert werden. Darunter finden sich Zirkonium- und Hafnium-haltige Verbindungen, die analog der bekannten Si-Zwillingsmonomere ein ähnliches Polymerisationsverhalten zeigen und durch Copolymerisation mit diesen, ZrO_2- und HfO_2-haltige SiO_2-Mischoxide ergeben. Ebenso war die Synthese von paramagnetischen, porösen Kohlenstoffen sowie superparamagnetischen porösen Silika-Materialien durch Verwendung von Ferrocen-haltigen Zwillingsmonomeren möglich. Es konnten auch entsprechende Pyrrol-basierte Siliziumalkoxide dargestellt werden, welche ein stark verändertes Polymerisationsverhalten zeigen, wie z.B. eine thermisch initiierte Zwillingspolymerisation ab 93 °C. Ebenso konnte gezeigt werden, dass das Einbringen von Stickstoff als Heteroatom in den resultierenden porösen Kohlenstoff ermöglicht wird.

Stichworte: Zwillingspolymerisation, Zwillingsmonomere, Hybridmaterialen, Metall- / Metalloxidnanopartikel, poröse Materialien, Magnetismus, Kohlenstoffhohlkugeln

Ort und Zeitraum der Durchführung

Die vorliegende Arbeit wurde im Zeitraum von November 2011 bis März 2015 unter der Leitung von Prof. Dr. Heinrich Lang am Lehrstuhl für Anorganische Chemie der Technischen Universität Chemnitz durchgeführt.

Herrn Prof. Dr. Heinrich Lang danke ich für die gewährten Freiheiten bei der Bearbeitung dieses Themas, die Bereitstellung der Laboreinrichtung, sowie für das mir entgegengebrachte Vertrauen.

Für meine Eltern und Großeltern

„Live long and prosper“

L.Nimoy † 2015

Inhaltsverzeichnis

Abkürzungsverzeichnis

4-NP	4-Nitrophenol
Abb.	Abbildung
Bu	Butyl-Rest (C_4H_9)
CP	Cross Polarization (Kreuzpolarisation)
Cp	Cyclopentadienyl (η^5-C_5H_5)
CV	Cyclovoltammetrie
d	Doublett
DEPT	Distorsionless Enhancement by Polarisation Transfer
DFG	Deutsche Forschungs Gemeinschaft
DSC	Differential Scanning Calorimetry (dynamische Differenzkalorimetrie)
ε	Extinktionskoefizient
EA	Elemental Analysis
ESI-MS	Electron Spray Ionisation Massspectrometry
Et	Ethyl (C_2H_5)
Fc	Ferrocenyl (Fe(η^5-C_5H_4)(η^5-C_5H_5))
FWHM	Full Width at Half Maximum (Halbwertsbreite)
HAADF-STEM	High Angle Annular Dark Field Scanning TEM
HCS	Hollow Carbon Sphere (Kohlenstoffhohlkugel)
IR	Infrarot
IS	Isomer Shift
*i*Pr	*iso*-Propyl (C_4H_9)
IUPAC	International Union of Pure and Applied Chemistry
IVCT	Inter Valence Charge Transfer
λ	Wellenlänge
m	Multiplet
MAS	Magic Angle Spinning
MB	Methylenblau
Me	Methyl (CH_3)
ν_{as}	asymetrische Valenzschwingung
ν_s	symmetrische Valenzschwingung
NIR	Nahes Infrarot

NMR	Nuclear Magnetic Resonance (Kernspinresonanz)
PA6	Polyamid 6
pd	Pseudo-Doublett
PMMA	Polymethylmethacrylat
PEO	Polyethylenoxid
PFA	Polyfurylalkohol
PP	Polypropylen
PS	Polystyrol
PSA	Polysalicylalcohol
pt	Pseudo-Triplett
QS	Quadrupole Splitting
REM	Rasterelektronenmikroskop
ROM	Ringöffnungsmetathese
s	Singulett
SBS	2,2‘-Spiro-bi[4H-1,3,2-benzodioxasiline]
SPR	Surface Plasmon Band
SQUID	Superconducting Quantum Interference Device (supraleitende Quanteninterferenzeinheit)
t	Triplett
TEM	Transmissionselektronenmikroskopie
TFOS	Tetrafurfuryloxysilan
TG	Thermogravimetrie Analyse
TG-MS	Thermogravimetrie gekoppelte Massenspektrometrie
TMS	Tetramethylsilan ($SiMe_4$)
TTMS	Tetrakistrimethylsilylsilan ($Si(SiMe_3)_4$)
UV	Ultraviolet
UV-Vis	Ultraviolett-Visible
vgl.	vergleiche
XPS	X-Ray Photoelectron Spectroscopy (Röntgenphotoelektronen-spektroskopie)
XRPD	X-Ray Powder Diffraction (Röntgenpulverdiffraktometrie)
z. B.	zum Beispiel

Abbildungsverzeichnis

Tabbellenverzeichnis

Präambel

Die im Rahmen dieser Dissertation erhaltenen Ergebnisse wurden z. T. vorab in internationalen referierten Fachzeitschriften veröffentlicht und bilden, in englischer Sprache, den Hauptteil dieser Arbeit. Die zugrundeliegenden Manuskripte wurden unter fachlicher Anleitung von Prof. Dr. H. Lang selbstständig erstellt. Im Folgenden sind die betreffenden Artikel einzeln aufgeführt:

- **3.1 A convenient light initiated synthesis of silver and gold nanoparticles using a single source precursor**
  C. Schliebe, K. Jiang, S. Schulze, M. Hietschold, W.-B. Cai, H. Lang, *Chem. Commun.* **2013**, *49*, 3991–3993.
- **3.2 Twin Polymerization: A Unique and Efficient Tool for Supporting Silver Nanoparticles on Highly Porous Carbon and Silica**
  C. Schliebe, T. Gemming, L. Mertens, M. Mehring, H. Lang, *Eur. J. Inorg. Chem.* **2014**, 3161–3163.
- **3.3 Zirconium and Hafnium Twin Monomers for Mixed Oxides**
  C. Schliebe, T. Gemming, L. Mertens, M. Mehring, A. Seifert, S. Spange, H. Lang, *ChemPlusChem*. **2015**, *80*, 559–567.
- **3.4 Metal Nanoparticle-loaded Porous Carbon Hollow Spheres by Twin Polymerization**
  C. Schliebe, T. Graske, T. Gemming, L. Mertens, H. Lang, *J. Mater. Chem. A*. **2015**, submitted.
- **3.5 $Si(OCH_2Fc)_4$: Synthesis, Electrochemical Behavior and Twin Polymerization**
  C. Schliebe, U. Pfaff, T. Gemming, C. Lochenie, B. Weber and H. Lang, *J. Organomet. Chem.* **2015**, submitted.
- **3.6 Nitrogen-containing Porous Carbon Materials by Twin Polymerization**
  C. Schliebe, J. Noll, T. Gemming, A. Seifert, S. Spange and H. Lang, *ChemPlusChem* **2015**, in preparation.

Das folgende Buchkapitel entstand ebenfalls während der Promotionszeit, ist aber nicht Bestandteil dieser Arbeit:

- Inkjet Printing of Group-11 Metal Structures (Buchkapitel). C. Gäbler, C. Schliebe, D. Adner, T. Blaudeck, A. Hildebrandt und H. Lang, Nova Science Publishers, Hauppauge, N. Y. (USA), in Comprehensive Guide for Nanocoatings Technology, Volume 1: Deposition and Mechanism, 2015, im Druck. ISBN: 978-1-63482-447-7.

Der im Kapitel 2 aufgeführte Kenntnisstand soll grundlegende Begrifflichkeiten zu den Themen Hybridmaterialien, poröse Kohlenstoffe und Zwillingspolymerisation erörtern, während weiterführende Literatur zu den einzelnen behandelten Themengebieten in Kapitel 3 jeweils an deren Anfang diskutiert wird.

1 Einleitung

Neue leistungsfähige Materialien sind der Grundstein für den anhaltenden Fortschritt unserer Gesellschaft. Die moderne Polymerchemie hat seit ihren Anfängen in den 1920er[2] Jahren des letzten Jahrhunderts ein rasantes Wachstum vollzogen.[1] Die gezielte Forschung nach neuen Polymeren und vor allem deren industrielle Produktion hatten und haben einen großen Einfluss auf unsere Epoche. Die vorteilhaften Eigenschaften wie zum Beispiel die plastische Verformbarkeit und die daraus resultierende gute Verarbeitbarkeit trugen zu diesem Siegeszug maßgeblich bei.

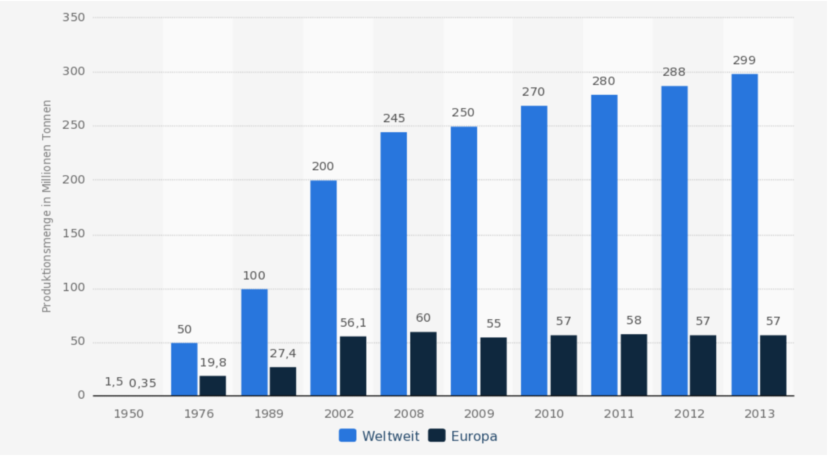

Abbildung 1.1 Weltweite und europaweite Entwicklung der Kunststoffproduktion.[1]

Dennoch stoßen die heutigen Polymere an ihre Grenzen und die Suche nach neuen leistungsfähigeren Werkstoffen stellt einen immer größer werdenden Trend in der Polymerforschung und Materialwissenschaft dar. Dabei geht es zumeist um die positive Verknüpfung von Stoffeigenschaften, so dass die resultierenden Komposite aufgrund von synergistischen Effekten leistungsfähiger als die Einzelkomponenten werden.[3] Ein Beispiel, das aus dem alltäglichen Leben nicht mehr wegzudenken ist, sind Glasfaser-verstärkte Kunststoffe (GFK). Bei diesen Materialien werden anorganische Glasfasergewebe mittels Epoxidharz laminiert und nach dem Aushärten erhält man leichte und schlagfeste Werkstoffe.[3] Während in diesem Beispiel die anorganische Komponente üblicherweise in einer makroskopischen Größenordnung verwendet wird, kann diese aber auch auf der Nanometerskala eingebracht werden. Die daraus resultierende Homogenisierung beider Komponenten hat einen noch stärkeren Einfluss auf die späteren Stoffeigenschaften.[4] Dabei ist es sogar möglich neben den klassischen Werkstoffkenngrößen auch weitere Funktionen einzuführen, die z. B. eine elektrische Leitfähigkeit, nicht linear optisches Verhalten oder eine bessere biologische Verträglichkeit erzielen.[5] Die Vernetzung von organischen und anorganischen Komponenten auf einer Nanometerebene kann auch zur Darstellung hoch geordneter poröser Materialien dienen.[6] Dabei werden Siliziumalkoxide, vorzugsweise mit langen Alkansubstituenten verwendet, die in einem polaren Medium zur Mizellenbildung neigen und so als Nanotemplat fungieren. Nach deren Kondensation wird ein mesoporöses hoch geordnetes Silikamaterial erhalten.[6] Die so zugänglichen Materialien können wiederum mit Kohlenstoff-reichen Polymeren beschichtet werden und nach Karbonisierung und dem Entfernen das mesoporösen anorganischen Templates erhält man die entsprechenden porösen Kohlenstoffmaterialien.[7] Neben diesen etablierten Verfahren entwickeln sich immer wieder leistungsfähige Methoden, wie zum Beispiel die Zwillingspolymerisation. Dabei entstehen aus einem Zwillingsmonomer organisch-anorganische Hybridmaterialien die aufgrund ihrer einzigartigen Struktur als Ausgangspunkt für die Darstellung von porösen Kohlenstoffen oder Siliziumdioxiden genutzt werden können.

Die hier vorliegende Arbeit befasst sich zum einem mit der Funktionalisierung von Zwillingspolymeren mit Übergangsmetallen. Dabei werden geeignete Silber(I)-carboxylate schon während des Zwillingspolymerisationsprozeses eingeführt und erzeugen nach Karbonisierung bzw. Oxidation die entsprechenden Metallnanopartikel in den porösen Systemen (SiO_2 und Kohlentoff). Neben diesem binären Ansatz wird auch an Hand des Ferrocens gezeigt, wie neue Zwillingsmonomere dargestellt und charakterisiert werden und deren Verwendung als metallhaltige Zwillingsmonomere diskutiert. Des Weiteren wurden neue Zr-/Hf-basierte Monomere dargestellt, um die Palette der zugänglichen Oxide zu erweitern und Einblicke in das Polymerisationsverhalten dieser Verbindungen zu erhalten. Es wurden ebenfalls Pyrrol-basierte Monomere synthetisiert, um den Eintrag von Stickstoff als zusätzliches Donoratom für die Stabilisierung von Metallnanopartikeln in der porösen Kohlenstoffmatrix zu ermöglichen.

2 Kenntnisstand

2.1 Organisch/anorganische Hybridmaterialien

Die Klassifizierung von Hybridmaterialien kann auf unterschiedlichen Wegen vollzogen werden. Dabei können wie von Judeinstein und Sanchez vorgeschlagen, die entsprechenden Komposite aufgrund der Bindung zwischen anorganischer und organischer Phase in Materialgruppen erster und zweiter Klasse unterteilt werden.[4] Zur Klasse I zählen alle Komposite, bei denen keine direkte kovalente Bindung zwischen der organischen und anorganischen Komponente besteht. Es werden lediglich schwache Wechselwirkungen (z. B. H-Brückenbindungen) zwischen beiden Komponenten beobachtet. Im Gegensatz dazu finden sich in Hybridmaterialien der Klasse II kovalente Bindungen zwischen beiden Phasen.[4,8] Eine weitere mögliche Klassifizierung wird von Gomez-Romero vorgeschlagen. Dabei steht die Wirt-Gastbeziehung zwischen der organischen und anorganischen Phase im Vordergrund. Demnach spricht man von einem organisch/anorganischen Hybridmaterial, wenn eine anorganische Gastkomponente in einer organischen Matrix eingebracht wird, bzw. beschreibt ein anorganisch/organisches Hybridmaterial den entgegengesetzten Fall.[9]
Aufgrund der hohen Anzahl von organisch-anorganischen Hybridmaterialien[10] stellen diese Klassifizierungen nur zwei Beispiele da und können in anderen Bereichen unter Umständen durch effektivere Prinzipien ergänzt werden.[11] Das Gleiche gilt für die im Folgenden gezeigten Syntheseverfahren und zugänglichen Materialien der hier vorgestellten Systeme. Diese sind als Beispiele zu betrachten um einzelne Prinzipen zu erläutern.

2.1.1 Hybridmaterialien der Klasse I

2.1.1.1 Schichtsilikate in Polymerschmelzen

Die Darstellung von Klasse I Materialien kann unter Verwendung von sogenannten Schichtsilikaten (Abb.: 2.1.1) erfolgen. Um die Einlagerung eines unpolaren Polymeres in diese Matrix zu ermöglichen, müssen zuerst die beweglichen Kationen, welche sich zwischen den Silikatschichten befinden, ausgetauscht werden, denn sie tragen zur starken Hydrophilie dieser Systeme bei.[12] Als geeignete Austauschkationen werden quaternäre Ammoniumsalze verwendet, die über entsprechend große und unpolare Alkylreste verfügen.[13] Die so hydrophobierten Schichten können anschließend durch Mischen mit z. B. einer Polymerschmelze voneinander getrennt werden.[14] Dabei ist die Größe des verwendeten Organokations entscheidend für den erzielbaren Delaminierungsgrad der einzelnen Schichten. Sterisch fordernde Ammoniumverbindungen trennen dabei die einzelnen Silikatschichten stärker und demnach ist auch die zu erreichende Dispersion der anorganischen Phase (Abb.: 2.1.1) größer.[15–17]

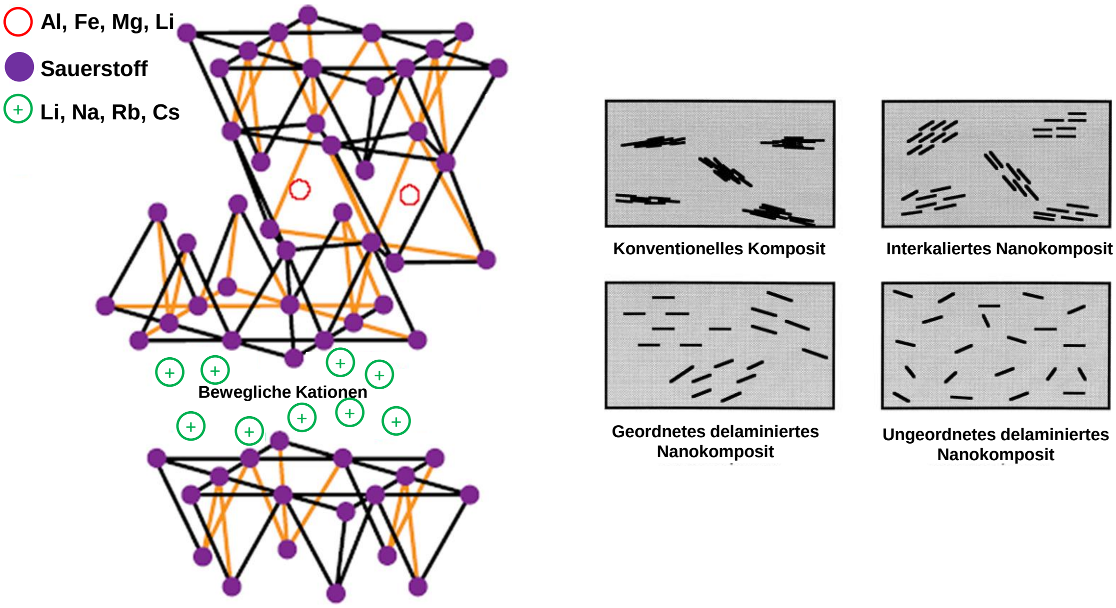

Abbildung 2.1.1 Links: Schematische Darstellung eines Schichtsilikates.[12] Rechts: Mögliche Polymer-Schichtsilikatsysteme.[17]

Diese Vorgehensweise lässt sich auf verschiedenste Schichtsilikate anwenden, wobei Montmorillonit, Hectorit und Saponit zu den am besten studierten Systemen gehören.[15] Neben einer Vielzahl von anorganischen Substraten wurden auch verschiedenste Polymere wie z.B. PP,[18] PS/PEO,[13,19] PA6[20] und Epoxidharze[21] erfolgreich eingesetzt. Die erzielten Hybridmaterialien zeigen, dass die mechanischen Eigenschaften der entsprechenden Nanokomposite die der reinen Polymere übersteigen.

2.1.1.2 Anorganisch-organische Hybridmaterialien im Sol-Gel-Verfahren

Anorganisch-organische Hybridmaterialien sind auch über Sol-Gel-Verfahren[22] zugänglich, dabei werden organische Polymere eingesetzt um Schrumpfungsverluste während des Trocknens auszugleichen.[23] Zwischen den beiden Phasen existieren im Idealfall keine kovalenten Wechselwirkungen und sind demnach ebenfalls der Klasse I zuzuordnen. Der Eintrag der Polymere kann auf verschiedenen Wegen erfolgen. Die Gruppe um Scherer *et al.* nutzte eine ethanolische Lösung von Polyethyloxazolin als Reaktionsmedium für einen Sol-Gel-Prozess und konnte so entsprechende Hybridmaterialien erzeugen. Die erhaltenen Komposite weisen keinen Glasübergangspunkt mehr auf, da das eingebrachte SiO_2-Netzwerk keine Beweglichkeit der Polymerkomponente mehr zulässt.[24] Neben dem Einsatz von Polymerlösung ist es auch möglich Monomere in ein Sol-Gel-System einzubringen und diese entsprechend zu polymerisieren. Auf diese Weise konnten SiO_2-Aerogele dargestellt werden, die *in situ* mit einem PMMA-Polymer stabilisiert wurden.[25] Im Gegensatz dazu können monolithische, optisch transparente Materialien durch Einbringen von Acrylaten[26] oder Acrylat/Styrol[27] Mischungen erhalten werden. Die benötigen Monomere können während des Sol-Gel-Prozesses beigefügt oder aus speziellen bifunktionellen Monomeren durch Hydrolyse erzeugt werden. Darunter versteht man Siliziumalkoxide deren organische Substituenten durch polymerisierbare Gruppen ersetzt wurden (Abbildung 2.1.2).[4]

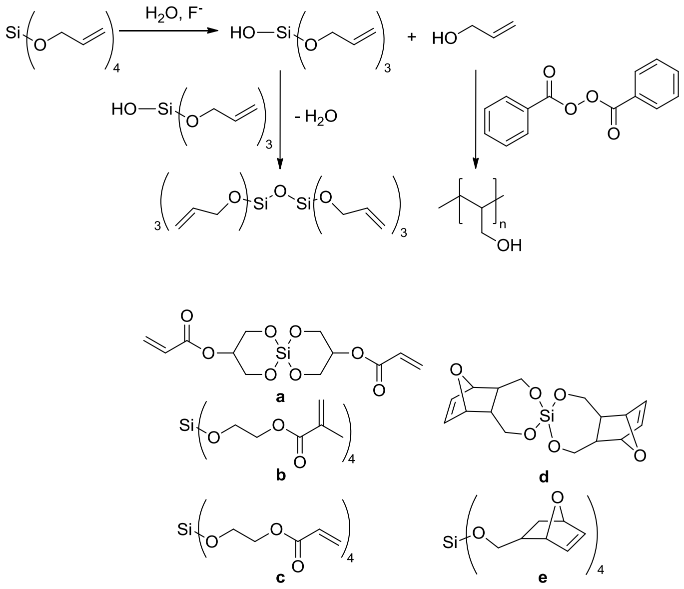

Abbildung 2.1.2. Reaktionsschema zur Polymerisation von bifunktionellen Monomeren und eine Auswahl von möglichen organischen Monomeren.[28–30]

Die Polymerisation der anorganischen Komponenten läuft nach den Prinzipien des Sol-Gel-Prozesses ab und wird unter Zugabe von Fluorid und Wasser initiiert[28] (Abb.: 2.1.2), während sich die Wahl des Initiators oder Katalysators für die organischen Komponente nach der angestrebten Polymerisationsart richtet. So können Vinyl-Substituenten unter Zugabe von Radikalstartern (vgl. Abb.: 2.1.2 **a**-**c**) polymerisiert werden,[30] aber auch die Verwendung von Ru-Katalysatoren die eine ROM-Polymerisation[31] (vgl. Abb.: 2.1.2 **d** und **e**) initiieren, ist möglich. Wie bei den zuvor beschrieben Methoden werden auch hier optisch transparente monolithische Materialien erhalten, welche nur ein geringes Schrumpfungsverhalten während der Trocknung zeigen.

2.1.2 Hybridmaterialien der Klasse II

2.1.2.1 Funktionalisierung von Schichtsilikaten

Die kovalente Verknüpfung zwischen der organischen und anorganischen Phase ist ein elementares Strukturmerkmal von Hybridmaterialien der Klasse II.[4] Demnach muss die anorganische Komponente über geeignete funktionelle Gruppen auf der Oberfläche verfügen, um eine Anbindung der organischen Phase zu erleichtern. Dabei können z. B. Si-OH Gruppen genutzt werden, wie sie häufig auf Schichtsilikaten anzutreffen sind.[12] Eine Funktionalisierung kann durch Umesterung mit Alkyl- oder Aryltrialkoxysilanen erfolgen, dabei werden die einzelnen Silikatschichten getrennt und delaminiert.[32,33] Mithilfe dieser Methode lassen sich nicht nur einfache Alkyl- oder Arylsubstituenten einführen, es können auch zusätzliche Funktionalitäten über eine Alkoxysilan-Verknüpfung eingebracht werden. Dies konnte von Wheeler *et al.* gezeigt werden, indem ein Aminopropyldimethylethoxysilan verwendet wurde. [34] Durch die zusätzlich eingeführten NH_2-Gruppen auf den Schichtsilikaten ist eine weitere Derivatisierung möglich. Dabei waren die Autoren in der Lage eine Vielzahl unterschiedlichster Endgruppen anzuknüpfen, wodurch die universelle Anwendbarkeit dieser Methode unterstrichen wird (Abb.: 2.1.3).

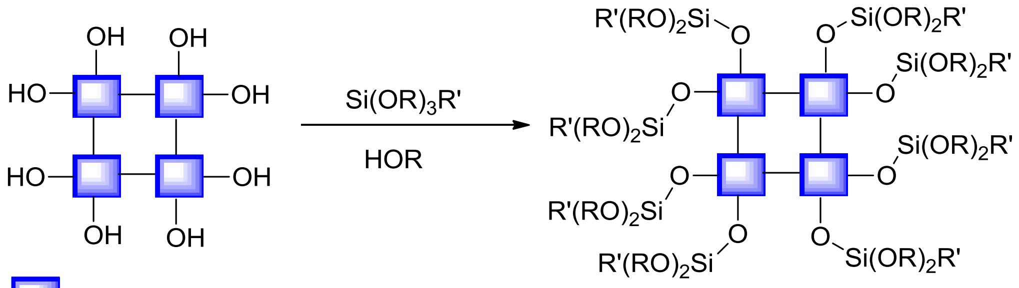

🟦 anorganische Phase

R = Me, Et

R' = Alkyl, Aryl

Abbildung 2.1.3. Schematischer Ablauf zur Darstellung eines Klasse II Hybridmaterials ausgehend von einer anorganischen Phase (z. B. Schichtsilikat).

2.1.2.2 Kovalent verknüpfte Alkoxysilane

Neben der Funktionalisierung von Schichtsilikaten sind Hybridmaterialien der Klasse II alternativ auch über einen Sol-Gel-Prozess zugänglich. Dabei werden zwei Trialkoxysilane mit einer organischen Brücke verknüpft (Abb.: 2.1.4).

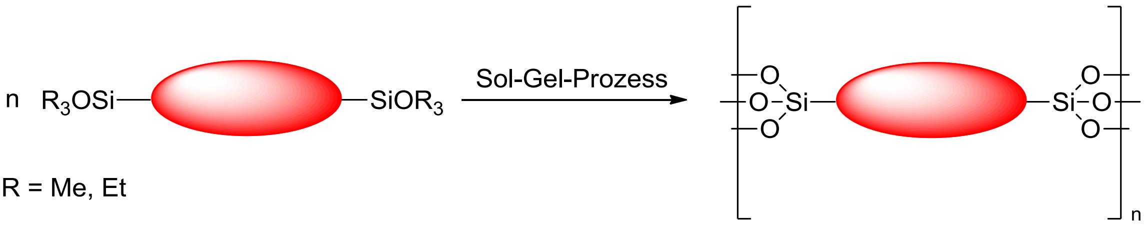

R = Me, Et

⬮ organischer Platzhalter

Abbildung 2.1.4. Schematische Darstellung zur Synthese von Klasse II Hybridmaterialien durch Funktionalisierung von Alkoxysilanen. [35]

Wird diese Verbindung nun einem Sol-Gel-Prozess unterzogen kondensieren die $SiOR_3$-Gruppen, während die verbrückende organische Komponente, z. B. Alkylketten, zur weiteren Quervernetzung beiträgt.[35] Durch dieses Verfahren sind mesoporöse Xerogele mit Oberflächen zwischen 200-700 m^2/g zugänglich. Alternativ können zur Verknüpfung auch aromatische Platzhalter eingesetzt werden, wobei mesoporöse Xerogele mit deutlich höheren Oberflächen von bis zu 960 m^2/g, erhalten werden.[36] Funktionelle Brückenbausteine, wie zum Beispiel 1,3-Butadiin, konnten von Corriu *et al.* mit Trimethoxysilan-Endgruppen modifiziert werden. Die so funktionalisierten 1,3-Butadiine wurden in einem Sol-Gel-Prozess umgesetzt, aus dem entsprechende Xerogele mit Oberflächen von rund 470 m^2/g hervorgehen.[37] Durch anschließende thermische Nachbehandlung konnte gezeigt werden, dass die eingeführten Butadiingruppen polymerisierbar sind und sich somit eine zusätzliche Quervernetzung der organischen Phase erzeugen lässt.

Monolithische Materialien, die den Hybridmaterialien der Klasse II zugeordnet werden können, lassen sich auch durch Ringöffnungspolymerisation von Silaoxocyclopentanen[38] erzeugen. Dabei verknüpften Rahimian *et al.* jeweils zwei dieser Heterozyklen mit einer aromatischen und aliphatischen Brücke.[39] Nach Basen-induzierter Ringöffnungspolymerisation wurden flexible Hybridmaterialien aus der Alkyl-verbrückten Spezies erhalten, während die aromatischen Komponenten dem Komposit zu einem spröderen Habitus verhelfen. Durch Kombination beider Monomere waren Hybridmaterialien der Klasse II mit unterschiedlichen Glasübergangstemperaturen zugänglich.

2.2 Poröse Kohlenstoffmaterialien

2.2.1 Aktivkohlen

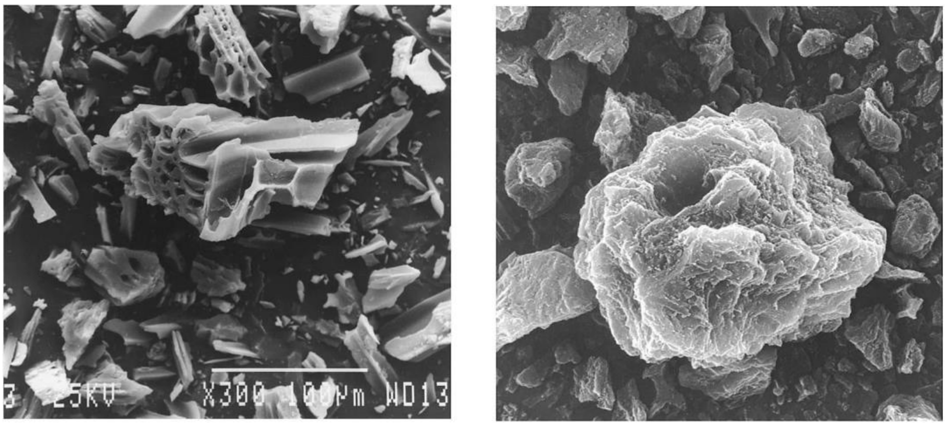

Abbildung 2.2.1. Rasterelektronenmikroskopische Abbildung von Aktivkohlepartikeln dargestellt aus Holz (links) und Torf (rechts).[40]

Aktivkohlen können sehr einfach aus einer Vielzahl von pflanzlichen oder tierischen Materialien hergestellt werden.[41] Dabei hängt der makroskopische Habitus sehr stark vom verwendeten Ausgangstoff ab, wie in Abbildung 2.2.1 verdeutlicht ist.[40,42] Dazu werden die gewünschten Rohstoffe als erstes unter Luftabschluss thermisch karbonisiert und anschließend aktiviert.[43] Dies kann zum Beispiel mit Wasserdampf[44] sowie hohen Temperaturen oder auch auf chemischem Weg mit dem Zusatz von Phosphorsäure[45] oder phosphorhaltigen Verbindungen geschehen.[46] Um den Einfluss der verschiedenen Aktivierungsmethoden auf die zu erzielende Oberfläche zu verstehen, ist es wichtig, immer ein und dieselbe Biomasse als Ausgangstoff zu verwenden. Denn aufgrund von unterschiedlichen Texturen oder Zusammensetzungen können die erzielbaren Resultate beeinflusst werden (vgl. Abb.: 2.2.1). Dazu haben Rambabu *et al.* sich mit den pflanzlichen Rückständen der Rapsölproduktion befasst.[47] Der nach dem Karbonisieren bei 500 °C erhaltene Rohstoff wurde mit Dampf- bzw. CO_2-Aktivierung oder chemischen Methoden (KOH- und NH_3-Aktivierung) behandelt. Dabei ergaben sich durch Aktivieren mittels Wasserdampf spezifische Oberflächen von 403 m^2/g, während 320 m^2/g durch die Behandlung mit CO_2 erhalten wurden. Durch Aktivierung mit Ammoniak konnte keine nennenswerte Steigerung der spezifischen Oberfläche im Vergleich zum karbonisierten Ausgangsmaterial beobachtet werden (19 m^2/g). Im Gegensatz dazu bewirkt der Einsatz von Kaliumhydroxid eine enorme Steigerung der spezifischen Oberfläche (1230 m^2/g). Dies erklären die Autoren damit, dass während der Reaktion Kalium gebildet wird, welches sich zwischen die einzelnen Graphitlagen interkaliert und diese dann von einander getrennt werden.[48] Neben biologischen Ausgangsmaterialien können aber auch kohlenstoffreiche Polymere (z. B. Phenolharze) eingesetzt werden. Dies bringt den Vorteil, das stets die gleiche Morphologie der resultierenden Kohlenstoffe erhalten wird.[49]

2.2.2 Kohlenstoffmaterialien durch Templat-assistierte Verfahren

Wie im Abschnitt 2.2.1 gezeigt werden konnte, ist die Kontrolle der Porengeometrie[42] in der Darstellung von Aktivkohlen schwierig. Demnach werden entsprechende Füllstoffe, welche als Templat fungieren, benötigt. Es wird zwischen Endo-Templaten und Exo-Templaten unterschieden. Endo-Template sind Füllstoffe (z. B. SiO_2-Partikel[50], Ag-Nanopartikel[51] oder Übergangsmetalloxidnanopartikel[52]), die komplett von der organischen Matrix umschlossen werden. Bei Exo-Templaten werden interne Hohlräume (z. B. mesoporöses Silika[53]) mit einer organischen Phase gefüllt.[54] Des Weiteren lassen sich die Template noch weiter in sogenannte Weich- und Harttemplate unterteilen (Abb.: 2.2.2).[53,55]

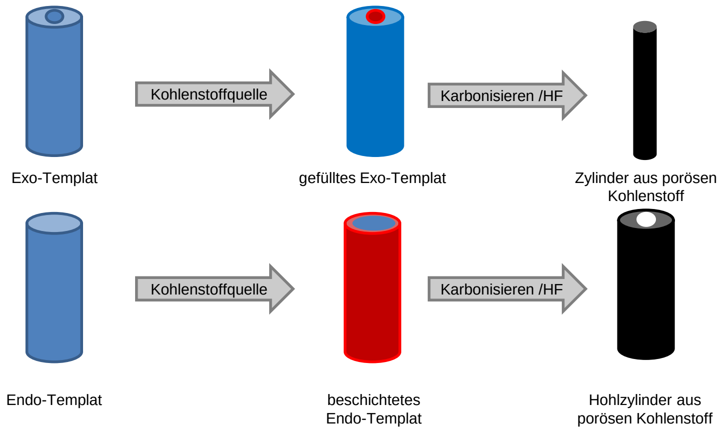

Abbildung 2.2.2. Schematische Darstellung zur Verwendung von Exo- bzw. Endo-Templaten.

Ein Beispiel für ein Weichtemplat ist Pluronic®, ein Poloxamer welches als nichtionisches Tensid in polaren Solventien Mizellen ausbildet, die zum Beispiel in ein Phenolharz eingebettet werden können.[56] Nach vollendeter Polymerisation, des Phenolharzes, werden monolithische Materialien erhalten, die nach dem Karbonisieren einen entsprechenden mesoporösen Kohlenstoffmonolith mit spezifischen Oberflächen von 400–500 m^2/g ergeben. Unter ähnlichen Bedingungen konnte auch gezeigt werden, dass sich Übergangsmetallkomplexe wie z. B. Eisen(III)-hexacyanoferrat(II/III) in entsprechende Materialien einbauen lässt und nach dem Karbonisieren Eisen(III)-oxid Nanopartikel erzeugt werden.[57] Ein weiteres polymeres Weichtemplat sind Polystyrollatex Partikel.[58] Dabei wurde eine wässrige Lösung bestehend aus Phenolharz und Latexpartikeln in einen Rohrofen gesprüht, in dem ein Temperaturgradient von 150-1000 °C herrscht. Am Anfang des Ofens, im Niedertemperaturbereich, wird das Lösungsmittel verdampft, wobei die Phenolharz/Latexpartikel-Tröpfchen aushärten. Im sich anschließenden Hochtemperaturbereich kommt es zur Karbonisierung der Polymertröpfchen. Hier wird auch das Weichtemplat entfernt und am Ende dieser Prozesse werden Kohlenstoffpartikel, die über eine hexagonale dichtgepackte Porensturktur verfügen, isoliert.

Ein häufig verwendetes Harttemplat ist das mesoporöse Siliziumdioxid SBA-15. Um seine Struktur in einer Kohlenstoffmatrix abzubilden, muss es mit einer Kohlenstoffquelle beschichtet werden, wofür meist Phenolharze[59] oder Polyfurfurylalkohol[60] verwendet werden. Nach dem Beschichten wird die organische Matrix karbonisiert und dann im Anschluss das SiO_2-Templat mit Flusssäure entfernt. Die so erhaltenen mesoporösen Kohlenstoffe weisen spezifische Oberflächen zwischen 1100–1720 m^2/g auf.[59] Diese lassen sich durch chemische Aktivierung mittels KOH (vgl. Abschnitt 2.2.1) noch steigern und so können bis zu 2660 m^2/g erzielt werden.[59]

Neben mesoporösen SiO_2-Templaten finden auch Siliziumdioxidschäume Verwendung (Abb.: 2.2.2).[61] Hierbei wird zuerst eine Kohlenstoffquelle in Form von Phenolharzen aufgebracht, die dann anschließend karbonisiert wird. Durch Herauslösen des Templates mittels Flusssäure sind poröse monolithische Kohlenstoffmaterialien mit spezifischen Oberflächen zwischen 459–802 m^2/g möglich.

2.3 Zwillingspolymerisation

2.3.1 Zwillingspolymerisation von siliziumhaltigen Zwillingsmonomeren

Unter der Zwillingspolymerisation versteht man die Bildung von organischen/anorganischen Hybridmaterialien aus einem einzelnen Monomer und unter Zusatz eines einzigen Initiators. Erstmalig wurde dieses Verhalten bei der Umsetzung von Tetrafurfuryloxysilan unter sauren Bedingungen beobachtet (Abb.: 2.3.1).[62] Dabei bildet eine Acidolyse den initialen Schritt, wobei eine SiOH-Gruppe, sowie ein Carbokation gebildet werden. Nun können zwei getrennte Reaktionswege durchlaufen werden. Zum einem können die Silanolgruppen kondensieren und bilden demnach ein SiO_2-Netzwerk aus. Dabei wird Wasser freigesetzt, das die weitere Verseifung der Furfuryloxysiloxangruppen katalysiert. Dadurch werden Furfurylalkoholmoleküle generiert, die mit vorhandenen Carbokationen die Polyfurfurylalkohol (= PFA) Komponente bilden. Am Ende dieses Prozesses wird ein Hybridmaterial bestehend aus Siliziumdioxidnanoclustern, welche in einer PFA-Matrix eingebettet sind, erhalten.

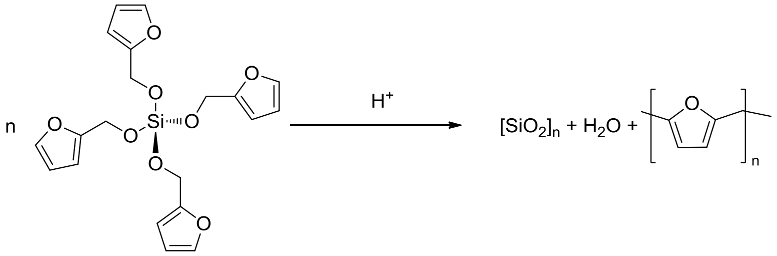

Abbildung 2.3.1. Säure-initiierte Zwillingspolymerisation von Tetrafurfuryloxysilan.[62]

Mittels Festkörper-NMR-Spektroskopie wurde die Identität der organischen Phase nachgewiesen, während für die anorganische Komponente ein hoher Vernetzungsgrad unter den einzelnen SiO_2-Einheiten gefunden wurde. Ebenso konnte mit Hilfe der $^{29}Si\{^1H\}$-CP-MAS NMR Spektroskopie das Fehlen entsprechender Resonanzsignale für das SiO-R (R = Furfuryloxy) Strukturmotiv gezeigt werden. Daraus wurde geschlussfolgert, dass zwischen organischer und anorganischer Komponente keine Verknüpfung kovalenter Natur mehr vorliegt. Um diesen Befund mit experimentellen Daten zu untermauern, wurde die analoge Verbindung Difurfuryloxydimethylsilan synthetisiert und unter gleichen Bedingungen polymerisiert. Dabei kam es zu einer Phasenseparation zwischen der organischen und anorganischen Phase, womit die fehlende Verknüpfung zwischen beiden belegt werden kann und demnach die erhaltenen Hybridmaterialien der Klasse I zuzuordnen sind.

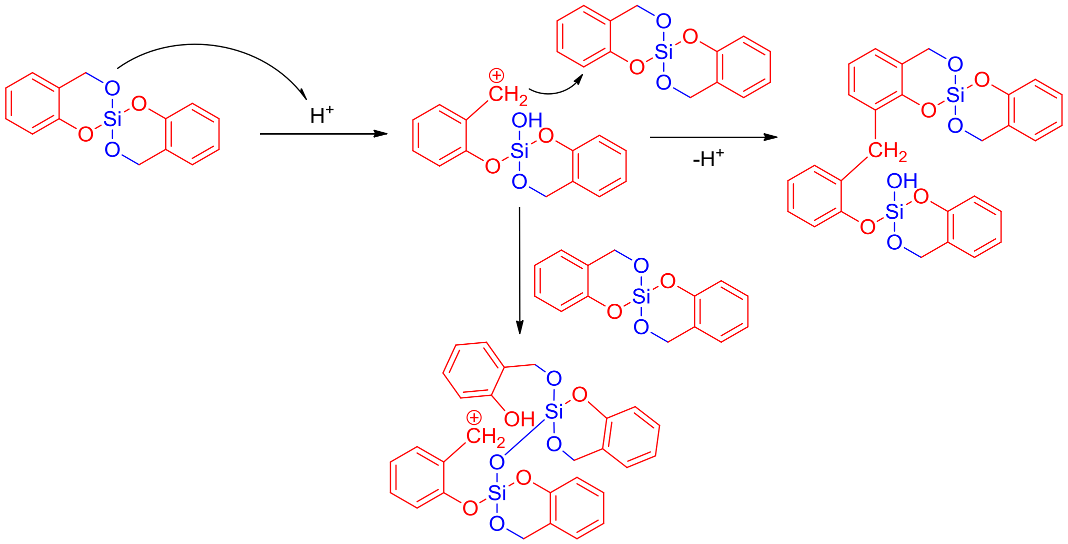

Abbildung 2.3.2. Ablauf der Säure-initiierten Zwillingspolymerisation am Beispiel des SBS.

Eine weitere Verbindung, die das Zwillingspolymerisationsverhalten zeigt, ist 2,2‘-Spirobi[*4H*-1,2,2-benzodioxasilin] (= SBS).[63] Eine Besonderheit dieser spirozyklischen Verbindung ist der verwendete Salicylalkohol. Aufgrund der phenolischen und benzylischen Hydroxyfunktion ergeben sich unterschiedliche Reaktivitäten, anders als bei den symmetrischen, analogen Verwandten Bis(*o*-phenylendioxy)silan[64] oder 3,3‘-Spirobi[2,4-dioxa-1,2,4,5-tetrahydro-*3H*-3-benzosilepin].[65] Einen Einfluss auf die Reaktivität, aufgrund des asymmetrischen Substitutionsmuster, konnte von Spange *et al.* gezeigt werden. Quantenchemische Berechnungen zeigen, dass die Ringöffnung an einer benzylischen Hydroxygruppe als initiierender Schritt benötigt wird. Ein erster experimenteller Beweis wurde durch gezieltes Umsetzen von SBS mit Trimethylsilyliodid erbracht. Mittels der ^{1}H-, ^{13}C{^{1}H}- und ^{29}Si{^{1}H}-NMR-Spektroskopie konnte die selektive Ringöffnung beobachtet werden. Das selbe Verhalten wurde auch für die analoge Verbindung 2,2-Dimethylbenzo-2-sila-1,3-dioxan[66–68] beobachtet. Eine weitere Derivatisierung und damit einhergehende Stabilisierung des Ringöffnungsproduktes war durch Reaktion der erhaltenen Benzyliodidspezies mit aprotischen Nukleophilen möglich. Aufgrund dieser Erkenntnis kann die Säure-initiierte Zwillingspolymerisation mechanistisch nachvollzogen werden (Abb.: 2.3.2).

Eine weitere Besonderheit ist die thermische Polymerisierbarkeit von SBS.[69] Wird diese Verbindung auf 230 °C erhitzt, so wird eine exotherme Reaktion mittels DSC beobachtet. Dabei kommt es analog der Säure initiierten Reaktion ebenfalls zu Ringöffnung des spirozyklischen Systems an einer benzylischen Hydroxygruppe. Der weitere Reaktionsverlauf konnte jedoch nicht umfassend geklärt werden, da quantenchemische Untersuchungen einen zwitterionischen Zustand prognostizieren. Dieser konnte bis jetzt noch nicht mit experimentellen Ergebnissen bewiesen werden. In weiterführenden Arbeiten wurde gezeigt, dass eine Substitution am aromatischen System mit Elektronen-schiebenden bzw. -ziehenden Substituenten einen Einfluss auf die Initiierungstemperatur der Zwillingspolymerisation hat.[70] Werden demnach in *meta*-Position substituierte SBS-Derivate eingesetzt, so zeigt sich, dass mit steigenden Hammett-Konstanten die nötige Polymerisationstemperatur herabgesetzt wird. Derselbe Trend wird auch beobachtet, wenn dem System eine Protonenquelle (z.B. $MeSO_3H$) beigemischt wird.

2.3.1.1 Poröse Materialien aus siliziumhaltigen Zwillingspolymeren

Wie im Abschnitt 2.3.1 gezeigt wurde, entstehen bei der Zwillingspolymerisation organisch-anorganische Hybridmaterialien. Die in diesen Kompositen *in situ* gebildete anorganische Phase kann auch als Harttemplat verstanden werden. Durch Karbonisierung wird die organische Komponente in Kohlenstoff umgewandelt, während die anorganische bestehen bleibt und entsprechende Freiräume blockiert.

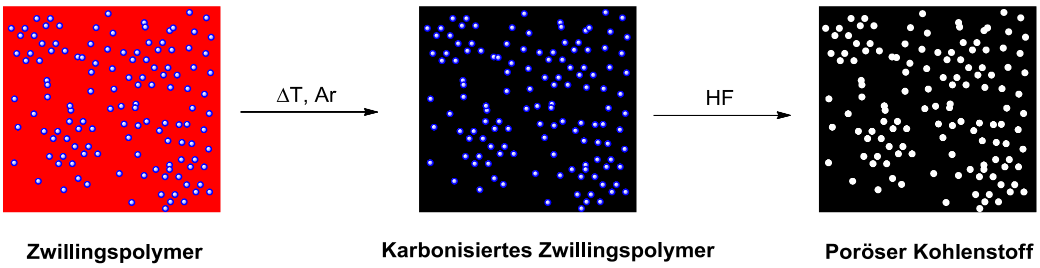

Abbildung 2.3.3. Karbonisierung von Zwillingspolymeren und dem Herauslösen der anorganischen SiO_2-Phase mit HF.

Durch anschließendes Herauslösen der SiO_2-Matrix werden Poren in der Kohlenstoffmaterial gebildet (Abb.: 2.3.3).[63] Dabei hat das verwendete Zwillingsmonomer einen großen Einfluss auf die zugänglichen Oberflächen. Wird zum Beispiel Tetrafurfuryloxysilan (= TFOS) eingesetzt, so sind eher mesoporöse Kohlenstoffe mit spezifischen Oberflächen bis maximal 135 m^2/g zugänglich.[62] Ein anderes Ergebnis wird erhalten, sobald SBS verwendet wird. Das resultierende Hybridmaterial besteht aus einem Phenolharz und SiO_2-Clustern (0.5-2 nm), die als Harttemplat fungieren und bilden nach dessen Herauslösen mit 5 M NaOH oder HF entsprechende Poren.[63] Dabei werden ausschließlich mikroporöse Kohlenstoffmaterialien mit spezifischen Oberflächen von bis zu 1500 m^2/g erhalten.[71] Durch Kombination beider Monomere (TFOS und SBS) konnte gezeigt werden, dass diese nicht copolymerisieren, sich jedoch poröse Kohlenstoffmaterialien darstellen lassen, die sowohl Meso- als auch Mikroporen aufweisen.[72]

Eine weitere Möglichkeit zur Darstellung von porösen Kohlenstoffstrukturen mittels Zwillingspolymerisation besteht in der Beschichtung von Harttemplaten (Abb.: 2.3.4).

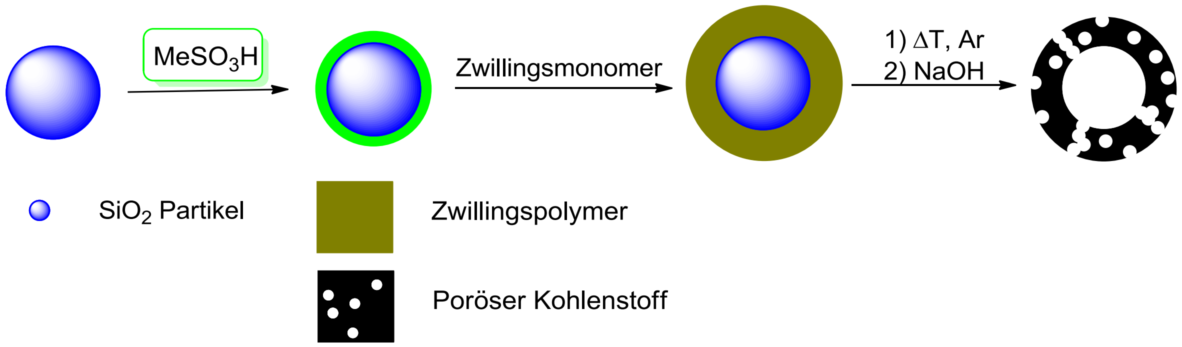

Abbildung 2.3.4. Darstellung von porösen Kohlenstoffhohlkugeln durch Zwillingspolymerisation an Harttemplaten.[73]

Dazu werden zum Beispiel Glasfasern mit SBS oder TFOS beschichtet und dann im Anschluss durch Zwillingspolymerisation mit einer Hülle aus Hybridmaterial umgeben. Die so erhaltenen Komposite werden karbonisiert und nach dem Herausätzen der anorganischen Materialien entsprechende Kohlenstoffhohlzylinder mit spezifischen Oberflächen zwischen 310-510 m^2/g, je nach verwendetem Monomer bzw. Monomerenverhältnis, erhalten.[74] Neben zylindrischen Templaten lassen sich auch sphärische SiO_2-Partikel verwenden. Dazu wird auf der Oberfläche zuerst $MeSO_3H$ aufgebracht, um die so funktionalisierten Template unter Zugabe der entsprechenden Monomere (TFOS, SBS oder beide gemischt) in einer Zwillingspolymerisation mit einer Hülle aus Zwillingspolymer zu beschichten. Nach Karbonisierung und dem Herauslösen der anorganischen Materialien werden poröse Kohlenstoffhohlkugeln erhalten.[73] Dabei konnte durch Variation des Monomerenverhältnisses und der Monomermenge die Schalendicke sowie das Verhältnis zwischen Meso- und Mikroporen beeinflusst werden, während der Durchmesser des Hohlraumes durch die verwendete Templatgröße gesteuert wurde (20 nm–300 µm). Dies unterstreicht noch einmal deutlich die universelle Modifizierbarkeit der durch Zwillingspolymerisation zugänglichen porösen Materialien.

2.3.2 Zwillingsmonomere von Übergangs- sowie Hauptgruppenmetallen (W, Ti, Sn und Ge)

Aufgrund seiner hohen Oxophilie eignet sich Titan ausgezeichnet zur Synthese von entsprechenden Alkoxiden.[75] In Analogie zu den bereits bekannten Silizium-basierten Zwillingsmonomeren (z. B. TFOS) wurden auch entsprechende Titan-haltige Verbindungen dargestellt.[76] Dabei wurde ein chiraler vier-kerniger Titanoxocluster erhalten.[77] Dieser zeigte ein ähnliches Verhalten während der Zwillingspolymerisations wie die Si-Analoga, wobei als anorganische Phase entsprechend TiO_2 gebildet wird. Ein weiterer Unterschied findet sich in der Porosität der anorganischen Titandioxid-Phase. Diese kann durch Oxidation der organischen Matrix isoliert werden und weist eine nur geringe spezifische Oberfläche von 50–100 m^2/g auf. Dabei werden deutlich kleinere Werte erzielt, als die Oberflächen der entsprechenden SiO_2-Materialien, welche aus SBS oder TFOS zugänglich sind (vgl. SiO_2 aus TFOS 250–520 m^2/g; SiO_2 aus SBS 500–900 m^2/g) [62,71].

Eine neue Variante der Zwillingspolymerisation wurde bei der Synthese von Wolfram-haltigen Zwillingsmonomeren beobachtet.[78] Dabei zeigte sich, dass durch Zugabe von WCl_6 zu entsprechenden Arylmethanolen ein Zwillingspolymerisationsprozess ausgelöst wurde, da die für eine Zwillingspolymerisation charakteristischen Hybridmaterialien erhalten wurden. Diese wiesen die für Zwillingspolymere typische Nanostrukturierung und homogene Verteilung der anorganischen Phase auf. Durch Oxidation der organischen Matrix konnte halogenfreies und poröses WO_3 mit einer spezifischen Oberfläche zwischen 50-60 m^2/g isoliert werden.

Neben der Polymerisation von Übergangsmetall-haltigen Zwillingsmonomeren konnten auch Hauptgruppenelemente für die Zwillingspolymerisation nutzbar gemacht werden. Durch Umsetzung von Furfurylalkohol, Thienylalkohol oder verschiedenen Methoxy(methyl)benzylalkoholen konnten entsprechende Zinnalkoxide dargestellt werden.[79] Die dabei erhaltenen Verbindungen weisen z. T. eine polymere Struktur auf. Es wurde beobachtet, dass elektronenreiche Benzylalkohle eher zur Oligomerisierung, als zur Zwillingspolymerisation neigen. Ebenso war es möglich Co-Polymerisate mit SBS zu erhalten. Aus diesen Hybridmaterialien waren poröse SiO_2-Komposite (165-380 m^2/g) zugänglich, die mit SnO_2-Nanopartikeln (20-32 nm) infiltriert waren. Neben Zinn(VI)oxid-Nanopartikeln, die in einer SiO_2-Matrix eingebettet sind, konnten auch poröse Kohlenstoffe dargestellt werden, welche Sn-Nanopartikel enthielten.[80] Dabei wurde durch Copolymerisation zwischen SBS und den entsprechenden Zinnalkoxiden ein Hybridmaterial erhalten, welches unter reduzierenden Bedingungen karbonisiert wurde. Dabei werden poröse Kohlenstoff/Sn/SiO_2 Komposite erzeugt, die einen Zinngehalt von bis zu 40 % aufweisen.

Analog zu den entsprechenden Zinnverbindungen konnte auch mit dem niederen Homologen Germanium entsprechende Alkoxide dargestellt werden, die ein Zwillingspolymerisationsverhalten zeigen.[81,82]

2.4 Synthese und Reaktionsverhalten der Alkoxide von Si, Zr und Hf

Die Synthese von Siliziumalkoxiden kann durch Umsetzen der entsprechenden Alkohole mit Siliziumtetrachlorid erfolgen. So sind die verschiedenen Substitutionsgraden bis hin zum Orthoester zugänglich.[83] Dabei hat der Alkohol einen erheblichen Einfluss auf die ablaufende Reaktion.[84] Werden aliphatische Alkohole verwendet, können die entsprechenden Orthoester erhalten werden. Sobald aber aromatische Substrate mit $SiCl_4$ umgesetzt werden, ergeben sich andere Reaktionsabläufe. Dabei spielt der Abstand des aromatischen Substituenten von der Hydroxyfunktion eine entscheidende Rolle. Werden β-funktionalisierte Alkohole (z. B. 2-Phenylethanol) verwendet, so erhält man die entsprechenden Orthoester. Im Gegensatz dazu, führt der Einsatz von α-substituierten Alkoholen (z. B. 1-Phenylethanol) zur Bildung der entsprechenden Halogenalkane. Triebkraft für diese Reaktion ist eine nukleophile Substitution am α-Kohlenstoff durch HCl. Das für diesen Prozess nötige Carbokation wird im 1-Phenylethanol besser mittels Mesomerie stabilisiert werden, als im 2-Phenylethanol, womit die Reaktion begünstigt wird.[85] Ein wiederum anderes Verhalten zeigt zum Beispiel das Catechol. Wird es im Verhältnis von 1:1 mit $SiCl_4$ umgesetzt, so wird ein Gemisch aus *o*-Phenylendioxidichlorosilan (vgl. Abb.: 2.4.1 **a**), seinem Dimer (vgl. Abb.: 2.4.1 **b**) und der entsprechenden spirocyclischen Verbindung (vgl. Abb.: 2.4.1 **c**) erhalten.[86] Verdoppelt man nun die Menge an Catechol wird hingegen nur **c** gebildet.

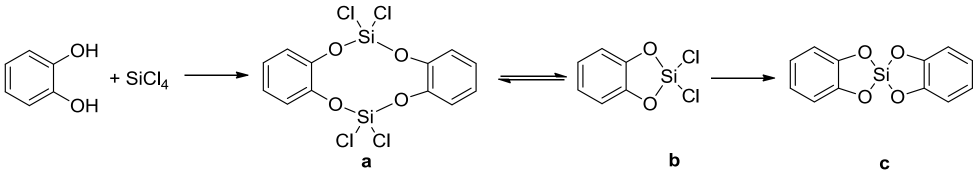

Abbildung 2.4.1. Reaktion von Catechol mit $SiCl_4$ im Verhältnis 1:1.

Eine alternative Darstellungsmethode ist die Umesterung zwischen zwei Siliziumalkoxiden. Da es sich bei dieser Reaktion um ein Gleichgewicht handelt, ist es von Vorteil wenn sich einer der ausgetauschten Alkohole z. B. mittels Destillation abtrennen lässt.[83,87,88] Mit dieser Methode ist es möglich auch sechsfach koordinierte Siliziumalkoxide darzustellen. Dazu wird Tetraethylorthosilikat mit Catechol in Gegenwart einer Stickstoffbase umgesetzt.[89] Die so zugänglichen hypervalenten[90] Siliziumspezies eignen sich als Ausgangsverbindungen für Polyspirosiloxane.

Die Analogen Zr- und Hf-Alkoxide lassen sich ähnlich zum Silizium durch Reaktion von $ZrCl_4$ oder $HfCl_4$ und den gewünschten Alkoholen darstellen. Ebenso ist eine Umesterung möglich.[91] Während Siliziumalkoxide als vierfach koordinierte Verbindungen erhalten werden, sind für Zr und Hf meist sechsfach koordinierte Spezies bekannt, die zusätzlich noch zur Aggregation in Clustern neigen.[92] So liefert die Umsetzung von Catechol mit $ZrCl_4$ oder $HfCl_4$ in Gegenwart von Pyrridin[93], vierkernige Oxocluster.[94] Höher substituierte Zirkoniumoxocluster sind durch Reaktion von Zr(O-*i*Pr)$_4$ und Oximen zugänglich. Dabei werden Koordinationszahlen von bis zu acht erhalten.[95]

Aufgrund des ausgeprägten Koordinationsverhaltens, lassen sich die Zirkonium- und Hafniumalkoxide auch für viele Anwendungen nutzen. So können zum Beispiel unter Verwendung zusätzlicher bidentater Liganden wie z. B. Acetylacetonat und Resorcinol spinnfähige Polymere erzeugt werden.[96] Aber auch als anorganische Vernetzungskomponente in organsichen Polymeren können Zirconiumoxocluster eingesetzt werden.[97] Dazu wird Zr(O-*i*Pr)$_4$ mit Methylmethacrylatanhydrid umgesetzt. Der sich bildende vierkernige Zirkoniumoxocluster kann dann mit Methacrylat copolymerisiert werden. Die so zugänglichen Hybridmaterialien weisen keine Löslichkeit in Ethylacetat mehr auf und auch die thermische Depolymerisation wird je nach Menge der eingesetzten Zirkoniumspezies gehemmt oder gar unterdrückt.

3 Theoretischer Teil

3.1 A convenient light initiated synthesis of silver and gold nanoparticles using a single source precursor

C. Schliebe, K. Jiang, S. Schulze, M. Hietschold, W.-B. Cai and H. Lang

Publiziert in *Chemical Communications* **2013**, *49*, 3991-3993.

Die Synthese und Charakterisierung der in diesem Kapitel veröffentlichten Verbindungen, sowie die Interpretation der erhaltenen Ergebnisse wurden vom Autor durchgeführt. Die photochemischen Zersetzungsversuche selbst wurden von K. Jiang unter Anleitung des Autors ausgeführt. Die Elektronenmikroskopischen Abbildungen hat Dr. S. Schulze angefertigt.

3.1.1 Introduction

Metal nanoparticles are well known for their special and unique optical[98], electronic[99] and catalytic[100] properties. These attributes are size and shape dependent[101] and lead to a versatile variety of applications, for example, in catalysis, optoelectronics and biochemistry.[102] The enormous interest in transition metal nanoparticles also created a vast diversity of protocols for their generation and stabilisation. Mostly, they were synthesised by reacting the corresponding transition metal salt, for example, silver nitrate, a reducing agent and a stabiliser in an appropriate solvent.[103] Therefore, a wide range of reductive reagents were investigated. For example sodium borohydride is used extensively for the preparation of metal nanoparticles. Even environmentally friendly substances like polysaccharides are just one example of a green alternative[104] reducing agent.

An even greener method involves ultra-violet irradiation,[105] as reported by Hartlieb *et al.*[106] Therefore, a metal source and a stabiliser were dissolved in water and irradiated with UV-light to afford nanoparticles. The sensitiveness can be tuned by adding a chromophoric system producing radicals, which are essential for the reduction process.[107,108] Reducing agent-free methods were also established, commonly they involve metal carbonyls, diluted in ionic liquids, which were irradiated with ultra violet light to form nanoparticles.[109–111]

Recently, we have succeeded in synthesizing silver[112] and gold[113] nanoparticles through thermal decomposition of the appropriate metal carboxylate complexes without the addition of a reducing agent and a stabiliser. Here we report a new advanced procedure for the generation of metal nanoparticles using a single source precursor, which combines light sensitive functionalities, a reducing agent and the metal source in one molecule. Bringing these three parts together simplifies the preparation and optimises the efficiency of the whole process. With an “all-in-one” molecule, it is no longer necessary to regulate the amount of reducing source or to control the concentration of silver ions in the nanoparticle forming process. The use of hazardous chemicals can be avoided, too (Scheme 3.1.1).

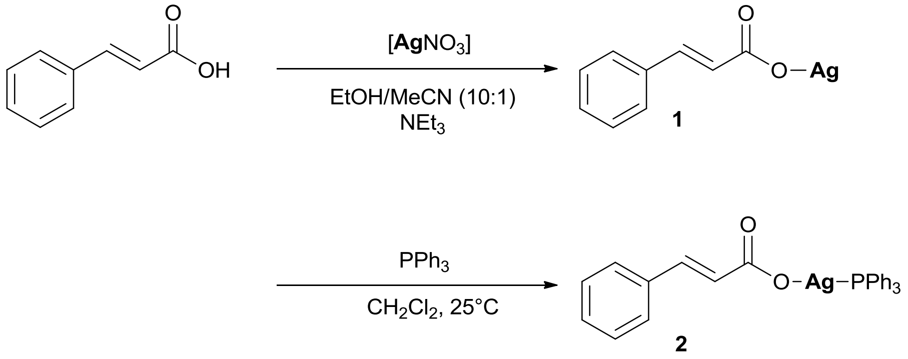

Scheme 3.1.1. Preparation method for [$AgOCH_2$=CHPh] (**2**).

3.1.2 Results and discussion

One class of compounds, which fulfil these requirements, are silver(I) carboxylates. However, due to their low solubility, the corresponding phosphine complexes are used. Silver carboxylates are known for their ability to thermally decompose into elemental silver and their light sensitivity.[114] Photosensitivity can be enormously increased using *α,β*-unsaturated carboxylic acids.[115] Due to the easy accessibility of *E*-cinnamic acid we chose this molecule for first experiments. Another important structural property favouring this acid is the conjugated CH=CHPh *π* unit. This entity acts as a chromophore as well and is situated close to the carboxylic group which is the linking moiety between the silver and the chromophore (Scheme 3.1.1). We were able to synthesise the corresponding silver(I) carboxylates and the respective phosphine complex by applying a modified synthetic methodology (Scheme 3.1.2) first described by Edwards et al.[115]

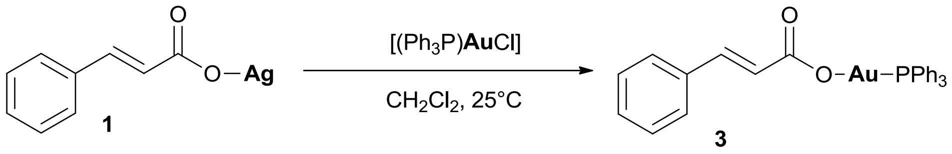

Scheme 3.1.2. Preparation method for [AuOCH$_2$=CHPh] (**3**).

For the decomposition experiments, **2** was dissolved in a mixture of oleic acid and tetrahydrofuran (ratio 1 : 10, *v*/*v*) for stabilising the particles during their generation. The resulting solution was transferred into a quartz glass vial and was irradiated using a standard UV lamp (2 × 8 W, λ = 254 nm and 366 nm) for 60 min. In the course of the reaction, the silver nanoparticles cause a change in the colour of the reaction mixture from colourless to yellow and finally orange, due to their surface-plasmon-resonance band (SPR band). Therefore, irradiation time intervals up to 1 h were used to ensure a complete turnover of **2**. The resulting UV-Vis spectra are shown in Fig. 3.1.1. From this Figure an increasing absorption with a maximum at λ_{max} = 450 nm, belonging to the silver SPR band,[116,117] can be seen, which is indicated by a change in the colour of the reaction mixture from colourless to yellow. After longer exposure to UV light a slight bathochromic shift can be observed (λ_{max} = 458 nm) and the molar absorptivity (ε) increases as well. For exposure times longer than 10 min, formation of a shoulder (λ = 380 nm) close to the main band was detected. After 60 min of irradiation a second shoulder can be observed, which is strongly red shifted. An explanation for this is plasmonic incitation which leads to surface oxidation of the silver nanoparticles with the consequence of formation of smaller and larger particles indicated by blue and red shifted shoulders.[118] A similar result could be observed in the TEM images (Fig. 3.1.1). They show an agglomeration of particles, the majority of which are 10 nm (±5 nm). The appearance of smaller particles (below 10 nm) surrounding the larger structures emphasises the theory of light induced ripening processes. The identity of the nanoparticles was proven using electron diffraction patterns obtained during the TEM measurement, confirming the formation of silver nanoparticles (the diffraction patterns are provided in the ESI).

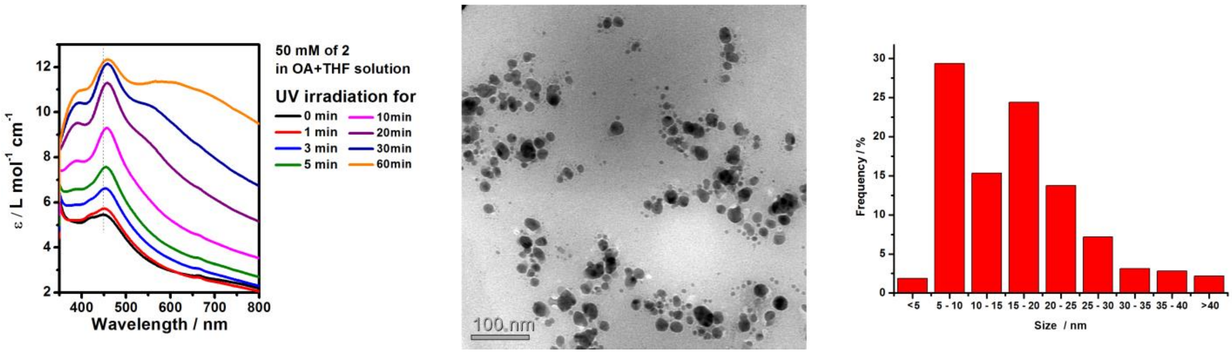

Figure 3.1.1. Left: UV-Vis spectra of **2** (50 mM) in the oleic acid (OA) and tetrahydrofuran (THF) ratio of 1 : 10 (v/v), middle: TEM image of the silver nanoparticles obtained from **2** and right: resulting size distribution (irradiation time: 20 min).

The corresponding compound $[(Ph_3P)AuO_2CCH{=}CHPh]$ (**3**), (Scheme 3.1.2) was also investigated as an “all-in-one” precursor[113] to light induced formation of gold nanoparticles. Gold has the advantage of lower oxophilicity over silver. The decomposition experiments were realised in a similar manner to that used for silver but diglyme was used as a solvent and a stabiliser instead of the oleic acid–THF system. After 15 min of irradiation, the UV-Vis spectra showed the appearance of a new band (Fig. 3.1.2). After prolonged exposure to UV light, the formation of a defined SPR band was observed at λ_{max} = 513 nm.[119] From the TEM image (Fig. 3.1.3) it can be seen that gold nanoparticles were formed. The majority of the particles are below 5 nm in diameter and their identity was proven using electron diffraction (see ESI).

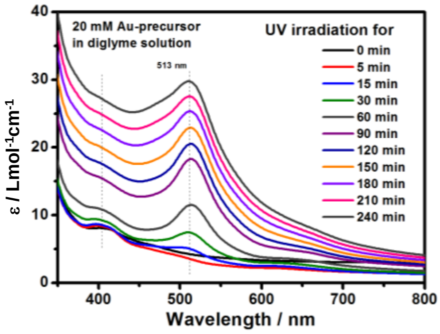

Figure 3.1.2. UV/Vis-spectra of **3** (20 mM in diglyme).

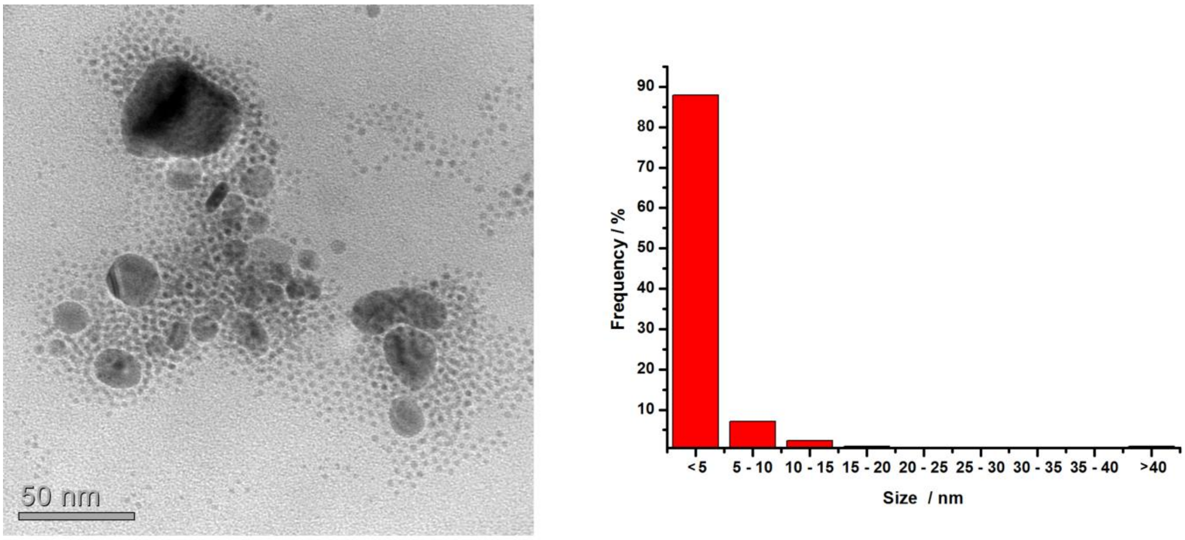

Figure 3.1.3. TEM image of gold nanoparticles obtained from **3** (irradiation time 60 min).

3.1.3 Conclusion

In summary, the feasibility of a light sensitive single-source-precursor which is able to produce metal nanoparticles has been demonstrated. Therefore, the decomposition of **2** [107] was investigated. The structural motifs of $[(Ph_3P)AgO_2CCH{=}CHPh]$ (**2**) were transferred to the appropriate gold(I)–phosphine complex **3** succsessfully. Between the syntheses of appropriate precursors we were able to decompose solutions containing the metal–organic complexes **2** and **3** through irradiation using a low energy UV light source. The resulting solutions were analysed using UV-Vis spectroscopy and TEM studies. Both methods prove the formation of metal nanoparticles from the precursor molecules. The particle sizes are narrowly distributed with the majority in the range of 10 nm (±5 nm) for silver and below 5 nm for gold as well. The advantages of this preparation methodology are that no reducing agents are needed and very mild conditions for nanoparticle formation can be applied. Actually, the introduction of a stabilising moiety at the phenyl ring is in progress, so the addition of an external stabiliser will be superfluous.

3.2 Twin Polymerization: A Unique and Efficient Tool for Supporting Silver Nanoparticles on Highly Porous Carbon and Silica

C. Schliebe, T. Gemming, L. Mertens, M. Mehring and H. Lang

Publiziert in *European Journal of Inorganic Chemistry* **2014**, 3161-3163.

Die Synthese und Charakterisierung der in diesem Kapitel veröffentlichten Verbindungen, sowie die Darstellung der entsprechenden Hybridmaterialien und der daraus resultierenden porösen Komposite wurden vom Autor durchgeführt. Die elektronenmikroskopischen Abbildungen (HAADF-STEM) wurden von Dr. T. Gemming angefertigt und die Abbildungen wurden vom Autor interpretiert. L. Mertens hat die PXRD sowie temperaturabhängigen PXRD Untersuchungen ausgeführt, die Ergebnisse wurden vom Autor interpretiert.

3.2.1 Introduction

During the last decades a vast variety of synthetic protocols for the preparation of porous catalyst supports has been reported.[120] These materials exhibit unique properties, and thus they are employed in a wide range of applications.[40,121–124] Especially as a catalyst support, for example, silver and silver alloys with interesting applications such as oxidation[125–129] and hydrogenation reactions[112,130] or electrooxidation[131–133] in fuel cells have been established. The preparation of these supports can be realized, for example, by carbonization and by activating organic materials to obtain activated carbons.[40] However, one problem associated with this method is the uncontrollable pore geometry and pore-size distribution. To address these topological challenges synthetically sophisticated template methodologies[53,134,135] have been employed. To overcome this topical question, the concept of twin polymerization was applied. This novel approach to microporous carbon and mesoporous silica[62,63,136] benefits from the fact that no external templates are required, as they are in situ generated during the polymerization process. The twin monomers used in this reaction are silicon orthoesters bearing polymerizable organic functionalities. Through reaction of those compounds under acidic conditions or at high temperatures, the organic moieties form an organic polymer and simultaneously the inorganic component creates a silicon dioxide network. During the twin polymerization process, a silicon dioxide template is formed, which interpenetrates the resulting organic material. After thermal treatment of the hybrid material under an inert atmosphere and removal of the inorganic component, a highly microporous carbon material with a narrow pore-size distribution (0.5 to 3 nm) is obtained.[72] Owing to the imbuing networks it is also possible to extract the inorganic template. The formed silicon dioxide is mainly mesoporous and has an inner surface area that is comparable to that of the carbon material.[72] We herein describe the preparation of silver-containing porous compounds by twin polymerization.

3.2.2 Results and discussion

To achieve silver-rich porous materials, we incorporated silver(I) carboxylates[137,138] during the twin polymerization process to achieve a silver-containing hybrid material from which silver-enriched porous carbon or silica materials could be generated. Therefore, the experimental setup depicted in Scheme 1 was applied. Silver(I) carboxylate **1**, derived from thienyl acetic acid, was used as the silver source. The triphenylphosphine ligand is advantageous for increasing the solubility of the silver(I) precursor. For a typical polymerization experiment (for details see the Supporting Information) the appropriate amount of 2,2′-spirobi[4*H*-1,3,2-benzodioxasiline] (**2**) and the silver source (15 mol-%) were diluted in dichloromethane. After warming the reaction mixture to 40 °C, methanesulfonic acid diluted in dichloromethane was added as a catalyst; within seconds the solution became turbid. The hybrid material precipitated, and it was collected and carbonized under an argon atmosphere. The resulting material was then either treated with a refluxing solution of sodium hydroxide to remove the silica template or oxidized to receive the porous inorganic material (Scheme 3.2.1).

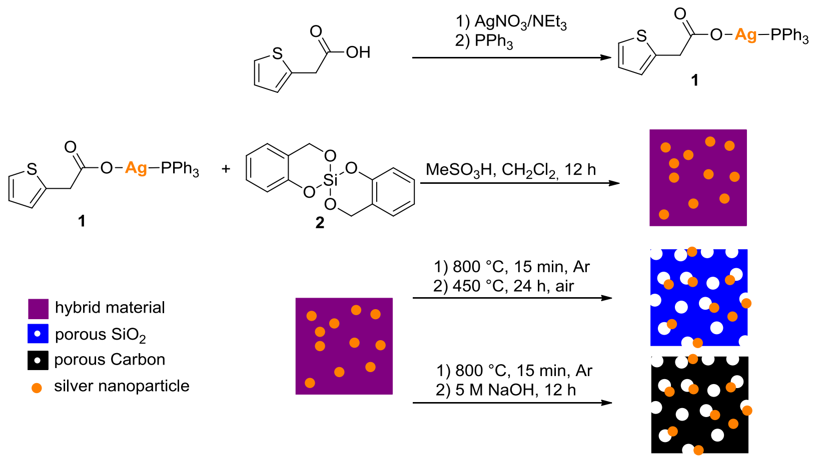

Scheme 3.2.1. Method for the preparation of the appropriate hybrid materials.

To investigate the formation of silver nanoparticles during the polymerization process, X-ray powder diffraction (XRPD) studies of the hybrid material, the carbon component, and the silica network were performed (see the Supporting Information). Nevertheless, the hybrid material did not exhibit the typical reflex pattern of silver, and hence, we conclude that, for example, the silver crystallites are too small to be detected. Upon thermal treatment and appropriate workup, silver could be detected, both in the carbon and in the silica materials. The broad reflex of silver [111] indicates a rather small silver particle size (see the Supporting Information). Temperature-dependent XRPD experiments were performed, which showed typical reflections at 230 °C, and this indicates the beginning of silver grain growth (Figure 3.2.1).

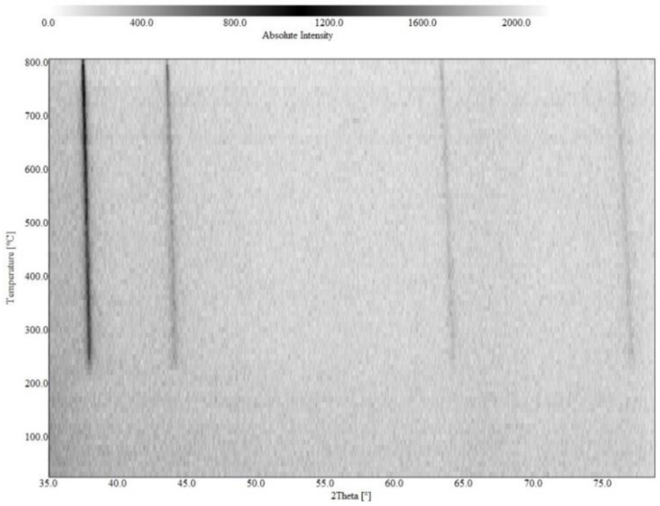

Figure 3.2.1. Temperature-depending XRPD pattern with the evolving reflexes of silver nanocrystals.

From high angle annular dark field scanning transmission electron microscopy (HAADF-STEM) images (Figure 3.2.2), the hybrid material shows the presence of silver nanoparticles. Within this picture the typical grainy structure of the twin polymer can be detected. This pattern belongs to nanometer-sized silicon dioxide clusters,[63] which were formed during the reaction. These clusters also act as a hard template and form the narrow and homogeneous pore structure of the resulting carbon (for pore-size distribution plots see the Supporting Information).[72] As found by XRPD studies, the HAADF-STEM images of the carbon (Ag content ≈ 4 % by energy dispersive spectroscopy (EDX)) and silicon dioxide (Ag content about 9 % by EDX) materials show finely dispersed silver nanoparticles with the majority smaller than 5 nm in diameter. The surface area of the carbon and silica materials was investigated by nitrogen adsorption–desorption isotherms at 77 K. An IUPAC type I[139] isotherm was found for the carbon material, which proves the microporosity of this material with a surface area of 1034 $m^2\,g^{-1}$. For the silica component, a combination of IUPAC type I[139] and type IV isotherms was observed. The pore-size distribution (see the Supporting Information) reveals microporous and mesoporous parts. The hysteresis is caused by interstitial areas from particular overlapping. Density functional theory calculations give a surface area of 666 $m^2\,g^{-1}$ for the silica materials, which points out that the area is slightly smaller than that of the reference materials reported in the literature.[63] Owing to the high surface area, the silver particles are well dispersed and hence sintering at high temperatures is restrained.

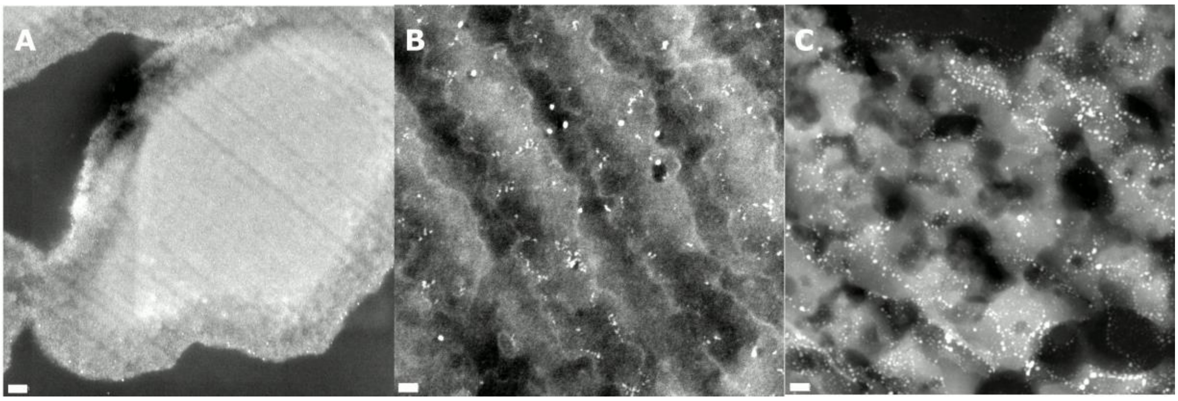

Figure 3.2.2. HAADF-STEM images (high resolution images are provided in the Supporting Information) of the hybrid material (A, 50 nm scale bar), the derived car-

bon component (B, 20 nm scale bar), and the silicon dioxide material (C, 20 nm scale bar).

3.2.3 Conclusions

In summary, we have shown that with the application of the twin-polymerization concept it is possible to generate carbon- or silica-supported metal nanoparticles in a straightforward manner with the benefit of a convenient one-pot procedure involving the twin monomer (2,2′-spirobi[4*H*-1,3,2-benzodioxasiline]) and triphenylphosphine silver(I) thiopheneacetate as precursor systems. After appropriate workup, the desired carbon and silica materials were obtained and investigated by XRPD, HAADF-STEM, and nitrogen adsorption–desorption isotherms. Both materials exhibit highly dispersed silver nanoparticles with a diameter of ≤5 nm, and both materials show unique properties regarding their surface area and pore-size distribution. The carbon component is mainly microporous with a high surface area of 1034 $m^2\,g^{-1}$, whereas the silicon dioxide has a lower surface area (666 $m^2\,g^{-1}$) with a higher mesoporous part. A stabilizing effect of the incorporated silver particles is accompanied with this high inner surface area owing to the high dispersion of silver. The extension of this procedure to other metal carboxylates based on Au, Cu, Pd, Pt, and Rh is in progress. Furthermore, the thus-supported silver nanoparticles will be used in catalytic applications including oxidation, hydrogenation, and isomerization processes.

Supporting Information (see footnote on the first page of this article): General procedures, experimental details, nitrogen absorption–desorption isotherms, XRPD pattern, and HAADF-STEM images.

3.2.4 Acknowledgements

The authors would like to thank the Deutsche Forschungsgemeinschaft (DFG) (FOR 1497) and the Fonds der Chemischen Industrie (FCI) for generous financial support. H. Gnägi (Diatome AG, Biel Switzerland) is thanked for TEM sample preparation.

3.3 Zirconium and Hafnium Twin Monomers for Mixed Oxides

C. Schliebe, T. Gemming, J. Noll, L. Mertens, M. Mehring, A. Seifert, S. Spange and H. Lang

Publiziert in *ChemPlusChem* **2015**, 80, *3*, 559-567.

Die Synthese und Charakterisierung der in diesem Kapitel veröffentlichten Verbindungen, sowie die Diskussion der erhaltenen Ergebnisse wurden vom Autor durchgeführt. Alle abgebildeten Elektronenmikroskopischen Darstellungen (TEM und HAADF-STEM) wurden von Dr. T. Gemming angefertigt und vom Autor interpretiert. Die thermischen Analysen wurden von J. Noll, die XRPD-Experimente von L. Mertens und die Festkörper-NMR-Charakterisierung von A. Seifert angefertigt, wobei die Interpretationen der erhaltenen Ergebnisse vom Autor erfolgte.

3.3.1 Introduction

Zirconium and hafnium oxide gained growing interest during the last years, since they show unique properties and hence opening a wide field of applications. For example, zirconium oxide was either used as co-catalyst for reducing nitric oxides with methane to N_2 and CO_2,[140] or for the oxidation of hydrocarbons in a solid oxide fuel cell[141]. Furthermore, ZrO_2 is used as a catalyst support for stabilizing precious metals like Ru, Rh, Pd or Pt in various catalytic applications[142–144]. Another usage of ZrO_2 is gas sensing as published by Wiemhöfer[145] and Miura[146]. The mixed oxides of zirconium and hafnium with silicon dioxide have been investigated, due to their high-k dielectric properties and were proposed as new gate dielectric compound in microelectronic circuits[147–149]. The preparation of mixed zirconium oxides was broadly investigated, firstly by sol gel methods, utilizing the appropriate metal alcoholate and silicon orthosilicate, respectively. Mixing them and reacting the respective mixture under defined conditions considering, for example, the pH value, catalyst concentration and temperature[150,151], the mixed oxides of type ZrO_2/SiO_2 or $ZrSiO_4$ were obtained depending on the ratio of the Zr and Si source. A different approach for mixed metal oxides is given by using a Laponite clay, which was infiltrated with $ZrOCl_2$ giving porous Zr-doped silicas with a rather high inner surface area (400 – 470 m^2/g, depending on the reaction conditions).[152] In addition, gas phase techniques can be applied to ZrO_2 and HfO_2 formation,[153] enabling these materials for microelectronic applications.

Recently, twin polymerization was introduced by Spange and co-workers which allows the preparation of nano-structured organic-inorganic hybrid materials within one step.[71] This convenient procedure benefits from the strong mechanistic coupling between the formation of the inorganic and organic networks. This methodology involves a silicon orthoester bearing polymerizable organic groups such as 2-furylic alcoholate or salicylic alcoholates[62,63,70,71,154]. By reacting these compounds with an acid (e.g. $MeSO_3H$) or under thermal initiation, reactive sites on the inorganic and organic part of the monomer are formed. Thus the formation of the phenolic resin proceeds faster and hence phase separation of the inorganic SiO_2 is not observed, leading to nano-structured hybrid materials. Both networks can be separated from each other. Oxidizing the hybrid material results in meso-porous silica, while after carbonization and removal of the SiO_2 lattice micro-porous carbon is formed. This concept was recently extended to transition metal-containing monomers from titanium and tungsten[76–78,155] and was also adapted to tin and germanium[79–82]. Herein, we extend the known twin monomers by a series of new Zr and Hf coordination complexes of the type $[M(2\text{-}OCH_2{}^cC_4H_3O)_4(x\ HOCH_2{}^cC_4H_3O)]$ (**3**, M = Zr, x = 0; **4**, M = Hf, x = 1) and $M[(2\text{-}OCH_2\text{-}C_6H_4O)_2(2\text{-}HOCH_2\text{-}C_6H_4OH)]$ (**5**, M = Zr; **6**, M = Hf) as polymerizable and copolymerizable species. In addition, the thermal behaviour of the mixed oxides MO_2/SiO_2 (M = Zr, Hf) is discussed.

3.3.2 Synthesis and characterization of twin monomers

By reacting an excess of 2-furylic alcohol with $M(OR)_4$ (**1**, M = Zr, R = ${}^nC_3H_7$; **2**, M = Hf, R = ${}^nC_4H_9$) (Scheme 1), the zirconium and hafnium complexes $[M(2\text{-}OCH_2{}^cC_4H_3O)_4\ (x\ HOCH_2{}^cC_4H_3O)]$ (**3**, M = Zr, x = 0; **4**, M = Hf, x = 1) were accessible. After subsequent removal of propanol or butanol, which is formed within the latter reactions, a yellow orange sticky material was obtained, which was repetitive precipitated from pentane and then dissolved in toluene and used for the hybrid material synthesis (see below).

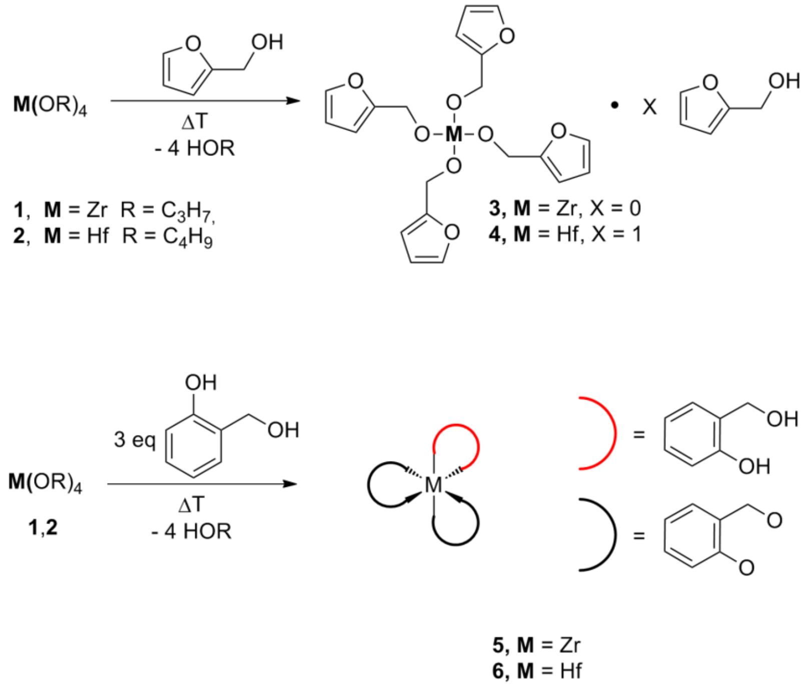

Scheme 3.3.1. Synthesis of zirconium (**3**, **5**) as well as hafnium (**4**, **6**) twin monomers from **1**, **2** and the respective alcohols.

As depicted in Scheme 3.3.1, the Zr and Hf complexes **5** and **6** are accessible in a similar manner as **3** and **4**. Therefore, three equivalents of salicylic alcohol were suspended in toluene and after addition of **1** or **2** the reaction mixture turned yellow. This solution was heated at reflux, while the volatiles were slowly evaporated over 2 h under reduced pressure. The obtained crude material was diluted in dichloromethane, filtered and precipitated from hexane giving a yellow solid.

Metal-organic complexes **3** - **6** were analyzed by ^{1}H and $^{13}C\{^{1}H\}$ NMR and solid state ^{13}C NMR (**5** and **6**) spectroscopy (for detailed information see ESI). However, no single crystals of **3** - **6** could be obtained and hence their molecular structure could not be verified by single crystal X-ray diffraction.

The typical resonance signals of the furylic and salicylic moiety, as compared to the pure alcohols, were observed, but shifted to lower fields. However, due to ligand exchange processes the NMR spectra of **3** - **6** show line broadening. Characteristic in the IR spectra of **3** - **6** is the observation of a $\nu_{O\text{-}H}$ vibration at 3615 cm^{-1}, indicating the presence of furylic (**3** and **4**) or salicylic alcohol (**5** and **6**), clarifying that a further molecule coordinates to the appropriate metal center M (M = Zr (**5**), Hf (**4**, **6**)).[92] This assumption is supported by CHN analysis for **3 - 6**, however, one should notice that Zr- and Hf-orthoesters are able to form clusters or oligomers, when the respective group-IV metal ion reaches a coordination number of 6 or higher.[94,156] Though, the oligomeric nature of the obtained compounds could not be verified by ESI-MS experiments since complexes **3 - 6** could not be ionized under the measurement conditions applied.

3.3.3 Polymerization and characterization of 3 - 6 and the resulting PFA/MO$_2$ and PSA/MO$_2$ (M = Zr, Hf; PFA = polyfurfurylicalcohol, PSA = polysalicylicalcohol) hybrid materials

From **3** and **4** the respective hybrid materials were prepared in toluene at elevated temperature and under addition of 40 mg of trifluromethanesulfonic anhydride ((CF_3SO_2) $_2$O) as initiator. The solution immediately turned dark and the hybrid material **HM3** (= Zr) and **HM4** (= Hf) precipitated. Polymerization of **5** and **6** was achieved by diluting the monomers in dichloromethane, followed by heating to 40 °C and addition of methanesulfonic acid (60 mol-%) as initiator (for detailed information see ESI). The resulting hybrid materials (**HM5** = Zr, **HM6** = Hf) were collected by filtration.

The supernatant solution as, obtained after polymerization of **3** and **4,** was investigated by GC-MS, verifying the formation of compounds which are typical for the cationic polymerization of furylic alcohol to polyfurylic alcohol (= PFA)[157,158] (Table 3.3.1).

Table 3.3.1. Byproducts of the hybrid material synthesis from **3** and **4** determined by GC-MS (GC: solvent = Ethyl acetate, MS: ionization energy = 45 keV).

Compd.	Retention time	M [g/mol]
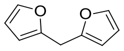	5‘14“	148.16
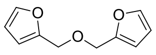	10‘48“	178.18
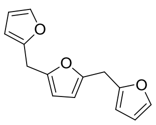	20‘48“	227.23

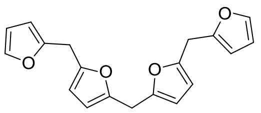	33‘27“	308.32
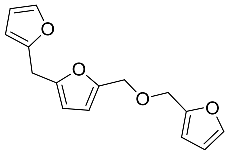	25‘10“	248.26

The as prepared **HM3** and **HM4** materials were investigated by $^{13}C\{^1H\}$ CP-MAS NMR spectroscopy. Figure 3.3.1 shows the corresponding spectrum for **HM3** with the typical signals for PFA[159] (**a**, **b**, **c**, **d**, **f**), as being characteristic for the polymerization of tetrafurfuryloxysilane[62]. The abundance of a rather sharp signal at around 60 ppm, referring to the **C**H_2O**M** group of the monomer, indicates a complete conversion within the hybrid materials.

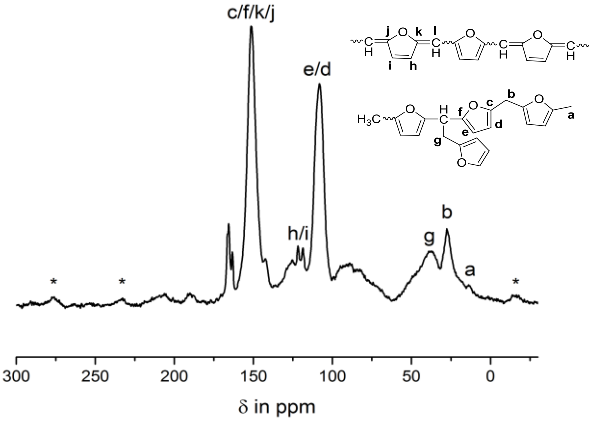

Figure 3.3.1. $^{13}C\{^1H\}$ CP-MAS spectrum of **HM3**. (inset: assignment of signals; 100.6 MHz, 12.5 kHz, * = spinning side bands, reference: tetrakistrimethylsilyl silane = TTSS).

The spectra show some evidence for crosslinking in the polymer (**g**) and also signals for unsaturated dimethylenedihydrofuran species[160]. The signal at 165 ppm can be assigned toring-opening products of the furan moiety. Levulinic acid was also found during the polymerization of tetrafurfuryloxy silane[160]. According to these results, similar spectra were obtained for the PFA/HfO_2 hybrid material **HM4** (ESI). In the solid state NMR spectrum of **HM5** the appropriate signals for a phenolic resin[63] obtained thru twin polymerization are observed (Figure 3.3.3). Signal **c** refers to the Zr-O-CH_2 unit indicating complete conversion of the starting material **5**. This is also emphasized by the strong resonance signal **d**, referring to the linking CH_2 groups within the phenolic resin. In comparison, the $^{13}C\{^1H\}$ CP- MAS NMR spectrum of **HM6** shows a signal of higher intensity for the Hf-O-CH_2 moiety evidencing an incomplete polymerization.

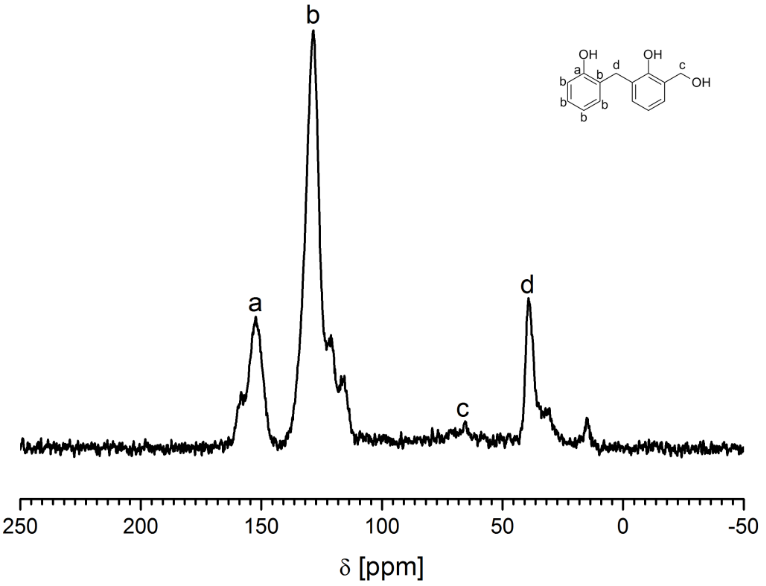

Figure 3.3.2. $^{13}C\{^1H\}$ CP-MAS spectrum of **HM5** (inset: assignment of signals; 100.6 MHz, 20 kHz, reference: TTSS).

3.3.4 Electron microscopy and thermal behaviour of HM3 - HM6

The distribution of the inorganic phase within the hybrid material was investigated by REM/EDX and TEM analysis. The specific REM images and EDX mappings are depicted in Figure 3.3.3. The secondary electron images of **HM3** and **HM4** show mainly spherical particles with an inhomogeneous surface. Identical shapes were reported for the hybrid materials obtained from the polymerization of tetrafurfuryloxy silane[62]. Regarding the EDX mappings a homogenous distribution of Zr or Hf is indicated. They are foreclosing a macroscopic phase separation, due to a higher amount of the inorganic component. The materials **HM5** and **HM6** are unveiling a similar behavior with the same distribution of Hf or Zr over the whole sample.

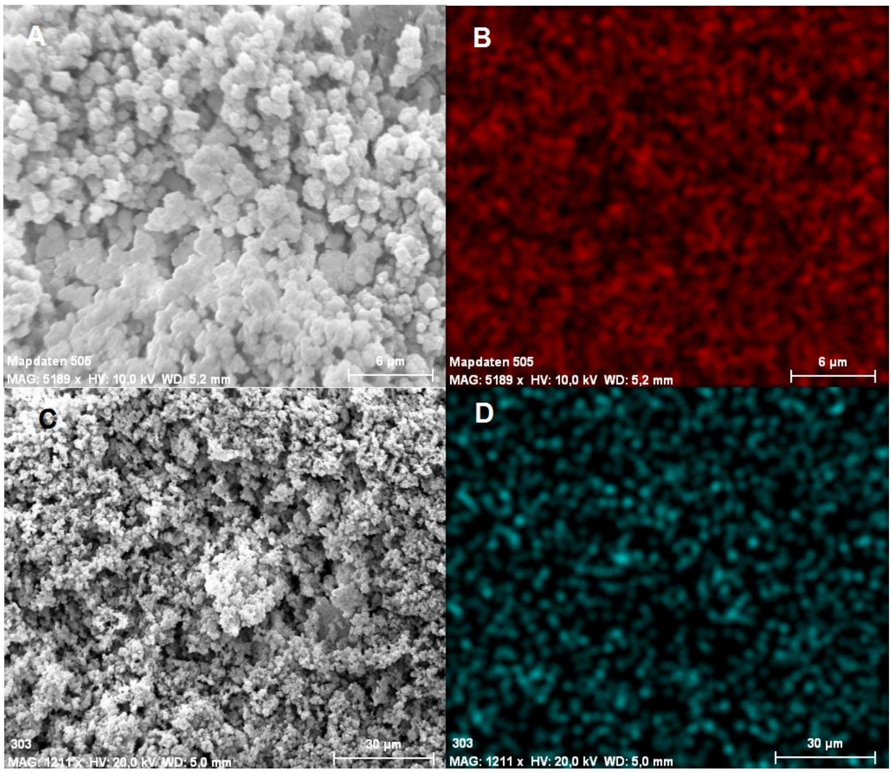

Figure 3.3.3. REM images and EDX mappings of **HM3** (A and B, red = Zr, 10 kV) and **HM4** (C and D, turquoise = Hf 20 kV) (for images and mappings of **HM5** and **HM6** see ESI).

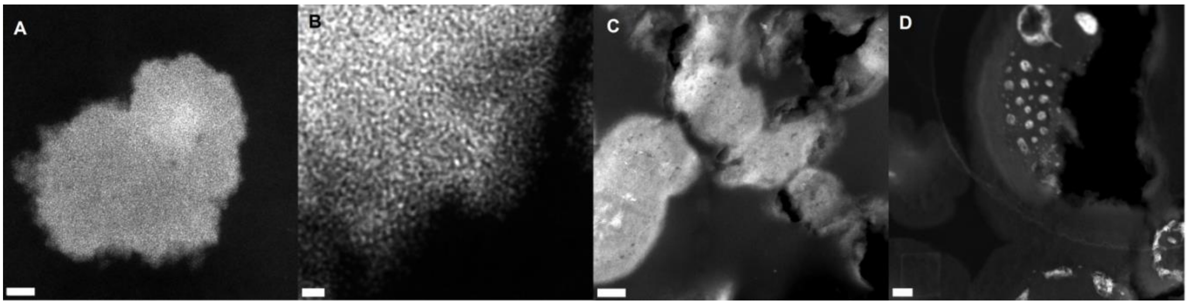

Figure 3.3.4. HAADF-STEM images of **HM3** (A, scale bar 50 nm), **HM4** (B, scale bar 10 nm), **HM5** (C, scale bar 100 nm) and **HM6** (D, scale bar 100 nm).

The nano-structuring of the materials was investigated by HAADF-STEM images (Figure 3.3.4). Materials **HM3** and **HM4** give similar pictures as reported for the corresponding silicon materials.[71] The inorganic phase forms nanometer sized clusters, which are homogenously distributed over the entire sample. An analogous image was obtained for **HM5** with ZrO_2 nanoclusters evenly dispersed in the organic matrix.

This indicates a full conversion of **5** during the twin polymerization process. In contrast, the HAADF-STEM images (Figure 3.3.4) from **HM6** reveal larger domains of ca. 100 nm, which are enriched with HfO_2. The surrounding material is impoverished of HfO_2. The higher mass of hafnium significantly influences the ratio between the inorganic component and the organic material. Hence, the hafnium-containing nanoclusters formed during the reaction can easily grow to a larger size then in **HM5**. This is supported by the polymerization behavior of **4**. Complex **4** exhibits more polymerizable units then **6** and the stabilization of the hafnium oxide nanoclusters is more effectively achieved during the polymerization process, as confirmed by the corresponding TEM images (Figure 3.3.4). The thermal behaviour of **HM3** - **HM6** was investigated by TG (= thermo gravimetry) studies to determine the weight loss during the carbonization process, remaining oxidizable material and the amount of ZrO_2 or HfO_2. The results of the thermogravimetric analysis are summarized in Table 3.3.2.

Table 3.3.2. Thermogravimetric data of **HM3** - **HM6** (40 - 800 °C, 10 K/min, 20 mL/min N_2; cooling to 100 °C, 50 K/min, 20 mL/min N_2; 40 - 800 °C, 10 K/min, 20 mL/min O_2).

Hybrid Material	Carrier Gas	Onset I [°C]	Δm_1 [%]	Onset II [°C]	Δm_2 [%]	Residue [%]
HM3	N_2	335	29.4	487	8.7	
	O_2/N_2	373	25.1	-	-	19.0
HM4	N_2	332	23.9	425	12.7	
	O_2/N_2	380	13.2	424	6.8	35.7
HM5	N_2	397	28.7	541	6.8	
	O_2/N_2	246	25.8	362	7.1	22.8
HM6	N_2	403	18.7	548	6.5	
	O_2/N_2	316	13.4	360	15.0	41.3

It is obvious that materials **HM3** and **HM4** show a weight loss with an onset temperature at 335 °C, while **HM5** and **HM6** started to decompose at ca. 400 °C. Under oxidizing conditions, the remaining organic material reacts at the same temperature level, while the carbon content of **HM5** oxidizes at the lowest temperature observed.

Due to the higher molar mass of hafnium, hybrid materials with an enriched inorganic component were formed as depicted in Table 3.3.2.

3.3.5 Characterization of the inorganic materials derived from HM3 – HM6

The composition of the inorganic oxidation products **HM3 - HM6** was investigated with EDX (see ESI for EDX mapping). For **HM3** and **HM5** a Zr content of 73 % (theory 74%) and for **HM4** and **HM6** a Hf content of 84 % (theory: 85 %) was observed. The inorganic residue of **HM3** and **HM4** consists of nano-crystalline monoclinic domains of ZrO_2 or HfO_2, while **HM5** and **HM6** are nearly amorphous. Only broad reflexes were obtained by XRPD measurements and hence the determination of the crystal system was not possible for these oxides. In combination with the EDX results the identity of inorganic materials was proven.

As similar to the silicon-based twin polymerization process, the porosity of the obtained inorganic materials from **HM3** – **HM6** was determined. The calculated surface areas for all materials are below 100 m^2/g, which is significant lower as for silicon-based twin monomers (500 - 600 m^2/g[62,63]). Compared with TiO_2 or WO_3, obtained from similar monomers, the surface areas are, however, in the same range[76,78]. One explanation for this behavior is the high amount of inorganic component which simplifies sintering processes.

3.3.6 Copolymerization of 5 and 6 with 2,2‘-spiro-bi[4H-1,3,2-benzodioxasiline] and characterization of the as prepared mixed oxides MO_2/SiO_2 (M = Zr, Hf)

Tetrafurfuryloxy silane (= TFOS) does not copolymerize with SBS, since complexes **3** and **4** contain the TFOS motif, thus solely compounds **5** and **6** were used for the copolymerization with SBS.[72,161] Therefore, 25 mol-% of the appropriate complex was polymerized with SBS under identical conditions as for the homo-polymerization (see above). The formed pink coloured solids (**HM7**, Zr-containing and **HM8**, Hf-containing) have the same appearance as the respective materials derived from SBS under similar conditions (Scheme 3.3.2).

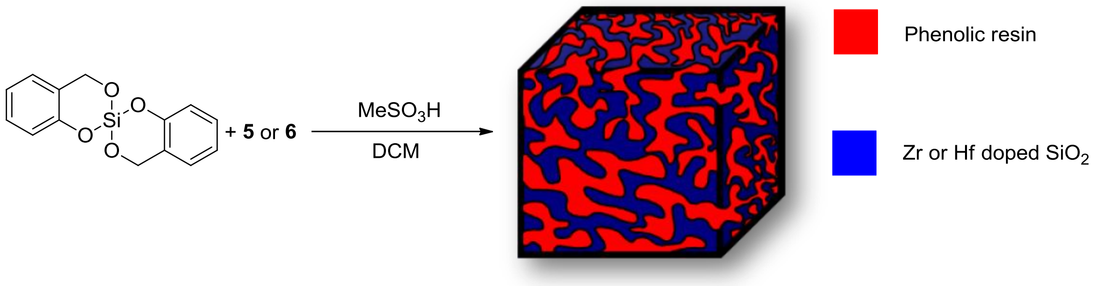

Scheme 3.3.2. Schematic outline of the preparation of **HM7** and **HM8** starting with 2,2‘-spiro-bi[4H-1,3,2-benzodioxasiline] and complexes **5** or **6**, yielding a Zr- (**HM7**) or Hf-enriched (**HM8**) twin polymer.

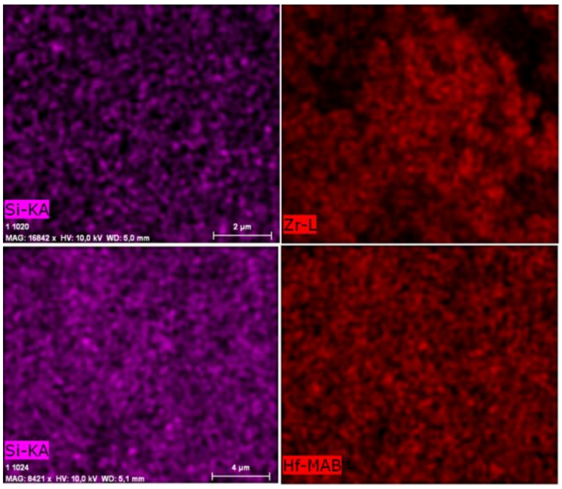

Figure 3.3.6. REM-EDX mappings of **HM7** and **HM8** showing the homogenous distribution of Si (violet) and Zr (red, upper row) respectively Hf (red, lower row) over the whole hybrid materials (see ESI for higher resolution).

The distribution of Zirconium and Hafnium within the hybrid materials was investigated by REM-EDX measurements. Therefore, a homogenous distribution of Zr or Hf is observed over the whole sample and no evidences for a phase separation within the inorganic matrix are found (Figure 3.3.6).

The appropriate materials were firstly carbonized at 800 °C for 2 h under an Argon atmosphere and then oxidized in air at 450 °C for 48 h to obtain the inorganic lattice as a white solid. EDX measurements reveal for both Zr- and Hf-containing silicon dioxides a homogenous distribution over the entire sample with a Zr amount of 20 % and a Hf amount of 23 %. The mixed oxides are mainly mesoporous, with pore sizes between 2 and 4 nm (see ESI for detailed information). The surface area is slightly higher for the ZrO$_2$ containing material (684 m^2/g) as for HfO$_2$/SiO$_2$ (550 m^2/g). The samples are completely amorphous as shown by XRPD. Temperature-depended

XRPD patterns reinforce no crystallization up to 800 °C. After calcination at 1000 °C the incorporated ZrO_2 and HfO_2, respectively, are crystalline as evidenced by XRPD (ESI). A tetragonal phase was found for Zr with crystallite sizes of 12 ± 1 nm (XRPD), being in accordance with the literature[162,163]. Considering the Hf-containing material, the phase could not be clearly estimated since an additional reflex near the [101] one occurs and hence the determination of crystallite size was not possible.

A (HAADF-)STEM analysis of the zirconium oxide-containing sample reveals ZrO_2 nano-crystals in a silicon matrix as depicted in Figure 3.3.7. The highly crystalline nature of these nanoparticles was shown by HR-TEM images, with the main portion of particles within the size of 10 and 20 nm. The size distribution could not be verified for the HfO_2-containing sample since a sharp delimitation of the particles is not possible. Due to the calcination process, however, the surface area decreases from 684 to ca. 20 m^2/g.

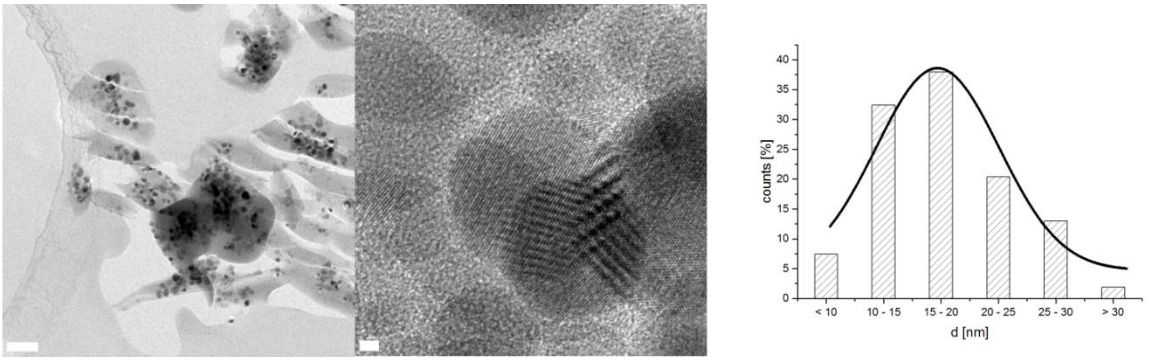

Figure 3.3.7. Left: TEM image of the SiO_2/ZrO_2 mixed oxide tempered at 1000 °C, showing ZrO_2 nanoparticles within the SiO_2 matrix (inset: size distribution; scale bar, 100 nm); right: HRTEM of the observed ZrO_2 particles (scale bar, 2 nm).

The thermal behavior of the incorporated nanoparticles and the SiO_2 lattice above 1000 °C was investigated by differential scanning calorimetry (= DSC). Heating the sample to 1300 °C resulted in a broad endothermic event (beginning at around 500 °C), which probably refers to the sintering processes of the porous material (Figure 3.3.8). In the high temperature region (> 1000 °C) no significant traces could be detected, while cooling the sample from 1300 °C to 40 °C allowed the observation of an exothermic process at 218 °C. The reversibility of this process was tested while heating the sample again in the DSC to 300 °C, the obtained curves are depicted in Figure 3.3.6. At 238 °C an endothermic process (-139 mJ) was observed. On cooling the sample to 40 °C an exothermic reaction (146 mJ) took place at 218 °C, which is typical for a crystallization process. A similar behavior was observed for the hafnium-containing material, however, the endothermic (206 °C, -64 mJ) and exothermic processes (193 °C, 62 mJ) are shifted to lower temperatures in contrast to the zirconium-containing system.

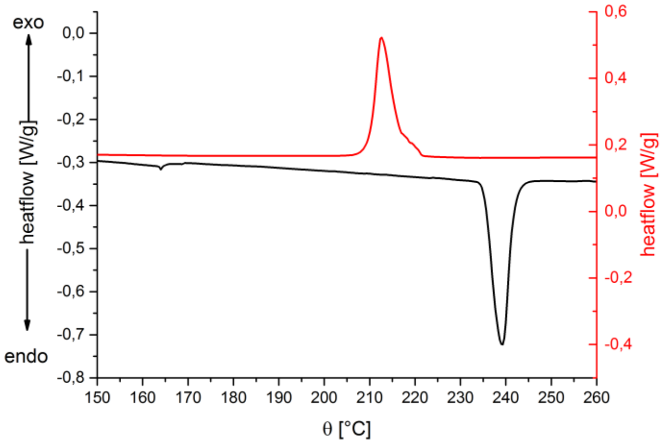

Figure 3.3.8. DSC curve of the high temperature sintered material (black: 40 - 300 °C, 10 K/min, N_2; red: 300 - 40 °C, 10 K/min, N_2).

This behavior was further investigated for the ZrO_2-containing material by temperature dependent X-ray powder diffraction analysis (Figure 3.3.9). The diffraction patterns at 215 °C and 235 °C show the phase transition of α-cristobalite to β-cristobalite (Figure 3.3.9), which is significantly lower than for pure α-cristobalite (275 °C) being in accordance with references [164–166]. The HfO_2-containing material shows a similar phase transition, but it occurs at lower temperatures (205 °C endothermic, 193 °C exothermic).

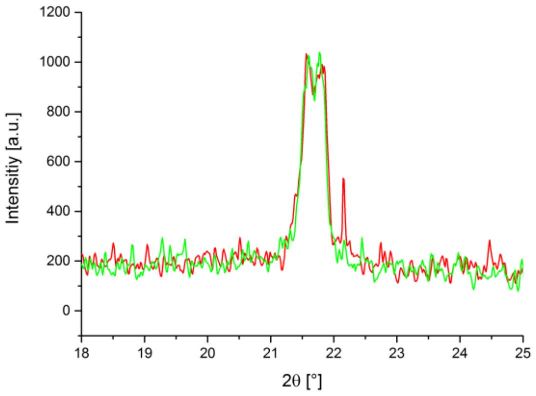

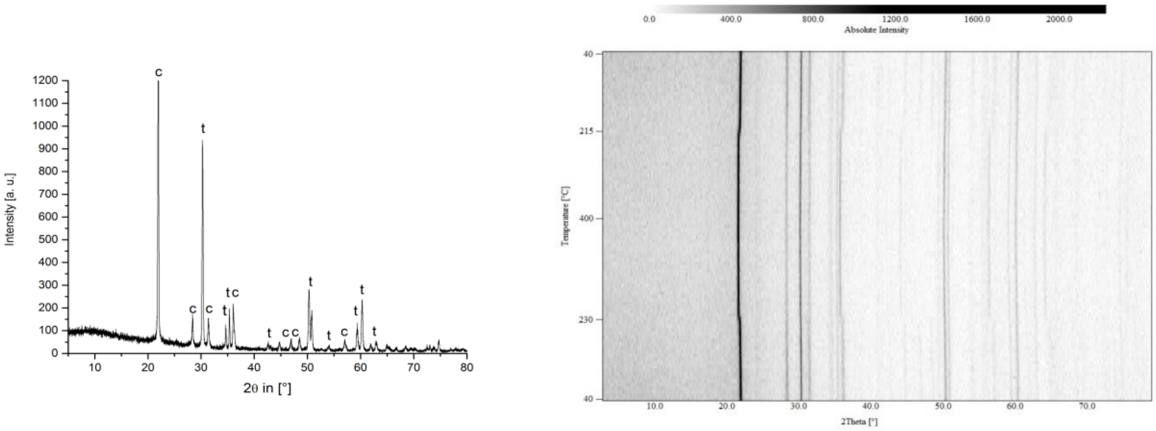

Figure 3.3.9. Top: Phase equilibrium between the [101] reflexes of α- and β–cristobalite during the heating and cooling process of the sample (red: measured at 235 °C heating up the sample $\alpha \rightarrow \beta$, green: measured at 215 °C cooling the sample $\beta \rightarrow \alpha$). Left: XRPD pattern after sintering the SiO_2/ZrO_2 mixed oxide at 1300 °C, showing tetragonal ZrO_2 crystallites (t) within the cristobalite matrix (c). Right: temperature dependent XRPD patterns, indicating the phase transition between α-cristobalite and β-cristobalite (see ESI for XRPD patterns were both phases are present).

3.3.7 Conclusion

In this work, the twin polymerization principle was extended to zirconium- and hafnium-based monomers of the type [M(2-$OCH_2{}^cC_4H_3O)_4$(x $HOCH_2{}^cC_4H_3O$)] (**3**, M = Zr, x = 0; **4**, M = Hf, x = 1) and M[(2-OCH_2-$C_6H_4O)_2$(2-$HOCH_2$-C_6H_4OH)] (**5**, M = Zr; **6**, M = Hf), which are accessible by treatment of metal alcoholates $M(OR)_4$ (M = Zr, R = ${}^nC_3H_7$, **1**; M = Hf, R = ${}^nC_4H_9$, **2**) with the corresponding alcohol. The polymerization and copolymerization behavior of **3** - **6** with 2,2'-spiro-bi[4H-1,3,2-benzodioxasiline] (= SBS) yielding the hybrid materials **HM3-HM6** was investigated. Hybrid materials from **3** (**HM3**) and **4** (**HM4**) were obtained after acid-catalyzed ($(CF_3SO_2)_2O$ for **3** and **4**, $MeSO_3H$ for **5** and **6**) twin polymerization. The formation of byproducts such as difurylmethane during the twin polymerization process are consistent with literature results of the polycondensation of furfuryl alcohol[157,158]. Solid state $^{13}C\{^1H\}$ CP-MAS NMR data of **HM3** and **HM4** revealed the typical polymeric structure as observed by polymerization of silicon monomers of type Si(2-$OCH_2{}^cC_4H_3O)_4$ [62,76]. After thermal decomposition of the organic matrix, the remaining inorganic materials MO_2 (M = Zr, Hf) possess a surface area below 100 m^2/g. The hybrid materials **HM5** and **HM6** were obtained from **5** and **6** under acid-catalyzed conditions ($MeSO_3H$), but the polymerization behavior differs from each other. Considering the solid state ^{13}C NMR spectra of **HM5**, no resonance signal for the **C**H_2-O-M units was observed, but is present in the spectra of **HM6**. Therefore, it can be concluded that the polymerization of **6** is incomplete. This result was substantiated by HAADF-STEM images. **HM5** shows the typical micro-structuring observed for twin polymers, while **HM6** suffers from phase separation between the organic and inorganic phases. The amount of formed HfO_2 nanoclusters during the polymerization process is too high, leading to phase separation of the inorganic phase and the organic polymer. The copolymerization behavior was investigated with complexes **5** and **6** and SBS. After oxidation of the organic material white solids were obtained. These mixed oxides have a high surface area of 684 (ZrO_2) and 550 m^2/g (HfO_2), respectively, and the Zr and Hf is homogenously distributed over the entire sample. In addition, the thermal behavior of these materials was investigated. Sintering at 1000 °C gave tetragonal ZrO_2 and HfO_2 nanoparticles within the SiO_2 matrix. At higher temperatures, also the silicon dioxide matrix crystallized producing Zr- or Hf-doped crystobalite ceramics. We have demonstrated that the produced inorganic materials are highly modifiable thru thermal sintering, hence enabling a broad field of application for this materials including their usage as gas sensors and high k dielectrics, respectively, which is the subject of further investigations.

3.3.8 Experimental Section

General procedures and starting materials

All reactions involving moisture sensitive compounds (**3** – **6**) were carried out under an atmosphere of dry argon using standard Schlenk techniques. Dichloromethane and pentane were purified by distillation from calcium hydride. Toluene and hexane were dried using a M. Braun SBS-800 purification system (stationary drying with molecular sieve columns 3 Å).

Zirconium propoxide (70 % in propanol) (**1**), hafnium butoxide (**2**) and salicylic alcohol were purchased from Sigma Aldrich and were used without further purification. 2-Furylmethanol (Acros) was distilled before use and stored under an inert argon atmosphere in the absence of light at - 30 °C. 2,2'-Spirobi[4*H*-1,3,2-benzodioxasiline] was prepared according to a published procedure.[63] All thermal operations were carried out in a Carbolite Tube Furnace MTF 12/38/400.

^{1}H NMR (500.3 MHz) and ^{13}C{^{1}H} NMR (125.8 MHz) spectra were recorded with a Bruker Avance III 500 spectrometer at 298 K. Chemical shifts δ are reported in ppm (parts per million) using undeuterated solvent residues as internal standard (benzene-d_6: ^{1}H, 7.16 ppm and ^{13}C{^{1}H}, 77.16 ppm). Solid state ^{13}C{^{1}H} NMR experiments were conducted using cross polarization (CP) and magic angle spinning (MAS) with spinning frequencies of 12.5 kHz or 20 kHz. Infrared spectra were recorded with a FT-IR Nicolet 200 spectrometer. X-ray powder diffraction analyses were carried out with a STOE-STAD-IP (Cu K_α λ = 0.154 nm). SEM images and EDX analysis were performed with a Phillips NanoNovaSEM. HAADF-STEM were recorded with a Fecnai FC20 with 200 kV accelerating voltage. Gas absorption-/desorption measurements were carried out using a Autosorb IQ2 system. Thermal analyses were performed with a Mettler Toledo TGA/DSC1/1600 system with a MX1 scale. DSC experiments were performed with a Mettler Toledo DSC1/700 equipment.

Temperature-dependent XRPD

Temperature-dependent XRPD measurements were performed as follows: the presintered material from the high temperature DSC experiment was sealed in a quartz vial and heated from 30 to 400 °C in 10 K steps with a heating rate of 10 K/min. Each step was equalized for 10 min and then the XRPD was measured (10 min).

TGA-DSC

One sample of binary oxide ($MO_2/SiO_{2;}$ M = Zr, Hf) was transfered in a standard aluminium oxide crucible and heated in the TGA-DSC device under a continuous flow of argon up to 1300 °C with a heating rate of 10 K/min. After reaching the final temperature the sample was cooled to room temperature with a cooling rate of 10 K/min. The obtained sintered disc was transferred into the DSC system and the thermal behaviour from 40 to 400 °C (10 K/min) was investigated.

Synthesis of Twin Monomers

Synthesis of Zirconium(IV) tetra-2-furylmethoxide (3). In a typical procedure, 4.26 g (0.013 mol) of **1** were mixed with 4.5 mL (0.052 mol) of 2-furyl methanol at room temperature. The reaction mixture was heated for 2 h at 40 °C in oil pump vacuum. Then the temperature was increased to 100 °C within 4 h. All volatiles were removed by distillation during this period. After the remaining melt solidified it was diluted in abs. toluene (20.0 mL) and precipitated in pentane (40.0 mL). This procedure was repeated trice. After removing of all volatiles from the remaining oil, a highly viscous orange residue was obtained (yield: 5.43 g, 87 %). Elemental analysis calculated for $C_{40}H_{40}O_{16}Zr_3$: C 45.74, H 3.84; found : C 45.87, H 4.23; IR (KBr, cm^{-1}): 3616 s [ν(OH)], 2911 s [$\nu_{as}(CH_2)$] , 2846 s [ν_s (CH_2)], 1503 s [$\delta(CH_2)$]; ^{1}H NMR (C_6D_6, ppm): 7.12 (broad s, 1H, 2-C**H**), 6.21 (broad s, 1 H, 3-C**H**), 6.11 (broad s, 1 H, 4-C**H**), 5.07 (broad s, 2 H, C**H**$_2$); $^{13}C\{^1H\}$ NMR (C_6D_6, ppm): 156.5 (OCH_2**C**), 141.71 (5-^{c}**C**$_4H_3O$), 110.57 (3-^{c}**C**$_4H_3O$), 107.23 (4-^{c}**C**$_4H_3O$), 64.64 (O**C**H_2).

Synthesis of Hafnium(IV) tetra-2-furylmethoxide (4). 5.00 g (0.011 mol) of **2** and 4 mL (0.046 mol) of 2-furyl methanol were reacted under the same reaction conditions as described for the synthesis of **3**. After appropriate work up, complex **4** was obtained as an orange sticky residue (yield: 2.41 g, 56 %). Elemental analysis calculated for $C_{40}H_{40}O_{16}Hf_3$ x $C_5H_7O_2$: C 38.32, H 3.29; found : C 38.72, H 3.31; mp: > 200 °C decomp.; IR (KBr, cm^{-1}): 3348 s [ν(OH)], 2921 s [$\nu_{as}(CH_2)$], 2829 s [ν_s (CH_2)], 1504 s [$\delta(CH_2)$]; ^{1}H NMR (C_6D_6, ppm): 7.11 (broad s, 1H, 2-C**H**), 6.22 (broad s, 1 H, 3-C**H**), 6.12 (broad s, 1 H, 4-C**H**), 5.19 (broad s, 2 H, C**H**$_2$); ^{13}C $\{^1H\}$ NMR (C_6D_6, ppm): 157.27 (OCH_2**C**), 141.82 (5-^{c}**C**$_4H_3O$), 110.74 (3-^{c}**C**$_4H_3O$), 107.37 (4-^{c}**C**$_4H_3O$), 64.60 (O**C**H_2).

Synthesis of Zirconium(IV) di(1-hydroxy-2-benzyloxy) (5). Salicylic alcohol (4.77 g, 0.039 mol) was suspended in 50 mL of abs. toluene and 5.0 g (0.013 mol) of **1** were added in a single portion. The reaction mixture turned yellow and was heated under vacuum for 2 h at 80 °C. After all volatiles were removed, the remaining yellow melt solidified at ambient temperature. The residue was diluted in 20 mL of abs. dichloromethane and filtered through celite (4 cm). After washing with an additional portion of dichloromethane (15 mL) the combined filtrates were concentrated in vacuum (10 mL) and **5** was precipitated upon addition of abs. hexane (50 mL). The remaining solvents were removed *in vacuo* yielding a yellow solid (yield: 3.88 g, 66 %).

Elemental analysis calculated for $C_{42}H_{36}O_{14}Zr_3$ x $C_7H_8O_2$: C 52.06, H 3.92; found : C 51.56, H 4.04; mp: > 200 °C decomp.; IR (KBr, cm^{-1}): 3434 s [ν(OH)], 2914 s [ν_{as}(CH_2)] , 2864 s [ν_s (CH_2)], 1483 s [δ(CH_2)]; CP-MAS-$^{13}C\{^1H\}$ NMR (ppm): 159.16 (C-Phenyl), 128.85 (C-Phenyl), 119.16 (C-Phenyl), 70.31 (O**C**H_2).

Synthesis of Hafnium(IV) di(1-hydroxy-2-benzyloxy) (6). A mixture of 5.0 g (0.011 mol) of **2** and 3.51 g (0.032 mol) of salicylic alcohol was reacted accordingly to the synthesis of **5**, giving, after appropriate workup, 3.16 g (70 %) of a yellow solid material. $C_{42}H_{36}O_{12}Hf_2$ x $C_7H_8O_2$: C 48.48, H 3.65; found : C 48.48, H 4.04; IR (KBr, cm^{-1}): 3401 s [ν(OH)], 2928 s [ν_{as}(CH_2)], 2867 s [ν_s (CH_2)], 1484 s [δ(CH_2)]; CP-MAS-$^{13}C\{^1H\}$ NMR (ppm): 160.29 (C-Phenyl), 128.03 (C-Phenyl), 118.01 (C-Phenyl), 68.20 (O**C**H_2).

Polymerization of complex 3. Trifluroacetic acid anhydride (40.0 mg, 0.14 mmol) was diluted in 20 mL of abs. toluene and heated to 80 °C. To this solution 2 mL (1.25 g, 0.72 mmol) of the monomer solution of **3** in abs. toluene was added in a single portion, causing an immediate colour change to black. After 48 h of stirring at 80 °C, the precipitated black hybrid material was collected by filtration and washed twice with dichloromethane (15 mL each). After drying the residue under vacuum, 997 mg of a dark green solid was obtained.

Polymerization of complex 4. As stated above 8.3 mL (1.0 g, 2.72 mmol) of the monomeric toluene solution of **4** was added to a similar solution of initiator and solvent as used for the polymerization of **3**. After appropriate work up, 986 mg of a black solid was obtained.

Polymerization of complex 5. Compound **5 (**1.0 g, 2.0 mmol) was dissolved in 100 mL of abs. dichloromethane and the mixture was heated to reflux. Then 0.08 mL (1.25 mmol) of methansulfonic acid diluted in 0.8 mL of abs. dichloromethane was added via a syringe. The clear reaction solution turned cloudy and the hybrid material precipitated by refluxing the mixture for 12 h. The precipitate was collected by filtration and washed twice with dichloromethane (20 mL), affording 0.77 g of an off-white solid.

Polymerization of complex 6. Complex **6** (2.0 g, 3.6 mmol) was treated as described above, producing 1.4 g of a yellow solid.

Copolymerization of 5 and 6 with 2,2'-spirobi[4*H*-1,3,2-benzodioxasiline] (HM7 and HM8). 2.0 g (7.3 mmol) of 2,2'-spirobi[4*H*-1,3,2-benzodioxasiline] and 25 mol-% of **5** (0.84 g, 1.8 mmol) or **6** (1.01 g, 1.8 mmol) were dissolved in 100 mL of abs. dichloromethane and the respective reaction mixture was heated to 40 °C. Then 0.16 mL (2.49 mmol) of methansulfonic acid diluted in 0.8 mL of abs. dichloromethane were added via a syringe in a single portion. The solution turned cloudy and a pink colored hybrid material precipitated after 12 h of reflux. The solid material was collected by filtration and washed twice with dichloromethane (20 mL each). After drying *in vacuo,* 2.7 g of a pink colored solid was obtained.

General procedure for the oxidation of the hybrid materials HM3 - HM8. In a typical experiment, the appropriate hybrid material was transferred to an aluminium oxid crucible and placed in a quartz tube furnace. Under a continuous flow of Ar the material was heated to 800 °C (50 K/min) and kept at this temperature for 30 min. After cooling to room temperature, the sample was heated again under a continuous flow of air to 450 °C (50 K/min) and hold at this temperature for 48 h, resulting in white solids.

Crystallization of ZrO_2 and HfO_2 in a SiO_2 matrix (oxides obtained from HM7/HM8). The binary oxides (200 mg) were placed in a porcelain crucible and were then heated to 1000 °C (heating rate 25 K/min) and kept there for 48 h. After cooling to room temperature a white powder was obtained.

3.3.9 Acknowledgement

We are grateful to the Deutsche Forschungsgemeinschaft (FOR 1497 Organic-Inorganic Nanocomposites by Twin Polymerization) and the Cluster of Excellence MERGE (DFG EXC 1075, MERGE Technologies for Multifunctional Lightweight Structures) for generous financial support. Furthermore, we like to thank T. Jagemann and Prof. M. Hietschold for REM imaging and EDX mapping of different samples and Dr. D. Schaarschmidt for GC-MS analysis.

3.4 Metal Nanoparticle-loaded Porous Carbon Hollow Spheres by Twin Polymerization

C. Schliebe, T. Graske, T. Gemming and Heinrich Lang

Eingereicht in *J. Mater. Chem.C* **Januar 2015**.

Die Synthese und Charakterisierung der in diesem Kapitel veröffentlichten Kohlenstoffhohlkugeln, sowie die Diskussion der erhaltenen Ergebnisse wurden vom Autor durchgeführt. Die kinetischen Untersuchungen hat T. Graske im Rahmen seiner Bachelorarbeit unter Anleitung des Autors durchgeführt und ausgewertet. Alle gezeigten TEM-Bilder wurden von Dr. T. Gemming angefertigt und vom Autor interpretiert. Der zu dieser Arbeit gehörende präparative Teil ist im Anhang 7.1.4 hinterlegt.

3.4.1 Introduction

Encapsulation and protection of active species like metal nanoparticles, gathered great attraction during the last decade.[167,168] These materials are benefiting also from a vast variety of advantages provided by the capsule itself, for example, preventing the phase coalescence of metal nanoparticles and hence enabling mass transport between the hollow core and the surrounding environment.[169] The preparation of functional hollow carbon spheres (= HCS) predominantly involves a meso-porous silicon dioxide template, which is coated with trimethylsilyl-terminated octadecane.[170] After chemical carbonization and removal of the template with hydrofluoric acid, HCS with a meso-porous hull (S_{bet} = 1620 m^2/g) were obtained[171,172]. The thus prepared HCS are infiltrated by incipient wetness methods with Pt and Ru salts giving after reduction $Pt_{50}Ru_{50}$ nanoparticles, which could successfully be applied as catalyst in direct methanol or formic acid fuel cells[50,173,174], showing an improved catalytic activity compared to commonly used carbon black supports. With a similar procedure $CoFe_2O_4$, Fe_3O_4, Sn and SnO_2 nanoparticles were incorporated and encapsulate in porous carbon, leading to magnetically separable HCS ($CoFe_2O_4$ and Fe_3O_4) or new anode materials (Sn and SnO_2) for high capacity Li-ion batteries.[175–179] A different concept for the functionalization of HCS with nanoparticles is given by using the respective nanoparticles as templates.[180] For example, Au or Fe_3O_4 nanoparticles were firstly encapsulated in a SiO_2 material and then a meso-porous silica layer was grafted onto this particles.[180] The metal-containing silica template was coated with a carbon source, like polystyrene and afterwards it was carbonized.[52] After removal of the silica template with hydrofluoric acid, the nanoparticles were entrapped into an mesoporous HCS.[52] Another example for direct encapsulation of metal nanoparticles was achieved by reacting a solution of glucose and silver nitrate under hydrothermal conditions, whereby carbon-coated silver nanoparticles were obtained.[51]

Recently, the concept of twin polymerization[63,71] was introduced in the preparation of hybrid materials using silicon orthoesters of salicylic or furfurylic alcohol.[62,63,70,71,154,181] Polymerization of these compounds results in a strong mechanistically coupling between the inorganic and organic polymerization processes imbuing networks on a nanometer scale. This methodology can also be used for the preparation of a variety of hollow carbon structures[74]. By coating the specific hard template with a twin polymer a porous carbon shell is obtained after carbonization and removal of the inorganic lattice.[73] By changing the twin monomer, the amount of micro- and meso-porosity of the carbon shell can be influenced.[73] For example, the incorporation of heteroatoms like sulfur into the HCS hull was achieved by using, tetrathienyloxy silane.[182] The resulting materials can, for example, be used as anode materials in sulfur-lithium-ion batteries, showing an improved cycle stability towards established systems.[183]

Herein, we present a straightforward approach for the encapsulation of silver and gold nanoparticles within a porous carbon shell by twin polymerization.

3.4.2 Synthesis of the carbon encapsulated metal nanoparticles

For the preparation of hollow carbon spheres (= HCS) filled with metal nanoparticles, spherical silica hard templates of different diameters (Aerosil® AS90, d ~ 20 nm; Aerosil® OX50, d ~ 40 nm; Stöber particles, d ~ 200 nm) were used and processed according to a modified procedure.[73] Therefore, the metal precursors $[AgO_2C(CH_2OCH_2)_3H]$ (**1**) and $[(PPh_3)AuO_2C(CH_2OCH_2)_3H]$ (**2**), respectively, were dissolved in acetonitrile (**1**) or dichloromethane (**2**) and applied to the specific template by using incipient wetness methods (Scheme 3.4.1).[112,113,137,138,184,185]

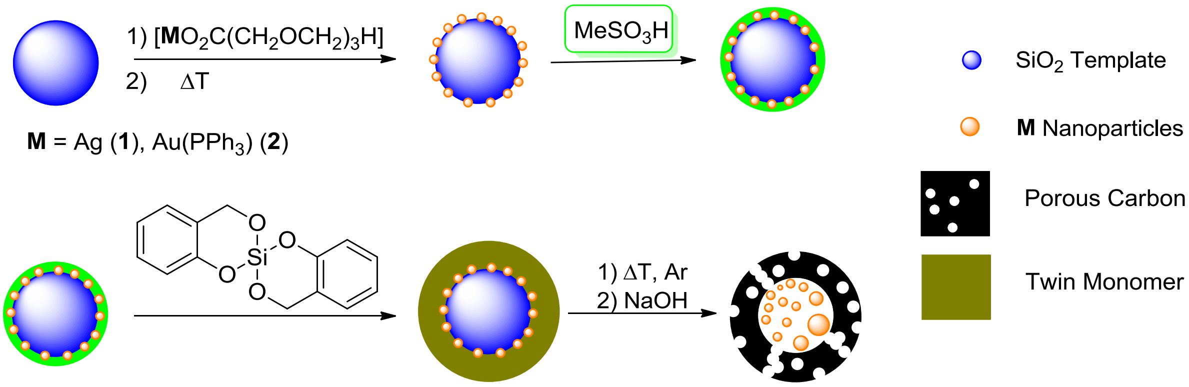

Scheme 3.4.1. Preparation of metal nanoparticle filled HCS by twin polymerization.[73]

The precursor-loaded templates were then transferred to a tube furnace and treated under argon for 1 h at 250 °C (see ESI for detailed information). A color change of the AS90 and OX50 spheres from colorless to yellow (silver) or red (gold) was observed, which is caused by the plasmon resonance of the respective formed nanoparticles (Figure 3.4.1).[186,187]

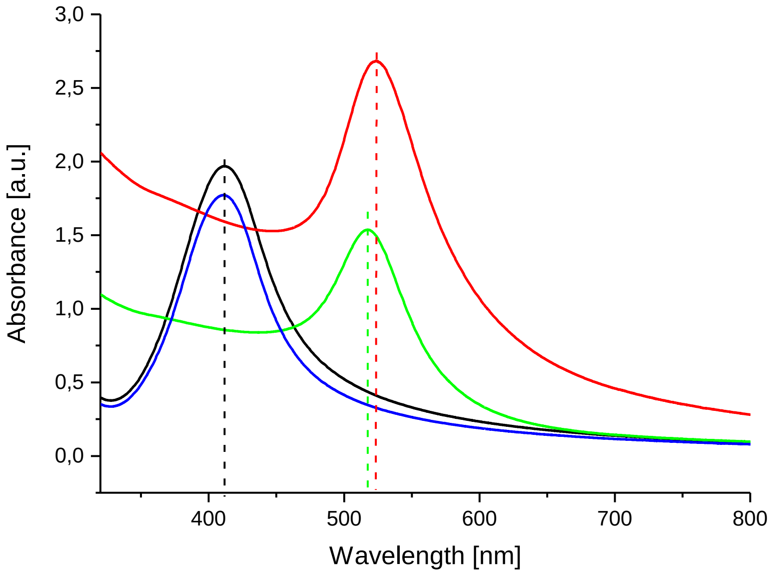

Figure 3.4.1. UV-Vis spectra showing the plasmon resonance of the deposited nanoparticles Ag on AS90 (black), Ag on OX50 (blue), Au on AS90 (red) and Au on OX50 (green) suspended in dichloromethane.

The loaded silica templates were then suspended in dichloromethane and after the addition of $MeSO_3H$ as initiator the solvent was replaced by toluene. After redispersion, a solution of the twin monomer 2,2‘-spiro-bi[4H-1,3,2-benzodioxasiline] (= SBS, **3**) was added and after 12 hours of stirring the twin polymer-coated template was carbonized at 800 °C under argon. The inorganic lattice of the twin monomer and the spherical template was removed by refluxing with 5 M sodium hydroxide, giving the respective metal nanoparticle-loaded HCS.

The metal loading was determined by atomic absorption spectroscopy (= AAS). However, this was only successful for the gold-containing hollow carbon spheres and the silver containing material derived from the Stöber particle template (Table 3.4.1). For the silver-containing carbon HCS prepared with the AS90 and OX50 template, the metal loading was determined from hybrid material-coated compounds before carbonization, since the concentration in the carbon materials was too low for a successful AAS analysis.

Table 3.4.1. Metal loadings of the hybrid material-coated compounds (a) or the prepared carbon spheres (b) determined by AAS.

Substrate	Ag	Au
AS90	0.96 %[a]	7.1 %[b]
OX50	0.92 %[a]	7.6 %[b]
Stöber particle	3.8 %[b]	4.0 %[b]

3.4.3 Characterization of the nanoparticle-modified templates

The metal-organic complexes **1** and **2** give upon thermal treatment the respective metal nanoparticles which are stabilized by their in-situ generated organic matrix resulting from the ethylene glycol functionality.[138]

The thermal behaviour of the precursor (**1**, **2**)-loaded templates (AS90, OX50, Stöber particle) was investigated by thermogravimetry (=TG, see ESI for more details). It was found that the corresponding surface-deposited silver carboxylate **1** starts to decompose at 211 - 219 °C,[112] whereby template AS90 and the Stöber particles show a weight loss of 5.8 % or 5.6 % (theoretical = 8.6 %), while the OX50 substrate material possess a weight loss of 9.8 %.

In contrast, the onset temperature of the with **2** loaded templates (see above) covers a somewhat broader range (213 – 228 °C).[185] The weight loss of the respective metal-organic modified templates is 10.1 (AS90), 9.5 (Stöber particles) and 14.1 % (OX50) (for comparison, theoretical = 21.4 %). This behaviour is characteristic for the subsequent thermal degradation of the respective coordination complexes **1** and **2** as reported in literature. [112,185]

The obtained templates were characterized by X-ray powder diffraction studies (= XRPD) showing the characteristic reflex patterns for gold and silver (see ESI). The crystallite sizes were determined with the Scherrer equation to 14 – 44 nm depending on the used templates (Table 3.4.2).

Table 3.4.2. Crystallite sizes of the thermally generated nanoparticles on the different templates (determined by XRPD).

Substrate	Ag	Au
AS90	14 ± 1 nm	19 ± 1 nm
OX50	17 ± 1 nm	34 ± 3 nm
Stöber particle	22 ± 1 nm	44 ± 4 nm

Since the AS90 template has with 90 m^2/g the highest surface area of all templates, the metal nanoparticles are best stabilized and show the smallest diameters.

A TEM study of the used templates (see Figure 3.4.2) confirms the formation of gold and silver nanoparticles on all substrates. For supports AS90 and OX50, metal nanoparticles sizes between 10 - 20 nm were obtained, while on the Stöber particles larger particles (40 - 45) nm were fromed, confirming the XRPD results (Table 3.4.2).

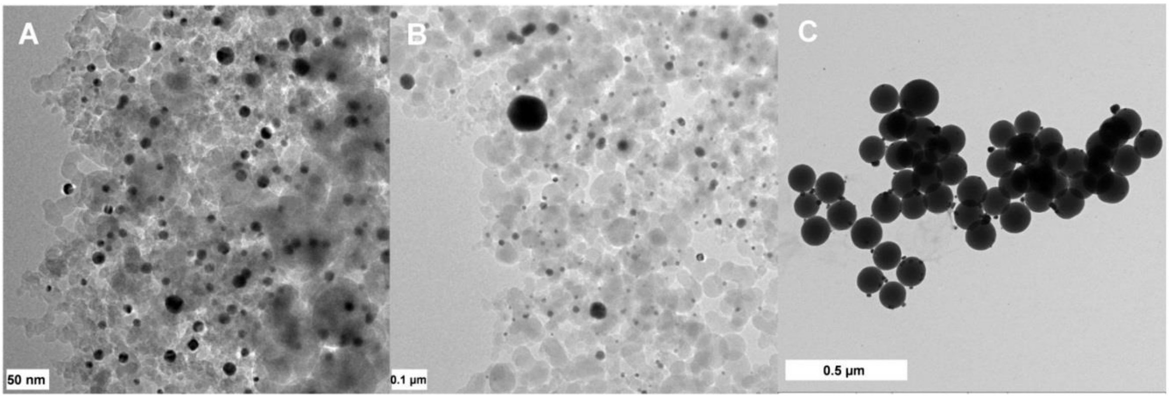

Figure 3.4.2. TEM images of the used templates with the deposited nanoparticles (**A**, Au on AS90; **B**, Au on OX50 and **C**, Ag on Stöber particles; see ESI for further TEM images).

3.4.4 XRPD and electron microscopy studies of the obtained carbon materials

The derived carbon materials (CAS90, COX50 and CSP (= Stöber particle)) were investigated by XRPD measurements. The typical reflex pattern for silver and gold were only found for CSP. The crystallite sizes were calculated using the Scherrer equation (Table 3.4.3) for CSP and by TEM measurements for CAS90 and COX50. The crystallite sizes have been increased for both metals in comparison to the metal nanoparticle-functionalized templates, which is caused by the thermal treatment during the carbonization process.[188,189]

Table 3.4.3. Crystallite sizes and particle sizes (CSP crystallite size from XRPD data, CAS90 and COX50 particles sizes from TEM images. For Au or Ag on COX50 no normal distribution is observed the reported size refer to the arithmetic mean and the standard deviation thereof. The silver nanoparticles could not be observed during TEM studies) of the prepared carbon materials, since they are too densely entrapped within the cavities between the capsules. (See ESI for further TEM images.)

Substrate	Ag	Au
CAS90	-	15 ± 4 nm
COX50	24 ± 11 nm	21 ± 9 nm
CSP	58 ± 10 nm	48 ± 6 nm

As it can be seen from the SEM images in Figure 3.4.3 the CAS90 and COX50 material exhibit mostly spherical structures with only a few broken capsules. Within the CSP small holes can be found, which points to the formation of interconnecting particles during the polymerization process. The thickness of the carbon hull was determined by TEM studies (Figure 3.4.3). The carbon materials derived from the AS90 templates exhibit a foam-like structure with thin walls (thickness 3 – 4 nm) and the incorporated metal particles seem not to be encapsulated rather situated in the cavities between the hollow carbon spheres. A possible explanation is given in Scheme 3.4.2. Although we were not able to observe silver nanoparticles by TEM studies within CAS90, however, AAS studies proved the existents of silver in this material. In comparison, the COX50 carbon spheres has a much thicker capsule walls (ca. 32 nm), which is the consequence of the decreased template surface area while keeping the used amount of monomer equal within the different polymerization procedures.[73] In contrast to the AS90 substrate, the respective metal nanoparticles are encapsulated within the cavities (Figure 3.4.3B). Increasing the template diameter to 200 nm with the Stöber particles, however, did not improve the encapsulation process. Due to their uniform spherical shapes and size distribution homogenously formed carbon spheres were obtained. The wall thickness increases somewhat to 35 nm.

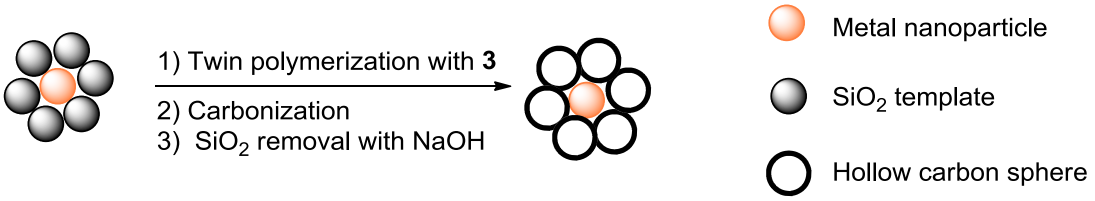

Scheme 3.4.2. Idealized metal nanoparticle stabilization on the AS90 template and resulting encapsulation within the formed cavities between the carbon capsules.

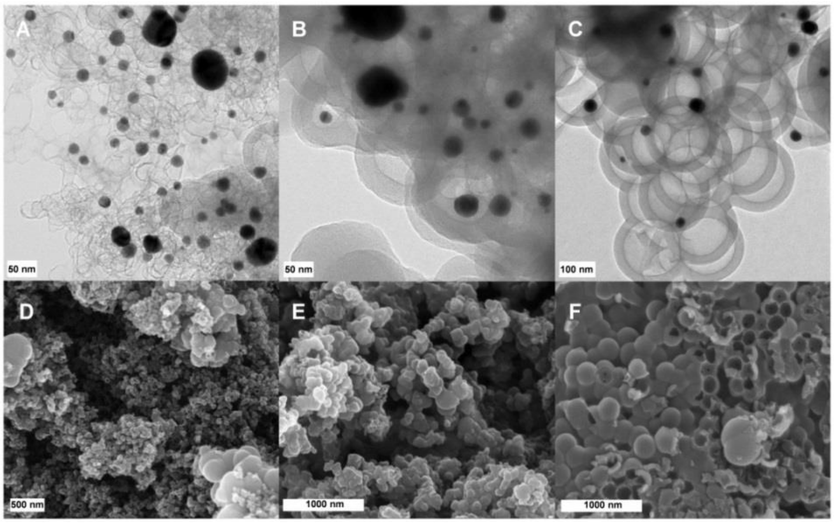

Figure 3.4.3. TEM (**A** - **C**) and SEM (**D** - **F**) image of the obtained carbon materials (**A**, Au on AS90; **B**, Ag on OX50; **C**, Au on Stöber particle; **D**, Ag on AS90; **E**, Au on OX50 and **F**, Au on Stöber particle. For further TEM images see ESI).

3.4.5 Gas adsorption measurements

The porous nature of the prepared materials COX50, CAS90 and CSP was characterized by N_2 adsorption and desorption isotherms at 77 K and the surface areas and pore volumes were calculated using DFT methods[190]. Metal free HCS were prepared to investigate the influence of the incorporated metal nanoparticles. Surface areas reaching from 1165 to 1250 m^2/g were obtained (Figure 3.4.4). Regarding the isotherms, mainly IUPAC Type I isotherms were observed for the Stöber particles used as template. While decreasing the template size (AS90 (20 nm) → OX50 (40 nm)) the observed isotherms (see ESI) exhibit a slight macro-porous behaviour as typical for Type II isotherms.[139] Considering the pore size distribution (ESI) mainly microporous carbons were obtained, which is in accordance with literature.[73] However, the incorporation of gold or silver nanoparticles within the encapsulation process has only minor influence on the porous nature of the final hollow carbon spheres. Regarding the obtained results for silver, a slight decrease of the calculated surface area was observed, while the Stöber particles gave with 972 m^2/g the lowest surface area (Figure 3.4.4). The pore volume also decreases with incorporation of silver nanoparticles. A similar trend was observed for the gold-containing materials. It must be noted that the incorporation of Au nanoparticles leading generally to overall smaller surface areas as observed for silver, while the pore volumes faintly decrease.

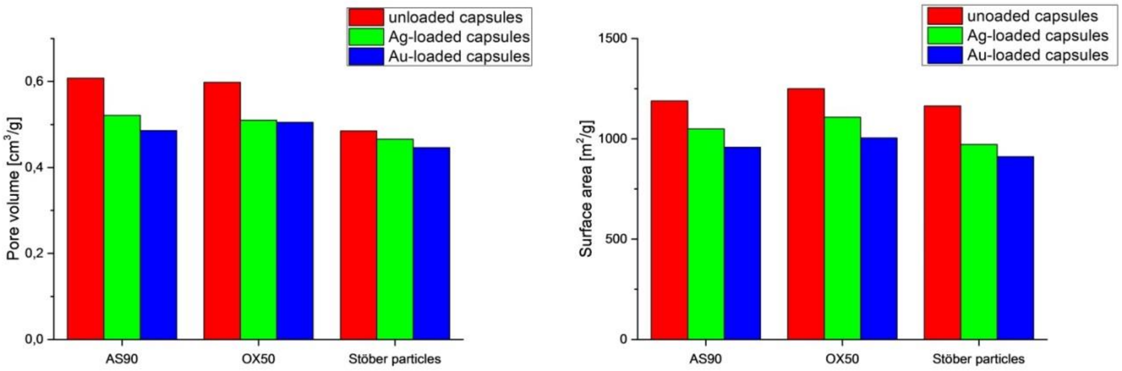

Figure 3.4.4. Comparison of the obtained pore volumes and calculated surface areas of the respectively loaded CAS90, COX50 and CSP materials (derived from nitrogen adsorption-desorption isotherms).

3.4.6 Catalytic reduction of methylene blue

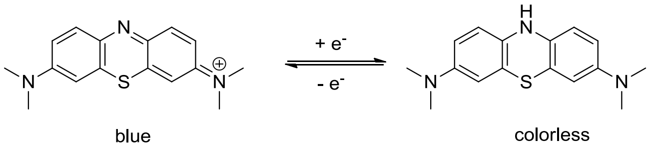

Scheme 3.4.3. Redox reaction of methylene blue and formation of the colorless form (counter ions have been omitted for clarity).[191]

The accessibility of the incorporated silver nanoparticles within the HCS was investigated by the reduction of methylene blue (= MB) with sodium borohydride.[192] The reduction of methylene blue was monitored by UV-Vis spectroscopy (Scheme 3.4.3). In absence of Ag nanoparticles the dye is stable against sodium borohydride, which minimizes side reactions.

In a typical experiment a defined amount (2.95 mg of CAS90, 2.36 mg of COX50, 1.0 mg of CSP; no reaction occurred with smaller amounts of the catalyst) of the specific silver-loaded carbon hollow sphere were suspended in a $2\cdot10^{-5}$ M methylene blue water solution. Afterwards, sodium borohydride was added under stirring and samples were collected and then analyzed by UV-Vis spectroscopy. At the beginning of the reaction an intense absorption at 650 nm was observed, which decreases during the reduction progress (Figure 3.4.5).

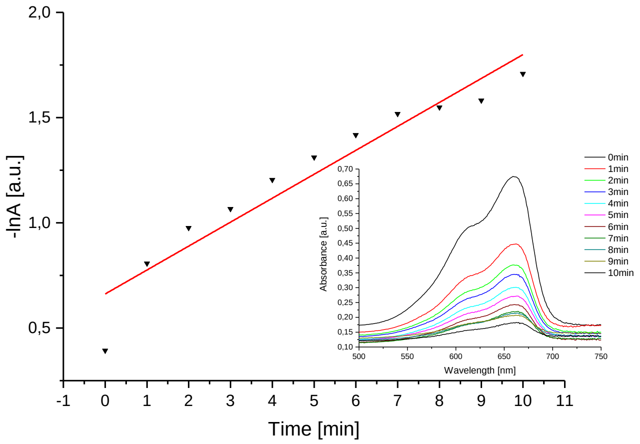

Figure 3.4.5. Logarithmic plot of the absorbance maximum (▼, catalyst: Ag on **CSP**) and the linear fitting to give the *k*-values from their slope (red line). Inset: UV-Vis spectra of methylene blue during the reduction with sodium borohydride and CSP.

This experiment shows that for all prepared silver-containing carbon hollow spheres a first order kinetic is characteristic.[192] The natural logarithm of the absorption maxima were plotted over the passed reduction time (Figure 3.4.5). The k-values for the specific material were determined from the slope. While the k-values for the smallest and largest template (CAS90, $k = 0.096\ s^{-1}$ and CSP, $k = 0.114\ s^{-1}$) are similar, the midsized material COX50 ($k = 0.217\ s^{-1}$) shows a higher value. The obtained results are in accordance with comparable systems described for silver nanoparticles supported on silica spheres.[192] A detailed comparison is difficult, since only the metal-loading of the CSP material could be determined and hence the lack in reactivity is probably contributed to the large crystallite size. The metal content (Table 3.4.1) of the legacy hybrid materials, from where CAS90 and COX50 were obtained, was nearly the same and therefore the difference in the rate constant k must be caused by the surrounding carbon sphere. To verify this hypothesis, the template only modified with the Ag nanoparticles was studied. Regarding the obtained k-values for AS90 ($k = 0.018\ s^{-1}$) and OX50 ($k = 0.361\ s^{-1}$) the same trend was observed. We assume that the smallest template agglomerates around the nanoparticles and so the accessibility is diminished as compared to COX50 (Scheme 3.4.2). This fact also has to be considered during the coating process (Scheme 3.4.2, Figure 3.4.3A). In summary, the nanoparticles will be surrounded by empty hollow carbon spheres, which complicate the approachability to the metal particles.

3.4.7 Catalytic reduction of 4-nitrophenol

The accessibility of the incorporated gold nanoparticles was shown by the reduction of 4-nitrophenol to 4-aminophenol in the presence of sodium borohydride. The experiments were performed in a similar manner as discussed for the reduction of methylene blue (see earlier). A detailed procedure is provided within the ESI. However, the reduction of 4-nitrophenol catalyzed by the gold-containing CSP material was not observed. Since the metal loading was in the same range ($0.9 \cdot 10^{-6}$ mol) for materials CAS90 ($= 1.1 \cdot 10^{-6}$ mol) and COX50 ($= 1.6 \cdot 10^{-6}$ mol, Figure 7) we assume that the larger crystallite size of the used gold nanoparticles is responsible for the low activity of CSP. However, rather smaller particles of the other materials facilitated the catalytic reduction process. This observation is supported by literature,[193] where the catalytic influence on the reduction reaction between growing and fully grown nanoparticles was investigated, showing excellent activity with small nanoparticles (ca. 5

nm).[193] Since, the gold nanoparticles in CAS90 and COX50 are smaller than in the CSP material (Table 3.4.3) a successful reduction of 4-nitrophenol to 4-aminopehnol is observed (Figure 3.4.6). As demonstrated for facetted gold nanoparticles, the concentration of sodium borohydride and 4-nitrophenol has as well an influence on the reaction kinetic.[194] Therefore, the k value has to be considered apparently ($k_{app.}$). The obtained $k_{app.}$ values for CAS90 ($k_{app.}$ = 0.114 s^{-1}) and COX50 ($k_{app.}$ = 0.250 s^{-1}) exhibiting the same trend as observed for the methylene blue experiment. Out of this, we assume that the same structural parameters, like cavity entrapped nanoparticles in CAS90 cause this difference. The obtained results are in agreement with, for example, bimetallic nanoparticles[195] or on ceria deposited Au particles.[196]

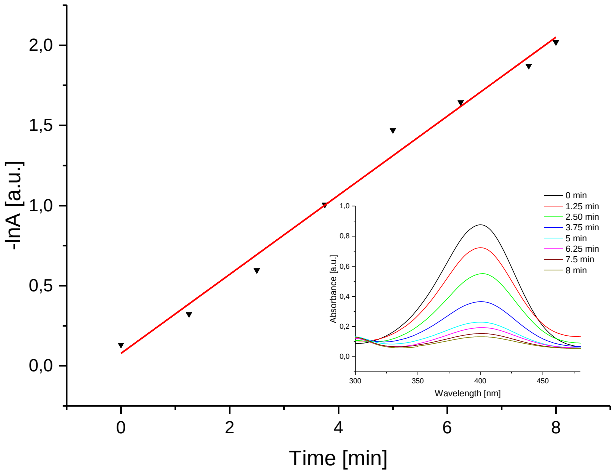

Figure 3.4.6. Logarithmic plot of the absorbance maximum (▼, catalyst: Au on COX50) and the linear fitting to give the k-values from their slope (red line). Inset: UV-Vis spectra showing the reduction of the 4-nitrophenol.

Considering the obtained results, the incorporated nanoparticles can be accessed easily by the used chemicals and can act as reduction catalyst towards 4-nitrophenol. It was also shown that the template diameter plays a crucial part within the encapsulation process and the best results could be achieved with COX50.

3.4.8 Conclusion

Within these studies the facile and convenient preparation and characterization of gold and silver nanoparticle filled hollow carbon spheres (= HCS) is discussed. Therefore, silicon templates (Aerosil® AS90, d ~ 20 nm; Aerosil® OX50, d ~ 40 nm;

Stöber particles, d ~ 200 nm) were coated with the specific single source complexes [$MO_2C(CH_2OCH_2)_3H$] (M = Ag, Au(Ph_3P)). Theses templates were tempered to initiate the nanoparticle formation, which was confirmed by UV-Vis spectroscopy, XRPD and TEM studies reveal crystallite sizes between 14 - 22 nm for silver and 19 - 44 nm for gold. The crystallite size increases with growing template diameter. The thus functionalized SiO_2 particles were then coated with the twin polymer derived from 2,2‘-spiro-bi[4H-1,3,2-benzodioxasiline] (= SBS). After carbonization and removal of all SiO_2 motifs, metal nanoparticle-loaded HCS were obtained. The porous nature of the carbon hull was investigated by nitrogen absorption-desorption isotherms revealing surface areas of ca. 1000 m^2/g for all materials. Compared with the metal-free compounds only a small decrease within the surface area and pore volume was detected. In addition, transmission electron microscopy studies were performed indicating that the HCS with the smallest template diameter shows no encapsulation. The nanoparticles were placed in cavities between the hollow carbon spheres. Complete encapsulation was observed for the COX50 (Aerosil® OX50, d ~ 40 nm) and the CSP (Stöber particles, d ~ 200 nm) material, which is attributed to the small ratio of the particle diameter and template size. To investigate the influence of the different carbon shells, the reduction of methylene blue and 4-nitrophenol as an efficient benchmark system was applied. The silver-containing CAS90 (Aerosil® AS90, d ~ 20 nm) showed the lowest reactivity for reducing methylene blue, while the highest activity was observed for COX50. The CSP exhibits a lower *k* value, since the crystallite size of the incorporated metal nanoparticles (before encapsulation: 22 ± 1 nm, after encapsulation: 58 ± 10 nm) has increased. The same behavior was found for the reduction of 4-nitrophenol. The HCS (CSP) with the largest template showed no reaction, while COX50 displayed the highest reactivity.

In summary, a suitable and straightforward method for the preparation of metal nanoparticles being encapsulated within porous carbon shells by twin polymerization is presented. Since the appropriate metal nanoparticles are accessible for the reduction of methylene blue or 4-nitrophenol, further applications including the aerobic oxidation of alcohols to ketones will be investigated.[197–200] Also the incorporation of other metal particles like palladium and their usage in *C,C* cross coupling reactions will be examined.

3.4.9 Acknowledgement

We are grateful to the Deutsche Forschungsgemeinschaft (FOR 1497 Organic-Inorganic Nanocomposites by Twin Polymerization) for a generous financial support. We like to thank T. Jagemann and M. Hietschold for SEM imaging of different samples, L. Mertens for carrying out the X-Ray powder diffraction studies and A. Kirillova for preparing the Stöber particles and TEM imaging of the metal-nanoparticle functionalized templates thereof.

3.5 Si(OCH$_2$Fc)$_4$: Synthesis, Electrochemical Behavior and Twin Polymerization

C. Schliebe, U. Pfaff, T. Gemming, C. Lochenie, B. Weber and Heinrich Lang

Publiziert in European Journal of Inorganic Chemistry; **2015**,10.1002/ejic.201500464.

Die in diesem Kapitel vorgestellten Synthese sowie Charakterisierung und Interpretation der erhaltenen Ergebnisse wurden vom Autor durchgeführt. Die elektrochemische Charakterisierung wurde von U. Pfaff durchgeführt und interpretiert, T. Gemming hat die HAADF-STEM und TEM-Aufnahmen angefertigt, C. Lochenie fertigte die Mössbauer- und SQUID-Messungen an und die erhaltenen Ergebnisse wurden vom Autor interpretiert.

3.5.1 Introduction

The incorporation of iron or iron oxide nanoparticles within porous carbon or silica matrices has gained great interest, due to the versatile catalytic[201] and magnetic[202] applications of iron. The preparation of such materials can be achieved by impregnation of activated carbon supports with aqueous iron(III) nitrate solutions followed by high temperature treatment.[203] An application of these as-prepared materials indicates their use as anode materials for lithium ion batteries with improved cycle stability.[203] Another iron source is, for example, iron(III) chloride[204–207] or organometallic compounds, including ferrocene which can be decomposed to afford iron-doped carbon materials.[208] Different modifications of carbon materials were thereby obtained, *e. g.*, uniform iron-rich carbon capsules through high pressure pyrolysis.[209] Carbon nano-tubes can also be prepared, for example, by subliming ferrocene and decomposing the vapors in a second furnace at higher temperature.[210] A different approach is given by using polymers containing metallocenes and hence a variety of ferrocene and ferrocene-related compounds were functionalized with side chains and then polymerized under various conditions.[211,212] The group of Manners *et al.* focused on strained silicon *ansa*-ferrocenes and demonstrated the superior polymerization abilities of such species.[213] The versatile processibility of the obtained materials was investigated.[213–217] Iso-structural compounds were also prepared by using different main group elements, for example, Sn, Se, S and organic groups such as $CH_2{=}CH_2$.[218–220]

The recently introduced concept of twin polymerization allows the preparation of organic-inorganic twin polymers,[62] by an acid-catalyzed reaction of, for example, the twin monomer 2,2'-spiro-bi[4H-1,3,2-benzodioxasiline] (= SBS).[72,154] During the polymerization progress a strong mechanistic coupling between the formation of the organic and inorganic phase leads to dispersed silicon dioxide clusters on a nanometer scale within the organic polymer.[71] After carbonization and removal of the inorganic phase with a boiling NaOH solution highly micro-porous materials were obtained. [71] Carbonization followed by carefully oxidation of the organic phase resulted in mainly meso-porous silicon dioxide.[63] This novel methodology was also used for the coating of spherical hard templates to obtain porous carbon capsules.[73,74]

Recently, it was shown that the functionalization of the organic part of the twin monomer has a significant effect on the twin polymerization itself.[70,182] Moreover, a modification of the inorganic component led to the formation of diverse oxide materials as, for example, the oxides of Sn[79,80], Ge[81], Ti[76,155], Zr, Hf[221] and W[78]. In a further study it could be demonstrated that the incorporation of silver nanoparticles during the twin polymerization process is possibile with the addition of silver(I) carboxylates of type $[AgO_2CCH_2{}^{c}C_4H_3S(PPh_3)]$ to SBS, giving homogenous distributed silver nanoparticles in a porous carbon or silica matrix.[222]

We herein report a straightforward synthetic methodology for the preparation of iron oxide-containing porous carbon and silica materials by the usage of a polymerizable ferrocene-based monomer. In addition, the polymerization of the twin monomer $Si(OCH_2Fc)_4$ (Fc = $Fe(\eta^5\text{-}C_5H_4)(\eta^5\text{-}C_5H_5)$) **2** and its copolymerization with SBS will be reported. Also the preparation of iron oxide filled carbon capsules under addition of a silicon dioxide templates is in scope of this article.

3.5.2 Synthesis and characterization of $Si(OCH_2Fc)_4$

The synthesis of $Si(OCH_2Fc)_4$ (Fc = $Fe(\eta^5\text{-}C_5H_4)(\eta^5\text{-}C_5H_5)$) (**2**) was achieved according to Scheme 1. Reduction of commercially available ferrocene carboxaldehyde gave the respective alcohol **1,** [223–225] which on subsequent treatment with $SiCl_4$ in the presence of pyridine afforded $Si(OCH_2Fc)_4$ **2** (Experimental Section). After appropriate work up, the title compound could be isolated as yellow solid in 67 % yield (Scheme 3.5.1).

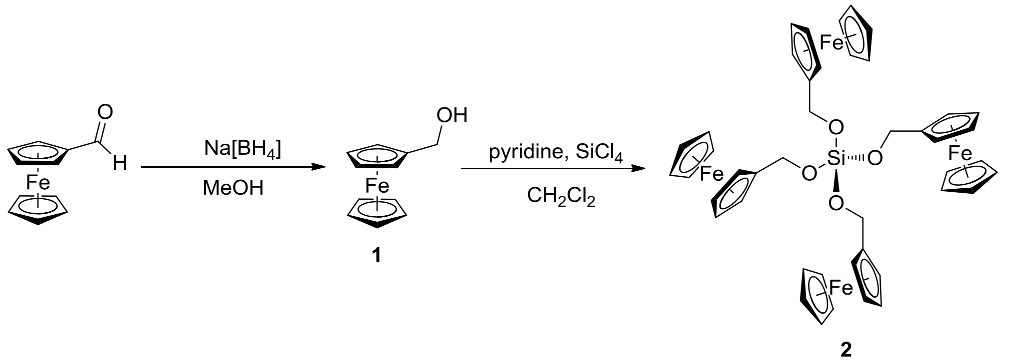

Scheme 3.5.1. Preparation of $Si(OCH_2Fc)_4$ (**2**).

$Si(OCH_2Fc)_4$ (**2**) was characterized by IR, ^1H, $^{13}C\{^1H\}$ and $^{29}Si\{^1H\}$ NMR spectroscopy and ESI mass-spectrometry. The ^1H NMR spectrum of **2** is characterized by a minor shift of the CH_2 protons from 4.32 ppm in **1** to 4.47 ppm in **2**. The respective C_5H_4 protons show, as expected, an AA'XX' [226] spin system with J_{HH} = 1.58 Hz, while for the C_5H_5 group a singlet was observed (4.12 ppm). In the $^{13}C\{^1H\}$ NMR spectrum of **2** the CH_2 carbon atom is shifted from 60.7 ppm in **1** to 62.0 ppm in **2**. A similar behavior is found for the remaining C_5H_4 and C_5H_5 carbon atoms. Considering the ^{29}Si-DEPT spectrum a resonance signal at -82.60 ppm was detected as typical for $Si(OR)_4$ species.[62]

The IR spectrum of **2** is characterized by two very distinct vibrations, which appear at 1104 cm^{-1} ($\nu_{C\text{-}O}$) and 1036 cm^{-1} ($\nu_{Si\text{-}O}$), respectively. These absorptions can be used to monitor the progress of the reaction of **1** with $SiCl_4$ to give **2**.

High resolution ESI mass-spectrometry showed the molecular ion (M^+) at m/z = 888.0360 proving the formation of **2**.

3.5.3 Electrochemical studies of 1 and 2

To get an insight into the electronic properties of **1** and **2**, electrochemical (cyclic voltammetry (= CV) and square-wave voltammetry (= SWV)) (Figure 3.5.1) and UV-Vis/NIR spectroelectrochemical (Figure 3.5.2) measurements have been carried out.

For the measurements dichloromethane solutions containing **1** or **2** (1.0 mmol·L^{-1}) and [^{n}Bu$_4$N][B(C$_6$F$_5$)$_4$] (0.1 mol·L^{-1})[227–229] as supporting electrolyte at 25 °C were applied. All potentials are referenced to the FcH/FcH$^+$ redox couple ($E^{\circ\prime}$ = 0 mV, FcH = Fe(η^5-C$_5$H$_5$)$_2$).[230]

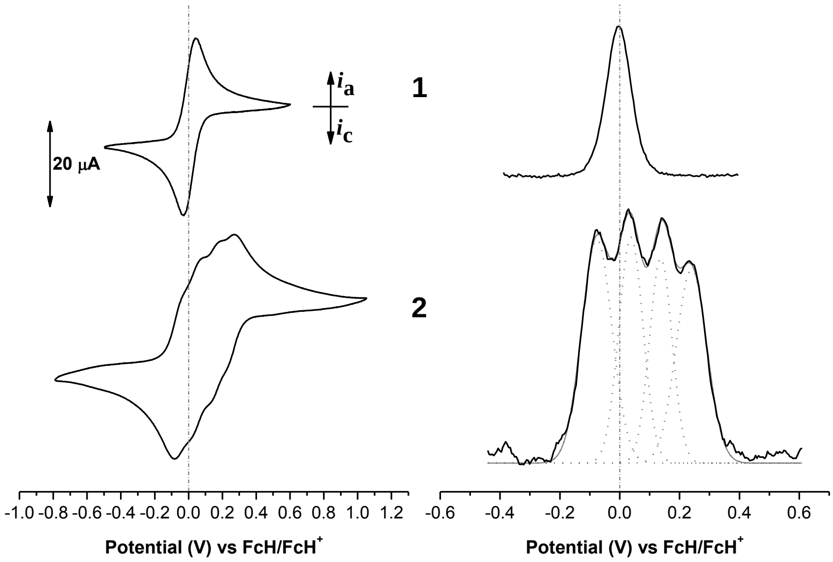

Figure 3.5.1. Left: Voltammograms of a 1.0 mmol·L^{-1} solution of **1** (top) and **2** (bottom) in dichloromethane containing [^{n}Bu$_4$N][B(C$_6$F$_5$)$_4$] as supporting electrolyte (0.1 mol·L^{-1}) at 25 °C (scan rate: 100 mV·s^{-1}). Right: square wave voltammogram (step-height: 25 mV, pulse width: 5 s , amplitude: 5 mV).

In the CV of **1**, as expected, a single reversible one-electron redox event was observed ($E^{\circ\prime}_1$ = 6 mV), while for **2** four redox processes in a close potential range are characteristic (Figure 3.5.1). For a better resolution of these events, SWV was performed and thus the redox potentials for all four ferrocenyl termini could be determined ($E^{\circ\prime}_1$ = -76 mV, $E^{\circ\prime}_2$ = 29 mV, $E^{\circ\prime}_3$ = 144 mV, $E^{\circ\prime}_4$ = 237 mV) (Figure 3.5.1). The integrated peak area of 1 : 1 : 1 : 1 verifies the presence of four closely spaced one-electron processes (Figure 3.5.1). The redox separation ($\Delta E^{\circ\prime}_1$ = 105 mV, $\Delta E^{\circ\prime}_2$ = 115 mV, $\Delta E^{\circ\prime}_3$ = 93 mV) of the symmetrically equal ferrocenyl moieties is caused either by intramolecular electronic interactions between the ferrocenyl/ferrocenium units or by electrostatic repulsion between the oxidized ferrocenyl groups.[231] The latter would be more favorable, because a π-conjugated bridging unit between the redox-active Fc groups, which is beneficial for an intramolecular electron transfer, is non-existent.[232] To prove this, spectroelectrochemical UV-Vis/NIR experiments were carried out in an

OTTLE (= Optically Transparent Thin Layer Electrochemistry) cell.[233] The stepwise increase of the potential (-200 to 700 mV) allowed the *in situ* generation of cationic $\mathbf{2}^{n+}$ (n = 1, 2, 3, 4) from neutral **2** (Figure 3.5.2).

As expected, neutral **2** shows no absorption in the NIR region (1000 – 3000 nm). Within successive oxidation, increasing absorptions below 750 nm (UV-Vis region) were observed, including d–d transitions of the ferrocenyl substituents[234] and LMCT (= Ligand-to-Metal-Charge-Transfer) from the cyclopentadienyl substituent to the iron atom.[231] Additionally, a very weak excitation (<100 $L\cdot mol^{-1}\cdot cm^{-1}$) at 2500 nm was detected, which can be assigned to the forbidden metal-centered ligand-field (LF) electronic transition (Figure 2). This excitation is a typical indication for the formation of a 17-valence electron ferrocenium species.[235,236] The absence of an IVCT absorption (= Inter-Valence-Charge-Transfer) is attributed to the structural properties of **2** excluding π-conjugation and validates that mainly electrostatic interactions are responsible for the observed redox splitting between the equally charged redox centres in 2^{n+} (n = 2, 3, 4). Therefore, compound **2** can be classified as a class I system according to Robin and Day.[237]

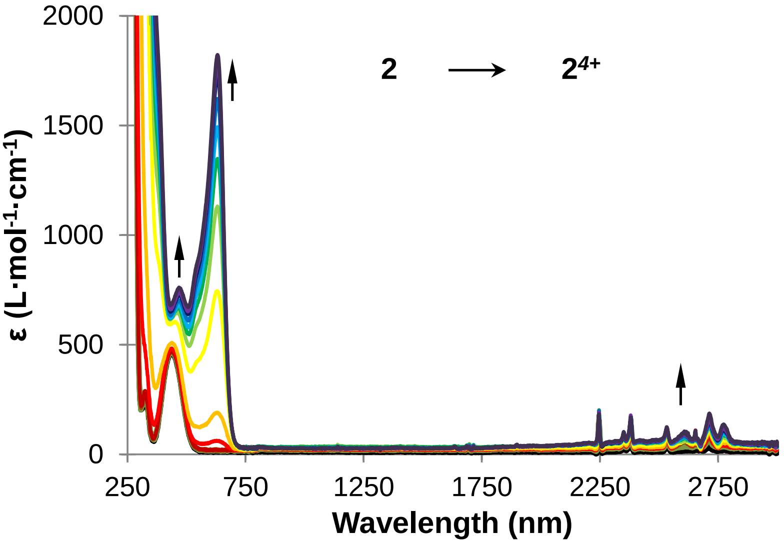

Figure 3.5.2. UV-Vis/NIR spectra of **2** at rising potentials vs Ag/AgCl (−200 to 700 mV). Measurement conditions: 25 °C, dichloromethane, 0.1 $mol\cdot L^{-1}$ $[^{n}Bu_4N][B(C_6F_5)_4]$ as supporting electrolyte (arrows indicating increasing potential).

3.5.4 Thermal characterization of 2

The ferrocene twin monomer **2** was characterized by differential scanning calorimetry (Figure 3.5.3). Melting of **2** occurs as an endothermic process at 128 °C, followed by a strong exothermic process at 210 °C. The nature of the latter event was investigated by thermogravimetric analysis, which reveals the release of volatile materials with $\Delta m = 4.23$ %. This weight loss can be explained by a thermally induced condensation reaction. The volatile products, which were formed during the heating process of **2**, were identified by TG-MS coupling experiments (Figure 3.5.3). Between 200 - 230 °C the evaporation of water (m/z = 18) was observed, indicating the condensation of **2**.

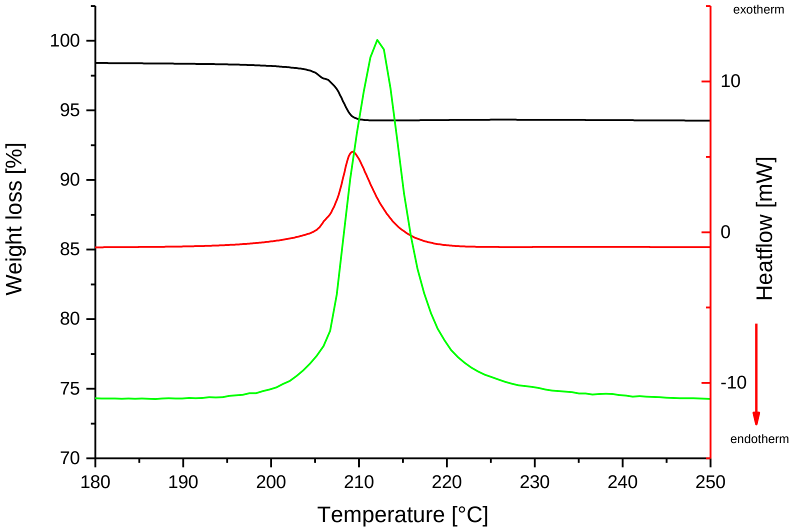

Figure 3.5.3. Thermogravimetric- (= TG, black) and differential scanning calorimetric traces (= DSC, red) of **2**, showing an exothermic process at 210 °C with simultaneous weight loss (see ESI for complete DSC and TG traces). TG-MS (green) study performed with **2**, showing the evaporation of water (m/z 18) during the exothermic process starting at 210 °C (40 – 800 °C, 10 K/min, Ar 20 mL/min).

3.5.5 Homopolymerization of 2

Homopolymerization experiments were carried out by suspending **2** in diisopropylnaphthalene and heating this mixture to 230 °C. After passing the melting point of **2** (128 °C) a clear solution formed, which darkened just below 200 °C. While reaching the condensation temperature of **2** (210 °C), water evaporated and a brown solid precipitated (see Experimental Section for detailed procedure).

The obtained hybrid material was further investigated by solid state $^{13}C\{^1H\}$ CP-MAS NMR spectroscopy (Figure 3.5.4). The signals for the ferrocenyl moieties C_5H_5 and C_5H_4 were observed at ca. 90 and 70 ppm. In contrast to monomeric **2**, no resonance signal at 62 ppm for the **C**H_2OSi groups could be detected, which verifies complete conversion of **2**. The new signal at 29 ppm can be assigned to the formation of a bridging Fc**C**H_2Fc motif. A similar NMR resonance signal for this structural motif was observed for diferrocenyl methane.[238]

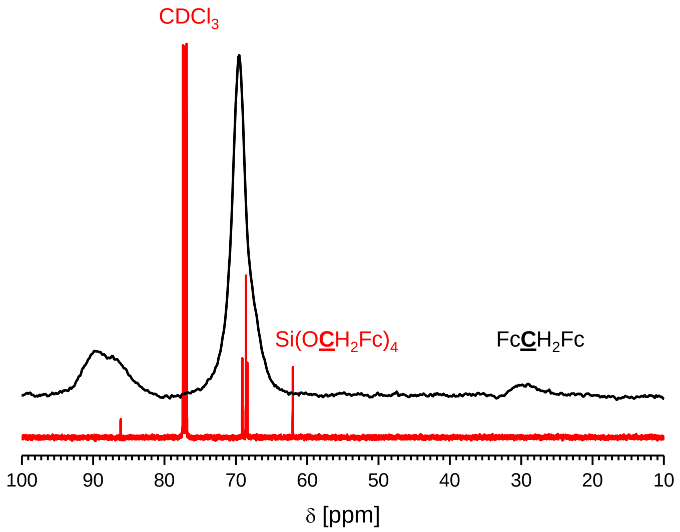

Figure 3.5.4. $^{13}C\{^1H\}$ CP-MAS spectrum of the hybrid material obtained by thermal twin polymerization of **2** (black line (Fc = $(Fe(\eta^5\text{-}C_5H_4)(\eta^5\text{-}C_5H_5))$), 100.6 MHz, 20 kHz, reference: $Si(SiMe_3)_4$) in comparison with the $^{13}C\{^1H\}$ NMR spectrum of **2** in $CDCl_3$ (red line) (see Experimental Section for an detailed assignment of signals).

The solid state NMR characterization of the incorporated SiO_2 network was not possible, since the amount of silicon within **2** is too small (3.2 %). According to that, we have carried out REM/EDX and TEM studies to determine the incorporated amount of silicon. It becomes obvious that silicon is homogeneously incorporated within this hybrid material, which can be seen from the EDX pattern (Figure 3.5.5). Since the oxygen signals observed are homogeneously distributed over the total sample, we suggest that a silicon dioxide matrix is formed. The TEM images of the examined polymer particle (Figure 3.5.5) shows an overall homogenous texturing with particles exhibiting a higher contrast than the surrounding matrix. This is most probably attributed to the formed silicon dioxide clusters during the twin polymerization process. In comparison with other twin polymers, for example, 2,2‘-spiro-bi[4H-1,3,2-benzodioxasiline],[63] the nanostructuring is more distinctive, due to the higher amount of silicon within this twin monomer.

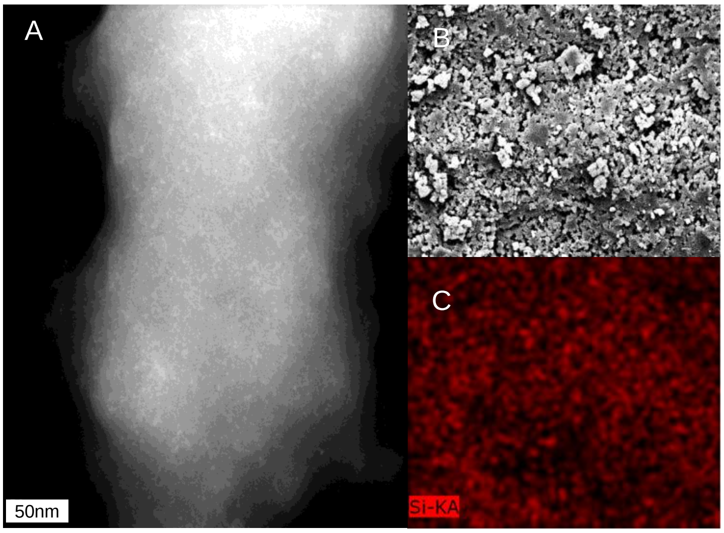

Figure 3.5.5. HAADF-STEM image of the obtained hybrid material from **2** by thermal polymerization (A), REM image (B) and EDX analysis (C) showing the homogenous distribution of silicon within the sample.

3.5.6 Copolymerization of 2 with 2,2‘-spiro-bi[4H-1,3,2-benzodioxasiline]

The copolymerization of **2** and 2,2‘-spiro-bi[4H-1,3,2-benzodioxasiline] (= SBS) was performed under acidic conditions with $MeSO_3H$, since thermal initiation is not suitable, due to the higher polymerization temperature of SBS (240 °C).[69] Therefore, SBS and **2** were dissolved in dichloromethane and the yellow mixture was heated to reflux. Then the initiator dissolved in 1 mL of dichloromethane was added and the solution becomes turbid and a pale green solid precipitated.

After appropriated work up, the obtained hybrid material was investigated by $^{13}C\{^1H\}$ CP-MAS and $^{29}Si\{^1H\}$ CP-MAS NMR spectroscopy. All expected resonance signals for the phenolic resin were observed, as typical for a twin polymer derived from SBS (ESI).[63] The $^{29}Si\{^1H\}$ CP-MAS NMR spectrum showed Q_3 and Q_4 signals, which are characteristic for the formed SiO_2 network.[63] However, the carbon signal of the ferrocenyl component could not be seen, since during the twin polymerization process paramagnetic species were formed from **2**. These paramagnetic impurities have an influence on the proton decoupling, which results in spectra with lower resolution.[239,240] The incorporation of ferrocenyl units during the copolymerization process was confirmed by AAS measurements and an iron content of 3.8 % was found. This value was also supported by EDX experiments (3.6 %) and a homogeneous distribution over the total sample was achieved (ESI).

3.5.7 Preparation of iron oxide-containing porous carbon/silica materials

The hybrid material obtained by acid-initiated copolymerization of **2** and SBS was carbonized under a constant flow of argon and then oxidized in air to obtain the inorganic silicon dioxide matrix, or refluxed with a 5 M sodium hydroxide solution to remove the inorganic SiO_2 network giving a porous carbon material (see ESI for a detailed procedure).

The porous nature of the carbon and silica material was investigated by N_2 adsorption/desorption isotherms. A IUPAC type I isotherm[139] for the carbon material was obtained, which indicates a mainly micro-porous nature of this sample (Figure 3.5.6). The silica material exhibits a type IV isotherm according to IUPAC[139] with a small hysteresis, which is mostly caused by capillary condensation within meso-porous structures. The surface areas and pore volumes were calculated using DFT methods.[190] The measured values are given in Figure 3.5.6 and are lower than compared with the pure carbon or silica materials obtained from the SBS twin polymer. This behavior can be explained by the incorporated iron oxide nanoparticles, since they were mostly situated within the porous structure and therefore, are lowering the surface area.[222]

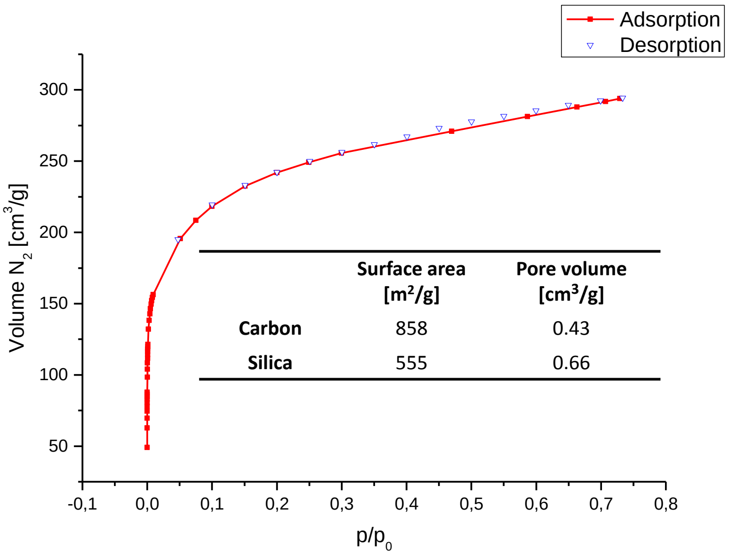

	Surface area [m^2/g]	Pore volume [cm^3/g]
Carbon	858	0.43
Silica	555	0.66

Figure 3.5.6. N_2 adsorption/desorption isotherm of the porous carbon material measured at 77 K. Inset: Table with the obtained surface areas and pore volumes for the as-prepared carbon and silica materials (see ESI for further isotherms and pore size distributions).

AAS experiments proved an iron content for the carbon material of 7.1 % and for the silica material of 15.0 %, respectively. These values were confirmed by EDX measurements (ESI, carbon material: 7.1 %, silica compound: 13.1 %). The iron distribution within the carbon or silica matrix was homogeneous, since the EDX analysis showed no agglomeration. The incorporated nanoparticles were detected by TEM studies (Figure 3.5.7). The HAADF-STEM images of the carbon material exhibit a z-contrasting, which is caused by the heavier elements like iron, for example.

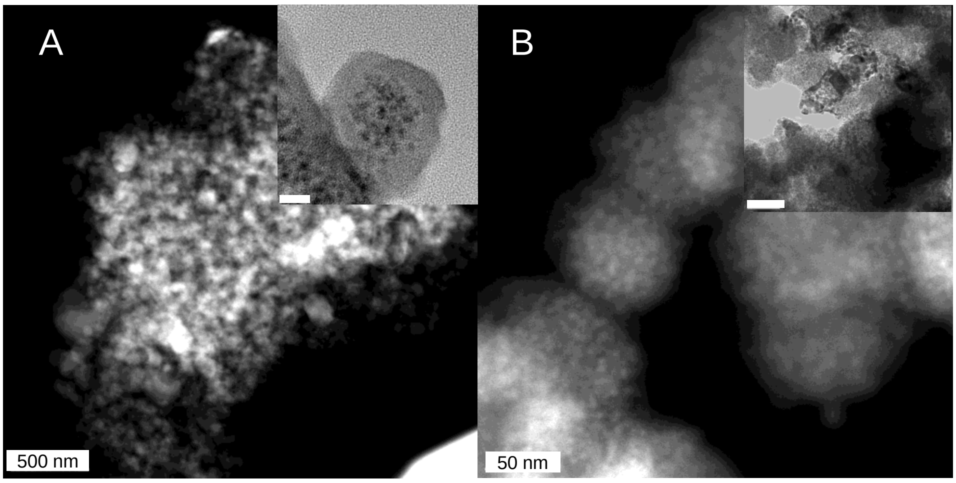

Figure 3.5.7. HAADF STEM image of the carbon (A) and the silica material (B). Bright field TEM images of the specific materials are displayed as insets (scale bar inset A: 20 nm, scale bar inset B: 100 nm).

Within standard bright field TEM images (Inset, Figure 3.5.7) some darker structures are observed, however, with no separation to the surrounding material, making a particle size determination inaccurate. The same observation was made for the appropriate silica material. The bright field TEM images exhibit a homogenous pattern, the HAADF images reveal some separated areas with a higher z-contrast, which could probably refer to iron oxide-rich areas. As noticed above for the nanoparticles incorporated within the porous carbon material, the particle size determination is also not possible for the silica material, but the observable structures are ≤ 10 nm in both materials.

The oxidation state of the incorporated iron could not be determined by XRPD studies, since the particles are amorphous (see ESI). Therefore, Mössbauer experiments were carried out and the result thereof is shown in Figure 3.5.8. The fitting of both signals was done by applying Lorentzian curves at the experimental data. The nanoparticles within the matrix are rather small as indicated by TEM and have a nonnegligible surface area, which causes a line broadening (different iron sites on the surface that contribute to the overall spectrum). Therefore, the herein presented fits are approximations.[241] However, comparing the obtained isomer shifts of the carbon sample (0.32 mm/s) with literature results, it would fit to either Fe_3C (Fe_3C = 0.29 mm/s)[242] or Fe_2O_3 (0.37 mm/s). With the obtained parameters (a quadrupole splitting of 0.71 mm/s was determined) it is also not possible to distinguish between Fe_2O_3 and Fe_3O_4.[243] This would have been of interest, as the iron oxide phase strongly depends on the size of the particles.[244] Hence no conclusion can be made if the incorporated nanoparticles are Fe_2O_3’ Fe_3O_4, and/or Fe_3C, respectively.

Due to the preparation under an oxidizing atmosphere and at elevated temperature, the incorporation of iron oxides (Fe_2O_3 or Fe_3O_4) within the sample is more likely.

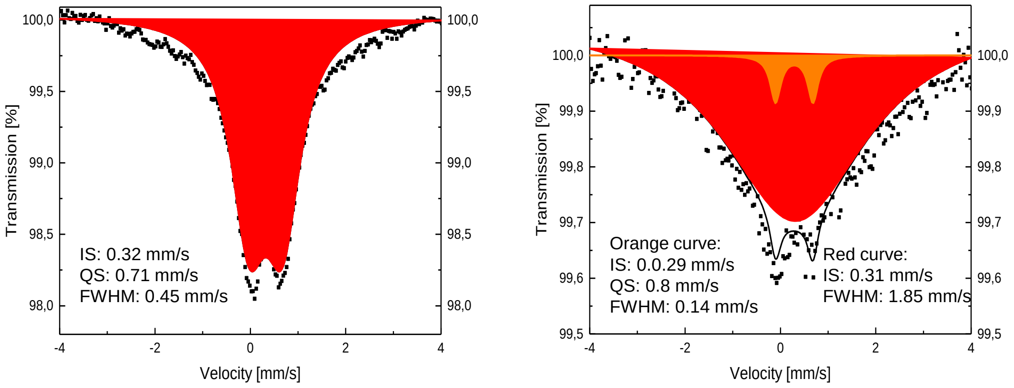

Figure 3.5.8. Results of the Mössbauer experiments for the carbon (left) and silica sample (right) and the fitting of the experimental data (IS: Isomer Shift, QS: Quadrupole Splitting, FWHM: Full Width at Half Maximum). The very wide line widths of the Mössbauer spectra are due to the very small size nanoparticles.

The magnetic behavior of these materials was investigated by SQUID experiments (Figure 3.5.9). The silica material showed superparamagnetic behavior [245,246]. In contrast to this, the curve progression of the carbon material indicates a paramagnetic behavior that does, however, not follow the Brillouin function. Since, superparamagnetic iron carbide nanoparticles were obtained by carbonization of ferrocene[208] or $FeCl_3$.[247] According to the Mössbauer results, the particles consist of Fe_2O_3 and Fe_3C, this is an indication that the silica material contains Fe_3C. Based on the Mössbauer results, no explanation can be given for the differences in magnetism. The different possible iron species cannot be distinguished and the formation of superparamagnetic nanoparticles is possible in all cases. Furthermore, the thus prepared particles are not crystalline, which will also influence their magnetic behavior. [208,247]

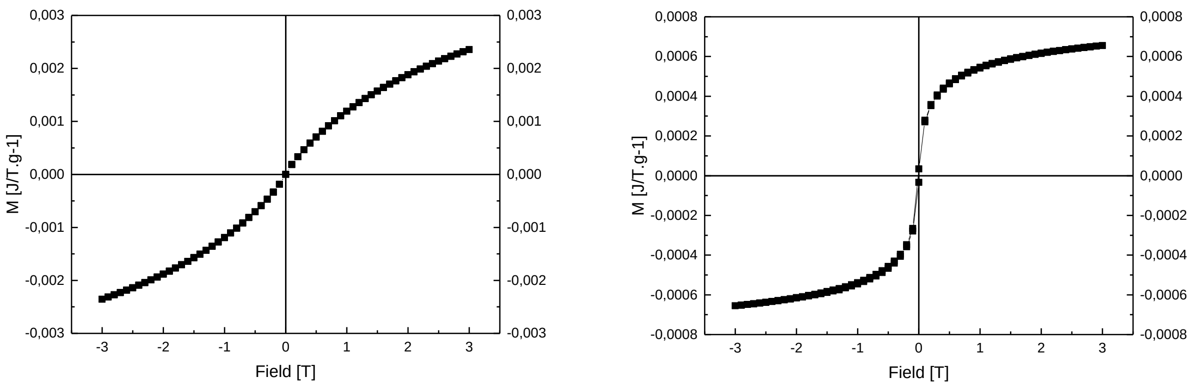

Figure 3.5.9. Magnetization curves obtained by SQUID measurements for the carbon (left) and the silica sample (right, measured at 300 K).

3.5.8 Preparation of iron oxide-containing porous carbon capsules

The coating abilities of **2** and SBS upon spherical silica templates were investigated (Scheme 3.5.2).[73] Therefore, plain silica particles (200 nm in diameter) were functionalized with methanesulfonic acid and suspended in toluene. After addition of the monomer mixture the substrate suspension changed its color to green and upon stirring overnight the coated templates precipitated. The thus prepared material was carbonized in argon atmosphere at 800 °C for 2 h and after cooling it to ambient temperature the incorporated SiO_2 was removed by refluxing the carbonized material in a 5 M NaOH solution (ESI).

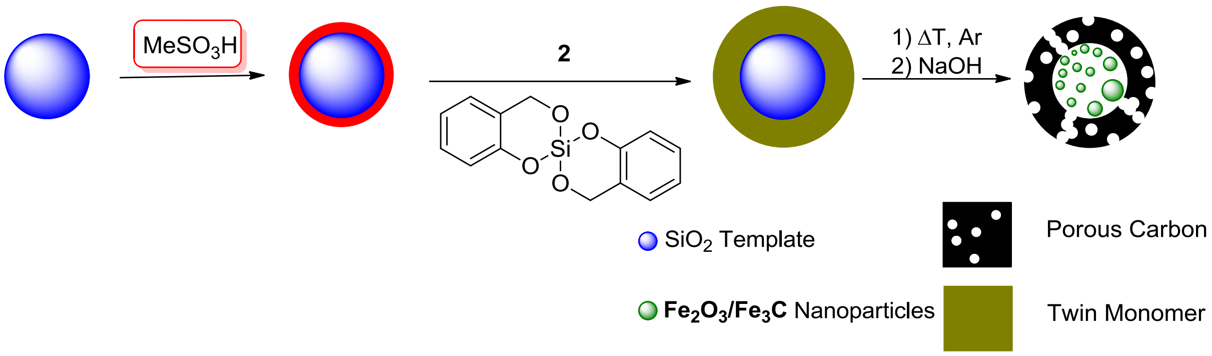

Scheme 3.5.2. Preparation of Fe_2O_3 filled porous carbon capsules.

The obtained carbon capsules were characterized by N_2 adsorption/desorption isotherms. At a first glance, the observed isotherm looks like a type I isotherm according to IUPAC[139] (Figure 3.5.10), which is caused by the mainly micro-porous carbon obtained from the twin polymer of SBS. However, considering the desorption part of the observed isotherm a small hysteresis typical for type IV isotherms[139] could be noticed. This is probably caused by cavities formed between connecting capsules.

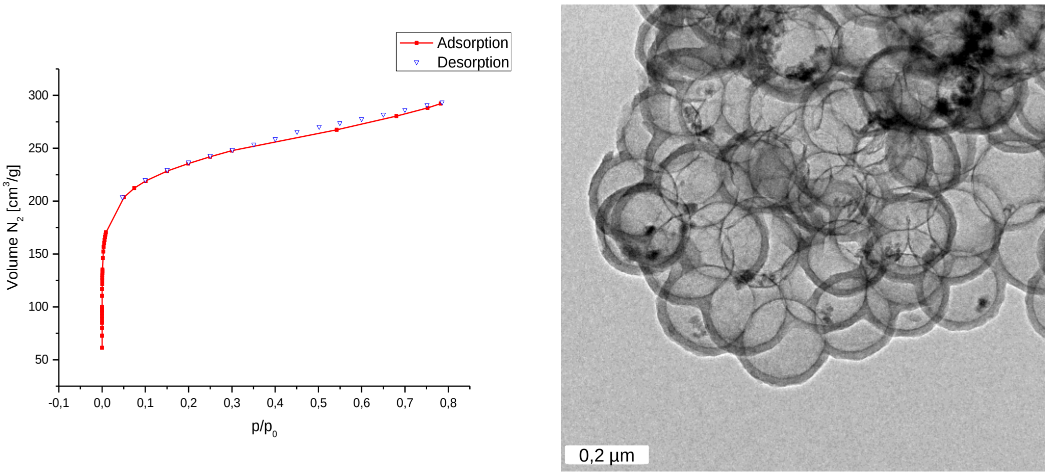

Figure 3.5.10. Left: N_2 adsorption/desorption isotherms of the obtained carbon capsules. Right: bright field TEM images showing the prepared porous carbon capsules with the incorporated nanoparticles.

The calculated surface area (915 m^2/g) and the obtained pore volume (0.42 cm^3/g) are smaller than the values for the reference material (surface area = 1180 m^2/g, pore volume = 0.48 cm^3/g) derived by using only 2,2'-spiro-bi[4H-1,3,2-benzodioxasiline] as twin monomer.

TEM studies reveal the formation of spherical carbon capsules, but otherwise as expected, the incorporated nanoparticles are found inside the capsules and not as supposed in the hull. This is most probably admitted by the finite carbon hull thickness, since within the bulk material the incorporated nanoparticles are even better separated. An iron content of 5 % was determined by AAS measurements.

Additional Mössbauer and SQUID experiments showed that the incorporated nanoparticles are of the same nature as those obtained by copolymerization of **2** with SBS and therefore also exhibiting a paramagnetic behavior (Figure 3.5.11).

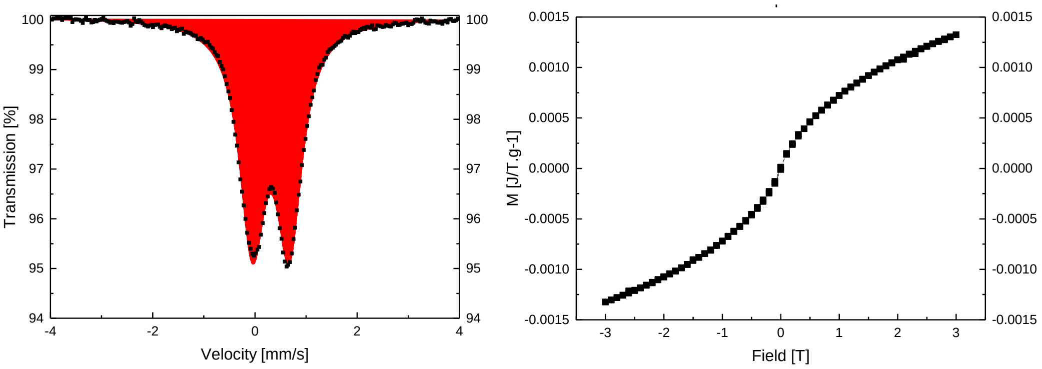

Figure 3.5.11. Results of the Mössbauer experiments with the fitting of the experimental data (IS = 0.31 mm/s, QS = 0.72 mm/s, FWHM = 0.30 mm/s) for the iron containing carbon capsules (left) and the respective SQUID experiments (right).

3.5.9 Conclusion

Herein, the preparation and characterization of a ferrocene containing twin monomer of type $Si(OCH_2Fc)_4$ (Fc = $Fe(\eta^5\text{-}C_5H_4)(\eta^5\text{-}C_5H_5)$) (**2**) is presented. Compound **2** was synthesized by the reaction of four equivalents $FcCH_2OH$ with $SiCl_4$ in presence of pyridine. Silicon orthoester **2** was electrochemically characterized showing four reversible redox processes ($E_1^{\circ\prime}$ = -76 mV, $E_2^{\circ\prime}$ = 29 mV, $E_3^{\circ\prime}$ = 144 mV, $E_4^{\circ\prime}$ = 237 mV). Further investigation by UV-Vis/NIR spectroelectrochemistry proved that the redox separation is caused be electrostatic repulsion of the oxidized species. The thermal behavior of **2** was investigated by differential scanning calorimetry (= DSC), thermogravimetry (= TG) and mass spectrometry-coupled TG (= TG-MS). DSC revealed a strong exothermic peak at 210 °C, which could be verified by TG and TG-MS experiments as thermally induced condensation. As consequence thereof, **2** was polymerized under thermal conditions in a high boiling solvent (220 °C, diisopropyl nahphtalene), giving a brown solid material. Investigation of this material by solid state $^{13}C\{^1H\}$ CP-MAS NMR spectroscopy reveals the transformation of the othoester moiety of the monomer (**C**H_2OSi) to a Fc**C**H_2Fc motif as indicated by the resonance signal at 29 ppm. The incorporated silicon dioxide network, which is formed during the polymerization process, could not be observed by solid state NMR techniques, due to its low concentration, but was confirmed by EDX measurements. As shown in the appropriated TEM images, the typical micro-structuring of twin polymers was not observed, [63] which is also a consequence of the low amount of silicon. However, **2** undergoes a thermally induced twin polymerization and we suggest to consider this monomer type as a borderline system for twin polymerization. The copolymerization of **2** and SBS under acidic conditions was investigated, producing a pale green solid material. After carbonization and oxidation or removal of the SiO_2 with sodium hydroxide, porous carbon or silica materials were obtained. Both materials have a rather high surface area (858 m^2/g, carbon; 555 m^2/g, silica). Attempts were made to determine the identity of the incorporated iron containing nanoparticles by Mössbauer studies showing that for both materials this is not possible. SQUID studies revealed the superparamagnetic behavior of the nanoparticles incorporated in the silica material, while the carbon compound remains paramagnetic. The monomeric mixture of **2** and SBS was further used for the incorporation of iron-containing nanoparticles within porous carbon spheres.

The thus accessible magnetic carbon materials will be further investigated, especially the incorporation of catalytic active metal nanoparticles, such as Pd or Pt will be studied. Such materials are of interest as catalysts in, for example, *C,C* cross coupling reactions.

3.5.10 Experimental Section

General. All reactions were carried out under an atmosphere of argon using standard Schlenk techniques. Dichloromethane was purified by distillation from calcium hydride. *n*-Hexane was taken from a M. Braun SBS-800 purification system (stationary drying with molecular sieve columns 3 Å). In addition, pyridine was dried by refluxing over potassium hydroxide and then distilled and stored over molecular sieve 3 Å. Ferrocene carboxaldehyde and diisopropylnaphthalene were purchased by commercial suppliers, the respective alcohol **1**[224] and 2,2’-spirobi[4*H*-1,3,2-benzodioxasiline][63] were prepared according to published procedures.

^1H NMR (500.3 MHz) and $^{13}C\{^1H\}$ NMR (125.8 MHz) spectra were recorded with a Bruker Avance III 500 spectrometer at 298 K. Chemical shifts δ are reported in ppm (parts per million) using undeuterated solvent residues as internal standard (benzene-d_6: ^1H, 7.16 ppm and $^{13}C\{^1H\}$, 128.06 ppm). Solid state $^{13}C\{^1H\}$ NMR experiments were conducted using cross polarization (CP) and magic angle spinning (MAS) with spinning frequencies of 12.5 kHz or 20 kHz. Infrared spectra were recorded with a FT-IR Nicolet 200 spectrometer. The melting point of **2** was determined with a Gallenkamp MFB 595 010 M melting point apparatus. Microanalysis was performed with a Thermo FLASHEA 1112 Series instrument. The mass spectrum of **2** was recorded with a Bruker micrOTOF QII system. SEM images and EDX analyses were performed with a Phillips NanoNovaSEM. TEM images were recorded with a Fecnai FC20 equipment with 200 kV accelerating voltage. Gas adsorption-desorption measurements were carried out using an Autosorb IQ2 system. Thermal analyses were performed with a Mettler Toledo TGA/DSC1/1600 system with a MX1 scale. Thermal carbonizations and oxidations were carried out in a Carbolite Tube Furnace MTF 12/38/400.

Electrochemistry. Measurements on 1.0 mmol•L^{-1} solutions of the analyte in anhydrous dichloromethane containing 0.1 mol•L^{-1} of $[^n\mathrm{Bu}_4\mathrm{N}][\mathrm{B}(\mathrm{C}_6\mathrm{F}_5)_4]$ as supporting electrolyte were conducted under a blanket of purified argon at 25 °C utilizing a Voltalab 10 electrochemical laboratory. A three electrode cell, which includes a Pt auxiliary electrode, a glassy carbon working electrode (surface area 0.031 cm^2) and an Ag/Ag$^+$ (0.01 mol•L^{-1} AgNO_3) reference electrode mounted on a Luggin capillary was used. The working electrode was pretreated by polishing on a Buehler microcloth first with a 1 µm and then with a 1/4 µm diamond paste. The reference electrode was built from a silver wire inserted into a solution of 0.01 mol•L^{-1} $[\mathrm{AgNO}_3]$ and 0.1 mol•L^{-1} $[^n\mathrm{Bu}_4\mathrm{N}][\mathrm{B}(\mathrm{C}_6\mathrm{F}_5)_4]$ in acetonitrile in a Luggin capillary with a Vycor tip. This Luggin capillary was inserted into a second Luggin capillary with a Vycor tip filled with a 0.1 mol•L^{-1} dichloromethane solution of $[^n\mathrm{Bu}_4\mathrm{N}][\mathrm{B}(\mathrm{C}_6\mathrm{F}_5)_4]$.[228,229,232,248–253] Successive experiments under the same experimental conditions showed that all formal reduction and oxidation potentials were reproducible within ±5 mV. Experimentally potentials were referenced against an Ag/Ag$^+$ reference electrode but results are presented referenced against ferrocene[254,255] (FcH/FcH$^+$ couple = 220 mV vs Ag/Ag$^+$, ΔEp = 61 mV; FcH = $\mathrm{Fe}(\eta^5\text{-}\mathrm{C}_5\mathrm{H}_5)_2$) as an internal standard as required by IUPAC.[256] When decamethylferrocene (Fc* = $\mathrm{Fe}(\eta^5\text{-}\mathrm{C}_5\mathrm{Me}_5)_2$) was used as an internal standard, the experimentally measured potential was converted into E vs FcH/FcH$^+$ (under our conditions the Fc*/Fc*$^+$ couple was at -614 mV vs FcH/FcH$^+$, ΔEp = 60 mV).[231] Data were then manipulated on a Microsoft Excel worksheet to set the formal redox potentials of the FcH/FcH$^+$ couple to E°′ = 0.00 V. The cyclic voltammograms were taken after typical two scans and are considered to be steady state cyclic voltammograms in which the signal pattern differs not from the initial sweep.

UV-Vis/NIR Spectroelectrochemistry. The spectroelectrochemical measurements of compound **2** (2.0 mM) in anhydrous dichloromethane containing [$^{n}Bu_4N$][$B(C_6F_5)_4$] (0.1 M) as the supporting electrolyte were performed in an OTTLE (= Optically Transparent Thin Layer Electrochemistry) cell with quartz windows (UV-Vis/NIR)[257] at 25 °C. Between the spectroscopic measurements the applied potentials have been increased stepwisely using step heights of 25, 50 or 100 mV. At the end of the measurements the analyte was reduced at -500 mV for 15 min and an additional spectrum was recorded to prove the reversibility of the oxidations.

^{57}Fe Mössbauer Spectrometry: ^{57}Fe Mössbauer spectra were recorded in transmission geometry on a constant-acceleration using a conventional Mössbauer spectrometer with a 50 mCi ^{57}Co(Rh) source. The samples were sealed in the sample holder under an argon atmosphere. The spectra were fitted using Recoil 1.05 Mössbauer Analysis Software. The isomer shift values are given with respect to an α-Fe reference at room temperature.

Magnetic measurements: Magnetization data were collected with a Quantum Design MPMSR-2 SQUID magnetometer over an applied field range of -3 to 3 T at 300 K in the settle mode. The samples were placed in gelatine capsules held within a plastic straw. The data were corrected for the diamagnetic magnetization of the sample holder.

Synthesis of Tetraferrocenylmethoxysilane (2). A mixture of 3.01 g (13.95 mmol) of **1** and 1.47 g (18.6 mmol, 1,5 mL) of pyridine were dissolved in 20 mL of dichoromethane. This mixture was cooled to 0° C with an ice/brine bath. Afterwards, 0.39 g (2.3 mmol, 0.27 mL) of silicon tetrachloride diluted in 10 mL of dichloromethane were added dropwise with a syringe within 15 min under stirring. The formed suspension was warmed to ambient temperature, stirred for 1 h and all volatiles were removed *in vacuo*. The resulting yellow solid was transferred to a soxhlet extractor and extracted with abs. *n*-hexane until the extract was colorless. The remaining solution was then cooled to -35 °C for 12 h and the precipitating microcrystalline product was collected and washed thrice with *n*-hexane (10 mL each) giving a bright yellow solid (1.36 g, 67%). Melting point: 121 °C; Elemental analysis calculated for $C_{44}H_{44}Fe_4O_4Si$: C 59.49, H 4.99; found : C 59.25, H 4.98; IR (KBr, cm^{-1}): 3074 w [ν(CH_{aromat})], 2945 w [$\nu_{as}(CH_2)$] , 2883 w [ν_s (CH_2)], 1467 m [$\delta(CH_2)$] , 1104 m [ν (C-O)], 1036 s [ν (Si-O)]; ^{1}H NMR ($CDCl_3$, ppm): 4.47 (s, 2H, $C\mathbf{H}_2$), 4.24 (pt, 2 H, $^cC_5\mathbf{H}_4$), 4.14 (pt, 2 H, $^cC_5\mathbf{H}_4$), 4.12 (s, 5 H, $^cC_5\mathbf{H}_5$); $^{13}C\{^1H\}$ NMR ($CDCl_3$, ppm): 86.15 (ipso $^c\mathbf{C}_5H_4$), 69.11 ($^c\mathbf{C}_5H_4$), 68.59 ($^c\mathbf{C}_5H_5$), 68.38 ($^c\mathbf{C}_5H_4$), 62.02 ($O\mathbf{C}H_2$); $^{29}Si\{^1H\}$-DEPT NMR ($CDCl_3$, ppm): -82.60; MS: calc. ($C_{44}H_{44}Fe_4O_4Si$): $[M]^+$ = 888.0406; found: $[M]^+$ = 888.0360.

Thermal polymerization of 2. The twin monomer **2** (0.72 mg, 0.82 mmol) was suspended in 20 mL of diisopropylnaphthalene and upon heating a clear solution was obtained. Heating was continued to 230 °C and after passing 210 °C a brown solid precipitated. The mixture was kept at this temperature for 15 min and then cooled to ambient temperature. The formed solid was filtered off and washed thrice with dichloromethane (30 mL each) and dried *in vacuo*, yielding 0.39 mg (54%).

Copolymerization of 2 with SBS. A mixture of 3.0 g (12 mmol) of SBS and 1.2 g (1.4 mmol) of **2** in 100 mL of dichloromethane was heated to 40 °C. Then 0.16 mL (2.49 mmol) of methanesulfonic acid diluted in 0.8 mL of dichloromethane were added via a syringe in a single portion. The solution get turbid and a pale green solid precipitated after 12 h of reflux. The solid material was collected by filtration and washed twice with dichloromethane (20 mL each). After drying *in vacuo,* 3.1 g (74%) of a pale green colored solid was obtained.

Template coating with 2 and SBS. The spherical SiO_2 template (1.0 g, 16,6 mmol) was suspended in 200 mL of dichloromethane and sonicated until a homogeneous suspension was formed. Afterwards, 0.16 mL (2.5 mmol) of methanesulfonic acid was added in a single portion and the mixture was stirred for 15 min at ambient temperature. Then, the solvent was evaporated *in vacuo* and the remaining solid was suspended in toluene (200 mL) and sonicated until a homogeneous suspension was formed. To this mixture, 2.0 g (7.3 mmol) of SBS and 0.8 mg of **2** (0.9 mmol) dissolved in 50 mL of toluene were added dropwise. After 15 min of stirring at ambient temperature the suspension turned pale green indicating the beginning of the twin polymerization. Stirring was conducted for 8 h, whereby the hybrid material-coated templates precipitated. They were collected by filtration and washed thrice with dichloromethane (50 mL each) and were then dried *in vacuo*, yielding 3.7 g (96%) of a pale green colored solid.

Carbonization and SiO_2 removal. In a typical procedure, 2.0 g of the specific compound (SBS and **2**, or respective coated templates) was placed in a tube furnace and carbonized at 800 °C (50 K/min) for 15 min under a continuous flow of argon. The removal of the incorporated SiO_2 (from the twin monomer and the template) was achieved by refluxing the carbonized material in 50 mL of a 5 M NaOH solution for 8 h. Afterwards, the SiO_2-free compounds were filtered off and washed with hot water (300 mL, until pH ~7 was reached) and then with 50 mL of deionized water followed by 30 mL of acetone and 50 mL of diethyl ether. The respective carbon materials were dried *in vacuo*.

General oxidation procedure. In a typical experiment, the appropriate hybrid material was transferred to an aluminium oxid crucible and placed in a quartz tube furnace. Under a continuous flow of Ar the material was heated to 800 °C (50 K/min) and kept at this temperature for 15 min. After cooling to ambient temperature, the sample was heated again under a continuous flow of air to 450 °C (50 K/min) and kept at this temperature for 48 h, resulting in an orange colored solid.

Acknowledgement. We are grateful to the Deutsche Forschungsgemeinschaft (FOR 1497 Organic-Inorganic Nanocomposites by Twin Polymerization) for a generous financial support. We thank T. Jagemann and Prof. Dr. M. Hietschold for SEM imaging of different samples, Dr. C. Georgi and J. Noll for carrying out the thermogravimetric measurements, B. Kempe and Dr. R. Buschbeck for mass spectrometry measurements, Dr. A. Seifert for the solid state NMR analytic and A. Kirillova for preparing the Stöber particles.

Detailed synthetic procedures and additional analytical data, further solid state NMR, TG traces, NIR spectra, TEM/REM-EDX images and N_2-adsorption/desorption measurements are available online free of charge from the publishers homepage.

3.6 Nitrogen-containing Porous Carbon Materials by Twin Polymerization

C. Schliebe, J. Noll, T. Gemming, A. Seifert, S. Spange, D. Lehmann, D. R. T. Zahn, and H. Lang

Die in diesem Kapitel vorgestellten Ergebnisse sind Teil einer gemeinsamen Publikation mit der Juniorprofessur für Theoretische Chemie. Dabei wurden vom Autor die Synthese und Charakterisierung der in diesem Kapitel vorgestellten Verbindungen durchgeführt. Die gezeigten TG-MS Messungen wurden von J. Noll durchgeführt, T. Gemming hat die HAADF-STEM und TEM aufnahmen angefertigt, A. Seifert fertigte die Festkörper-NMR Spektren an und D. Lehmann hat die XPS Charakterisierung durchgeführt. Die erhaltenen analytischen Ergebnisse wurden vom Autor interpretiert.

3.6.1 Introduction

The incorporation of hetero atoms like boron,[258] nitrogen,[259] phosphorous[260] and sulfur[261] into carbon materials influences the carbon structure by mainly adding sp^2 defects, which changes the properties of the specific carbon compound.[262] It was shown that nitrogen-doped carbon materials possess, for example, a different electrochemical behavior then the respective original carbon species. Moreover, the stabilization of metal nanoparticles with donating nitrogen surface functionalities can be enhanced upon addition of different nitrogen sources, for example, acetonitrile.[263–266] Therefore, a vast variety of applications like CO_2 capturing,[267,268] super capacitors[269–272] or catalyst supports for polymer electrolyte membrane fuel cells[273,274] have been established. The incorporation of nitrogen in a carbon matrix can be achieved by reacting the desired carbon material at high temperatures with, *i. e.* ammonia.[275] Another approach is given by using nitrogen-rich polymers like melamine resins,[266,272] metal organic frameworks,[269,270] or bioorganic polymers like starch[276].

One possibility to prepare organic-inorganic hybrid materials is twin polymerization.[62] Therefore, the twin monomer, for example, 2,2‘-spiro-bi[4*H*-1,3,2-benzodioxasiline] (= SBS) is polymerized under acidic conditions or the polymerization is started by thermal initiation.[69,72,154] During the twin polymerization process, a strong mechanistically coupling between the formation of the organic and inorganic polymer exists, which leads to a hybrid material consisting of highly dispersed SiO_2 nanoclusters in a phenolic resin.[71] After carbonization of the twin polymer and removal of the inorganic SiO_2 phase with a boiling 5 M NaOH solution, a micro-porous carbon material is obtained, while the inorganic material is accessible as a mesoporous solid by oxidation of the previously carbonized compound in air.[63] Coating of various hard templates by twin polymerization leads to a diversity of porous carbon materials.[73,74]

The functionalization of the organic part of the twin monomer motif has a significant influence on the twin polymerization process itself.[70,182] Furthermore, doping of the resulting carbon material can also be achieved by modification of the organic moieties. This was demonstrated by using $Si(OCH_2{}^{c}C_4H_3S)_4$ as twin monomer, leading to sulphur-doped carbon materials, which are, for example, suitable as anode material for lithium ion batteries.[183] Exchanging the silicon to various main group or transition metals enables the preparation of Sn[79,80], Ge[81], W[78], Ti[76,155], Zr[221] and Hf[221] oxides. Furthermore, the use of silver(I) carboxylates such as $[AgO_2CCH_2{}^{c}C_4H_3S(PPh_3)]$ during the twin polymerization process led to highly dispersed silver nanoparticle-rich carbon or silica materials.[222]

Herein, we describe the synthesis and characterization of pyrrole-based twin monomers of type $Si(OCH_2{}^{c}C_4H_3NR)_4$ (**5**, R = Me; **6**, R = H). Their polymerization/copolymerization behavior is reported as well as their use for the generation of nitrogen-containing highly porous carbon materials.

3.6.2 Twin monomer synthesis

According to Scheme 3.6.1, aldehydes $2\text{-}H(O)C{}^{c}C_4H_3NR$ (**1**, R = Me; **2**, R = H) were reduced with sodium borohydride to give the corresponding alcohols **3**[277] or **4**[278], which upon consecutive treatment with $SiCl_4$ in a 4:1 stoichiometry in presence of NEt_3 afforded, after appropriate work-up, the title silicon orthoesters $Si(OCH_2{}^{c}C_4H_3NR)_4$ (**5**, R = Me; **6**, R = H) (Experimental Section) as solid materials in 68 % (**5**) and 44 % (**6**) yield, respectively.

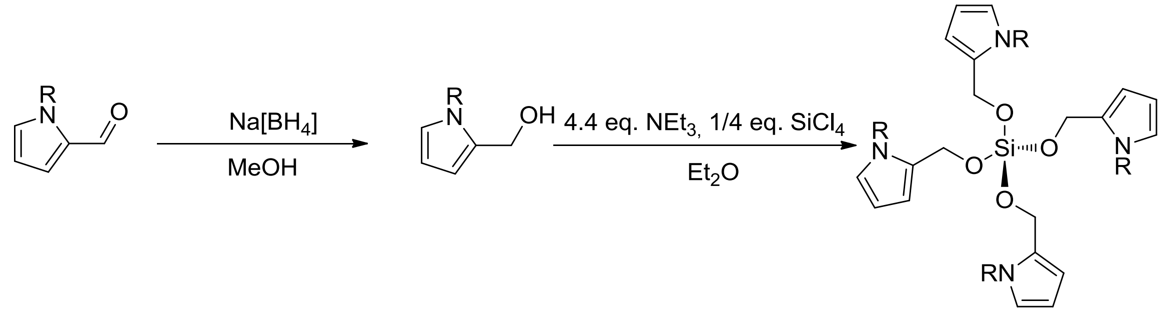

1, R = Me; **2**, R = H **3**, R = Me; **4**, R = H **5**, R = Me; **6**, R = H

Scheme 3.6.1. Consecutive synthetic methodology for the preparation of the twin monomers **5** and **6**, respectively.

The as-prepared twin monomers **5** and **6** were characterized by IR, ^{1}H, $^{13}C\{^{1}H\}$ and $^{29}Si\{^{1}H\}$ DEPT NMR spectroscopy and ESI mass-spectrometry (see ESI for detailed information). The ^{1}H NMR spectra of **5** and **6** contain the resonance signals typical for the pyrrole protons between 6.59 and 6.03 ppm, which resonate at the same chemical shift as the corresponding alcohols. Next to the aromatic protons the CH_2 hydrogens are observed as a singlet at 4.6 ppm, which is in contrast to the corresponding alcohols, where they appear as doublet due to coupling with the HO proton. This behavior allows to monitor the formation of **5** and **6** from **1** and **2**, respectively. Regarding the $^{13}C\{^{1}H\}$ NMR spectra of **5** and **6** no significant shifting is observed compared to the **3** and **4**, which is typical for the formation of silicon orthoester.[62] The silicon atoms in **5** and **6** gave a single resonance at 81.6 ppm (**5**) and 80.9 ppm (**6**) as it could be shown by ^{29}Si-DEPT-NMR spectroscopy. The obtained IR spectra of **5** and **6** are similar. Both compounds exhibit characteristic vibrations at 1100 cm^{-1} (CO) and 1000 cm^{-1} (SiO_2). The only difference is the strong stretching vibration of the NH group at 3380 cm^{-1} for **6**. High resolution mass-spectrometry proved the existence of **5** (m/z = 467.2099) and **6** (m/z = 413.1621), respectively.

The thermal behavior of **5** and **6** was determined by thermogravimetry (= TG), differential scanning calorimetry (= DSC) and mass-spectrometry-coupled TG (= TG-MS). Regarding the DSC traces of **5** an endothermic event was observed at 64 °C (-11.2 kJ/mol) which is attributed to the melting of **5**. This event is followed by a strong exothermic peak at 140 °C (82.3 kJ/mol). In comparison to **6**, two sharp exothermic peaks at 93 °C and 94 °C (48.8 kJ/mol) are found, which most probably overlay an endothermic melting process, resulting in a lower energy output as compared to **5**. This behavior is supported by heating **6** in a glass vial to 100 °C whereby a melting is observed at 93 °C, which is accompanied by a color change and immediate solidification of the molten material. The polymerization temperature of 93 °C is so far the lowest one reported for twin monomers.[279] The exothermic events were further examined by TG studies (Figure 3.6.1) showing that **5** (Δm = 23.5%) releases nearly twice as much volatiles as **6** (Δm = 10.1 %).

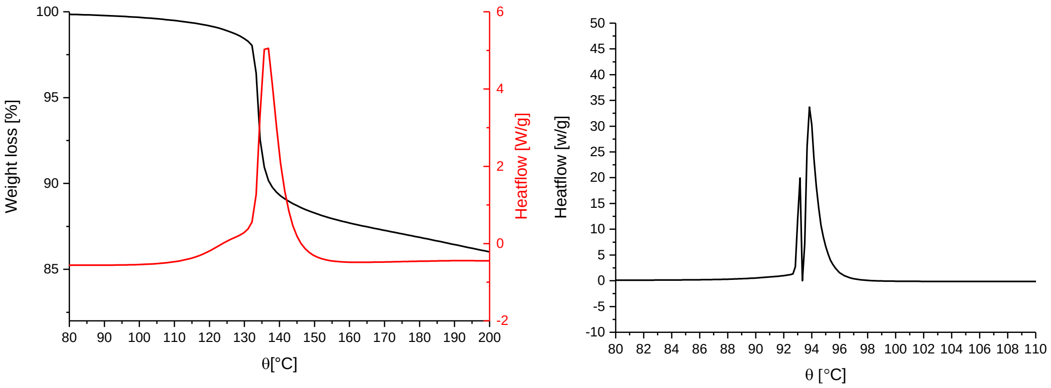

Figure 3.6.1. Left: TG (black) and DSC traces (red) (40 - 800 °C, 10 K/min, Ar) of **5**. Right: DSC peaks of **6** (see ESI for further data) (40 - 600 °C, 10 K/min, N_2).

The identity of the volatiles formed during the heating process of **5** and **6** was investigated by TG-MS experiments (Figure 3.6.2). For both compounds the same volatiles could be detected of which water is the main species, implying a condensation reaction. Also, the formation of formaldehyde could be detected, which is formed by degradation of the CH_2O building block attributed to the large amount of energy released upon the condensation reaction.

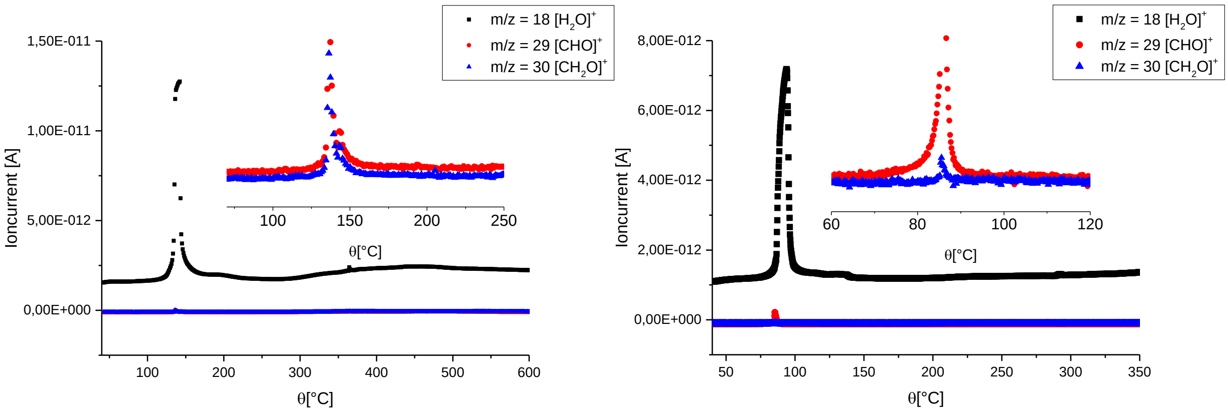

Figure 3.6.2. TG-MS traces of **5** (left) and **6** (right). The m/z values typical for formaldehyde are shown within the inset in a higher magnification (40 - 800 °C, 10 K/min, Ar).

3.6.3 Polymerization and copolymerization of 5 and 6

The thermal polymerization abilities of **5** and **6** were investigated. Since **5** exhibits a higher condensation temperature then **6**, as indicated by DSC studies, this compound was heated to 145 °C and after cooling to ambient temperature the resulting material was treated with dichloromethane, whereby only a small amount of an insoluble material remained. In contrast, polymerization of **6** was conducted in anhydrous toluene. After heating the mixture to reflux a brown solid material precipitated.

In addition, the acidic initiated twin-polymerization behavior of **5** and **6** was investigated for which the twin monomers were dissolved in anhydrous toluene and upon addition of methane sulfonic acid a solid material precipitated. The co-polymerization experiments were conducted in a similar manner under addition of two equiv. of 2,2‘-spiro-bi[4H-1,3,2-benzodioxasiline] (= SBS)[70] to **5** and **6** (see Experimental Section for detailed procedures).

The nitrogen content within the obtained hybrid materials was determined by microanalysis (Table 3.6.1). Monomer **5** afforded a hybrid material possessing a lower nitrogen content than the one obtained from **6**, while the materials prepared by acid initiated polymerization exhibit nearly the same amount of nitrogen. This most probably is attributed to the different substituents R at the nitrogen atom, which has a direct influence on the polymerization behaviour as shown by DSC experiments of monomers **5** and **6** (see above).

Table 3.6.1. Nitrogen content of the obtained hybrid materials measured by microanalysis (nitrogen content of **5** = 11.9%; nitrogen content of **6** = 13.5%) .

Twin monomer	Thermal initiation	Acidic initiation	Copolymerization
5	7.3 %	9.3 %	5.1 %
6	12.6 %	11.0 %	8.9 %

The HAADF-STEM images of the respective hybrid materials prepared under acidic (**5** and **6**) and thermal polymerization (**6**) are depicted in Figure 3.6.3. The nanostructuring is typical for twin polymers,[71] but rougher as for known systems derived from SBS.[63] Since the samples were prepared as ultra-microtomic thin cuts of 50 nm thickness, the observed grainy structure can be referred to the z contrast resulting from the heavier silicon dioxide clusters. As it can be seen from Figure 3.6.3, images A and B exhibit a homogenous distribution of the inorganic phase, while C shows some agglomeration of the silicon dioxide components.

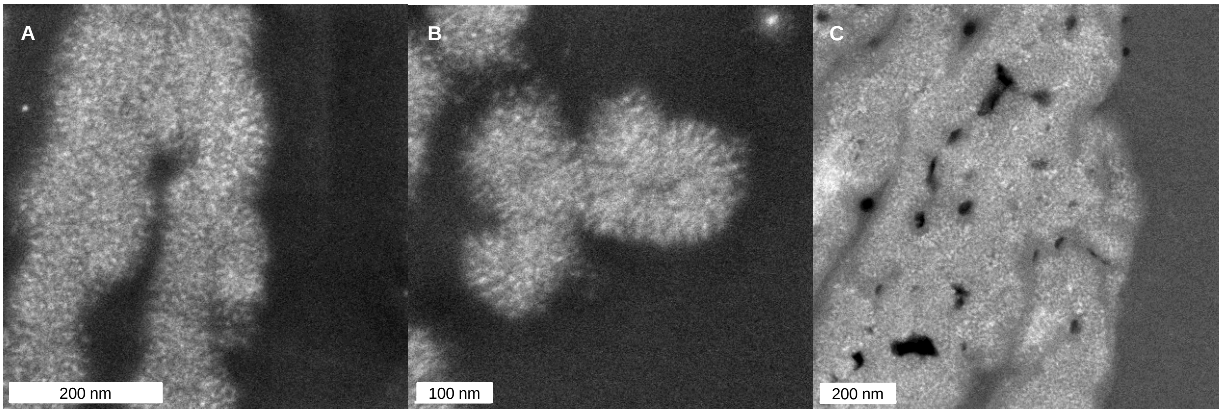

Figure 3.6.3. HAADF-STEM (= High Angle Annular Dark Field, 200 kV) imaged from the obtained hybrid material of **5** (A = acidic initiation) and **6** (B = thermal- and C = acidic initiation), respectively, after homo-polymerization.

3.6.4 Solid-state NMR analysis of the hybrid materials

In the $^{13}C\{^1H\}$-CPMAS NMR spectra of the hybrid materials obtained from **5** and **6**, all expected signals were observed (see ESI). The striking feature of the spectra is the abundance of the resonance signal at 60 ppm characteristic for the CH_2OSi moiety in the monomer. Instead a new resonance signal at 25 ppm is observed indicating the formation of a linking CH_2 group between two $^cC_4H_2NR$ (R = Me, H) fragments. The materials prepared by acidic initiation exhibit a broad resonance signal between 175 – 180 ppm which can be assigned to the respective carboxaldehyde functionality, which was formed upon oxidation of the CH_2OH group.[280–282] The ^{29}Si-CPMAS NMR spectra are characterized by mostly Q^3 signals indicating some crosslinking within the inorganic SiO_2 component (ESI).

Major differences are found in the $^{13}C\{^1H\}$-CPMAS NMR spectra between the hybrid materials obtained by acidic or thermal polymerization of **6**. For both materials the resonance signal at 25 ppm is observed referring to the 2,5-linking pattern as depicted in Figure 4.[283] In contrast to the material obtained after thermal polymerization of **6**, a new resonance signal is found at 40 ppm and we suppose that this signal originates most likely from a 1,2-linking (N-alkylation) within the polymer matrix (Figure 3.6.4).[284]

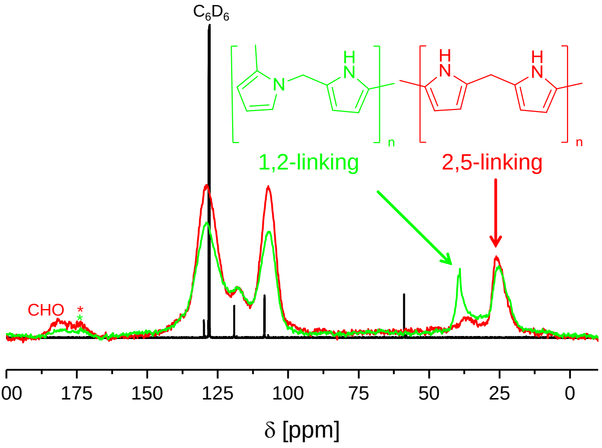

Figure 3.6.4. $^{13}C\{^1H\}$ NMR spectrum of monomer **6** (black) and $^{13}C\{^1H\}$-CP-MAS NMR spectra of the hybrid material obtained thru thermal initiation (red) and the compound prepared by adding an acidic initiator (green) (100.6 MHz, 15 kHz, referenced to tetrakistrimethylsilyl silane).

3.6.5 Nitrogen-rich porous carbon materials

The obtained hybrid materials from the homo- or co-polymerization of **5** and **6** (see earlier) were consecutively carbonized at 800 °C for 15 min under a constant flow of argon and the black materials formed were afterwards refluxed with a 5 M NaOH solution to remove the inorganic silicon dioxide network (see ESI for detailed procedure).

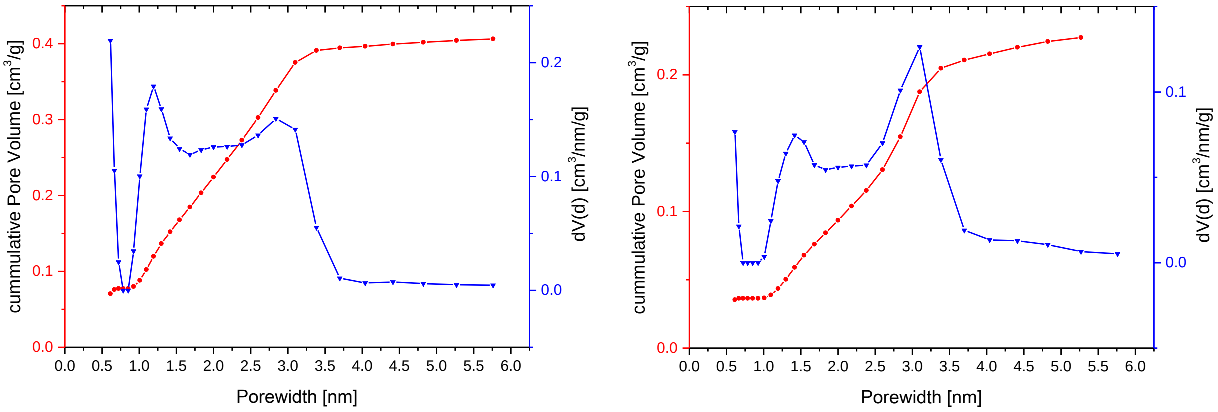

Figure 3.6.5. Pore-size distribution of the carbon materials obtained from the thermal (left) and the acidic (right) polymerization of **6** (derived from N_2 adsorption/desorption isotherms at 77 K).

The porous nature of the as-prepared carbon materials was investigated by N_2 adsorption/desorption isotherms from which the specific surface areas and pore volumes were calculated by DFT methods.[190] Mostly type IV isotherms were found according to IUPAC[139] for the porous carbon materials obtained by homopolymerization of **5** and **6**. The meso-porous character is in agreement with the porosity observed for similar twin monomers based on furan and thiophene.[62,181] In addition, however, some micro-pores are found by DFT calculations too. Considering the obtained pore diameters it can be noted that acid-initiated polymerization of **5** leads to an equal distribution of micro- (1 - 2 nm) and meso-pores (3 - 4 nm) (Figure 3.6.5). A different result was found for **6**, since the distribution of meso- and micro-pores depends on the polymerization type (acidic *vs* thermal). As shown in Figure 5, the carbon material obtained from thermally polymerized **6** led to a higher micro-porous part, while acidic initiation increased the amount of macro-pores. The calculated surface areas of the porous materials from the acid-initiated hybrid materials (**5** or **6**) are ca. 310 m^2/g, for thermally polymerized **6** a porous carbon material with a surface area of 633 m^2/g was obtained. Compared to furan-based twin monomers described in literature,[62] the calculated surface areas are significantly increased (for comparison, furan-based twin monomer 135 m^2/g) [62].

The porous nature of the carbon materials obtained by copolymerization of **5** and **6** with SBS is dominated by micro-pores, which is a consequence of the co-polymerized monomer. Mainly IUPAC type I isotherms[139] were found. Also the pore size distribution (ESI) shows mainly micro-pores next to a minor amount (due to the lower cumulated pore volumes in this area) of meso-pores. A difference is found in the calculated surface areas. The co-polymerized material obtained from SBS and **5** resulted in a porous carbon system (840 m^2/g), while the co-polymerized product of **6** with SBS gave a material with 290 m^2/g. One explanation for this finding is the high amount of inorganic residue in the carbon matrix, which could not be completely removed by treatment with sodium hydroxide (14.3 %, TG). HAADF-STEM, TEM and XPS studies confirmed the existence of silicon dioxide structures (see ESI Figures S18 and S19) within the carbon matrix. We suppose that the agglomeration of the formed silicon dioxide nanoclusters for the acid initiated twin polymerization of **6** facilitates their sintering upon carbonization and as result thereof, lower surface areas are typical.

3.6.6 Nitrogen content of the porous carbon materials and XPS studies

The nitrogen content of the as-prepared carbon materials was measured by micro-analysis (Table 3.6.2). It was found that the nitrogen contents are lower than the ones for the uncarbonized hybrid materials. It also becomes obvious that the difference in the nitrogen content between the hybrid material and the resulting porous carbon compound is little, when **5** is used for twin polymerization indicating an lower nitrogen loss during carbonization. In contrast, **6** generates nitrogen-richer hybrid materials, but during the carbonization process 2 – 4 % of the nitrogen is lost, which, however, could not further be clarified, for example, by TG-MS studies.

Table 3.6.2. Nitrogen content of the obtained porous carbon materials measured by micro-analysis. Due to the low yield of hybrid material obtained by thermal polymerization of **5**, no carbonization experiments were carried out (nitrogen content of **5** = 11.9%; nitrogen content of **6** = 13.5%).

Twin monomer	Thermal initiation	Acidic initiation	Co-polymerization
5	-	9.1 %	5.0 %
6	8.6 %	7.9 %	6.6 %

As it can be seen from Table 3.6.2, the N-Me functionalized compound **5** leads to a better incorporation of nitrogen within the carbon matrix during the carbonization process. This observation is supported by the derived porous carbon material received from the acidic-initiated twin-polymerization of **6**. It has been demonstrated that the N-H building block is partly substituted by a CH_2 group during the twin polymerization process and hence less nitrogen is evolved as from the material obtained by thermal twin-polymerization of **6**.

The electronic structure of the incorporated nitrogen was further investigated by X-ray photo-electron spectroscopic studies. The carbon materials derived from the acidic-initiated twin polymerization of **5** and the thermally-induced polymerization of **6** showed the best results regarding the surface area and the nitrogen content. The obtained XPS spectrum (Figure 3.6.6) of the latter material exhibits two bands, which can be referred to pyrrolic (ca. 398 eV) and pyridinic nitrogen (ca. 400 eV) species that means, the nitrogen atoms are either incorporated in pyrrol-like 5-ring or pyrdinic 6-ring moieties within the porous carbon matrix.[285] Since in monomers **5** and **6** pyrrole units are present the incorporation of pyrrolic nitrogen is more favored. Due to the high temperature used during carbonization some pyrrolic nitrogen groups were converted to pyridinc units as indicated by XPS.

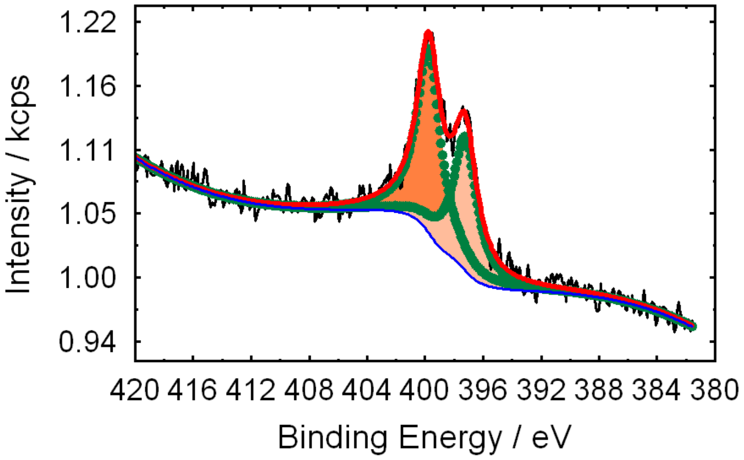

Figure 3.6.6. XPS spectrum of the carbon material obtained from **6** after thermal initiation (N1s, band pass energy = 5 eV).

3.6.7 Conclusion

Within this study a straightforward synthetic methodology for doping porous carbon materials with nitrogen by twin polymerization is reported. Therefore, the new twin monomers $Si(OCH_2{}^cC_4H_3NR)_4$ (**5**, R = Me; **6**, R = H) were prepared by reacting the specific alcohols $2\text{-}HOCH_2\text{-}{}^cC_4H_3NR$ (**1**, R = Me; **2**, R = H) with silicon tetrachloride in a 4:1 molar ratio in the presence of triethylamine. The as-prepared twin monomers **5** and **6** were characterized by NMR and IR spectroscopy, ESI-mass spectrometry and micro-analysis. The thermal behavior of **5** and **6** was investigated by DSC indicating an exothermic condensation reaction at 140 °C (**5**) and 93 °C (**6**), respectively, which is the lowest temperature observed for thermally induced twin-polymerization so far.[279] The gaseous reaction products at this temperature were examined by TG-MS revealing the formation of water underlining a temperature-induced condensation reaction.

The twin polymerization behavior of **5** and **6** was investigated under acidic and thermal initiation, respectively. Both twin monomers were polymerized by addition of $MeSO_3H$. The thermal polymerization of **6** gave higher yields than observed for **5**.

The obtained hybrid materials were investigated by $^{13}C\{^1H\}$-CP-MAS and $^{29}Si\{^1H\}$-CP-MAS NMR spectroscopy, revealing that the CH_2OSi moieties of the twin-monomers were transferred into a methylene group. A different substitution pattern was observed in the hybrid materials obtained by the twin polymerization of **6**. Initiating the polymerization process thermally, a 2,5-linking is observed, however, using the acidic method an additional 1,2-linking (N-alkylation) occured. The nitrogen content of the obtained hybrid materials was determined by micro-analysis revealing higher nitrogen contents in the hybrid material obtained from **6**. The same trend was observed within the copolymerization experiments of **5** and **6** with 2,2‘-spiro-bi[4H-1,3,2-benzodioxasiline] (= SBS).

Furthermore, porous nitrogen-containing carbon materials were prepared from the various hybrid materials by heating them to 800 °C under an inert atmosphere and removal of the incorporated inorganic SiO_2 network by refluxing the respective material with a 5 M NaOH solution. N_2-adsorption/desorption measurements revealed a mostly meso-porous nature for the homopolymerized materials, while co-polymerization led to micro-porous systems as characteristic for SBS.[71]

While the thermal product exhibits a higher micro-porous part, the acid-initiated material is more meso-porous. The nitrogen content of the porous carbon materials only slightly decreases during carbonization (below 1 % for the materials derived from **5**), while the system derived from **6** releases more nitrogen (2 – 4 %). The hybridization of the incorporated nitrogen was investigated by XPS. The carbon materials obtained from acidic-initiated twin polymerization of **5** and thermally polymerized **6** were examined, since those samples showed the best results regarding surface area (310 m^2/g for **5** and 633 m^2/g for **6**) as well as high nitrogen contents (9.1 % for **5** and 8.6 for **6**). Therefore, mostly pyrrolic nitrogen along with pyridinic nitrogen moieties were found within those carbon materials.

The incorporation of transition metal nanoparticles within these porous carbon structures will be studied in further work, since the donating character of the incorporated nitrogen atoms increases the stabilization of those particles as indicated by litrature[286].

3.6.8 Experimental Section

General

All reactions involving moisture sensitive compounds **5** and **6** were carried out under an atmosphere of argon using standard Schlenk techniques. Diethyl ether, toluene and *n*-hexane were dried using a M. Braun SBS-800 purification system (stationary drying with molecular sieve columns 3 Å).

Carbaldehydes **1** and **2** were purchased from commercial suppliers and used without any further purification. 2,2'-Spirobi[4*H*-1,3,2-benzodioxasiline] was prepared according to a published procedure.[63] The alcohols **3**[277] and **4**[278] were prepared following published procedures.

All thermal operations were carried out in a Carbolite Tube Furnace MTF 12/38/400. ^{1}H NMR (500.3 MHz), $^{13}C\{^{1}H\}$ NMR (125.8 MHz) and $^{29}Si\{^{1}H\}$-DEPT-NMR (99.39 MHz) spectra were recorded with a Bruker Avance III 500 spectrometer at 298 K. Chemical shifts δ are reported in ppm (parts per million) using undeuterated solvent residues as internal standard (benzene-d_6: ^{1}H, 7.16 ppm and $^{13}C\{^{1}H\}$, 128.06 ppm or chloroform-d_1: ^{1}H, 7.26 ppm and $^{13}C\{^{1}H\}$, 77.16 ppm), while for the ^{29}Si experiments $SiMe_4$ was used as internal standard. Solid state $^{13}C\{^{1}H\}$ and $^{29}Si\{^{1}H\}$ NMR measurements were conducted using cross polarization (CP) and magic angle spinning (MAS) with spinning frequencies between 12.5 and 20 kHz. Infrared spectra were recorded with a FT-IR Nicolet 200 spectrometer. SEM images and EDX analyses were performed with a Phillips NanoNovaSEM equipment. HAADF-STEM images were recorded with a Fecnai FC20 instrument with 200 kV accelerating voltage. The melting points of **5** and **6** were determined with a Gallenkamp MFB 595 010 M melting point apparatus. Microanalyses were performed with a Thermo FLASHEA 1112 Series instrument. Mass spectra were recorded with a Bruker micrOTOF QII system. Gas absorption/desorption measurements were carried out using an Autosorb IQ2 system. Thermal analyses were performed with a Mettler Toledo TGA/DSC1/1600 instrument with a MX1 scale. DSC experiments were performed with a Mettler Toledo DSC1/700 equipment. X-ray photoemission spectroscopy (XPS) was performed using a SPECS XR50 X-ray source (Mg K_α emission line of 1253.6 eV, 300 W) in combination with a SPECS PHOIBOS 150 analyzer. Charging of the samples was compensated with a SPECS FG15/40 electron flood gun (0.1 eV kinetic energy, 0.05 mA emission current).

Synthesis of tetra[(*N*-methylpyrrol)methoxy]silane (5). In a typical experiment, 5.38 g (48.4 mmol) of **3** were diluted in 20 mL of anhydrous diethyl ether and 8.23 mL (53.1 mmol) of NEt$_3$ were added. This mixture was cooled to 0 °C and 2.0 g (11.8 mmol) of silicon tetrachloride diluted in 10 mL of diethyl ether were added drop wise via a syringe. The resulting suspension was warmed to ambient temperature and stirring was continued for 30 min. Afterwards, the precipitated ammonium salt was filtered off and washed thrice with diethyl ether (each 50 mL). The filtrate was concentrated *in vacuo* and upon addition of 30 mL of *n*-hexane the title compound precipitated and was collected by filtration. After removing of all volatiles *in vacuo*, a pale yellow solid was obtained (yield: 7.56 g, 68 % based on SiCl$_4$). MP: 64 °C. Elemental analysis calculated for $C_{24}H_{32}N_4O_4Si$: C, 61.51, H, 6.88, N, 11.96; found: C, 61.22, H, 6.99, N, 11.86; IR (KBr, cm^{-1}): 3100 m [ν(CH$_{aromat}$)], 2938 m [ν_{as}(CH$_2$)] , 2876 m [ν_s(CH$_2$)], 1493 m [δ(CH$_2$)], 1085 m [ν(C-O)], 995 s [ν (Si-O)]; ^{1}H NMR (CDCl$_3$, ppm): 6.59 (pt, 1H, 5-^{c}C$_4$**H**$_3$N), 6.03 (pd, 2 H, 2- and 3-^{c}C$_4$**H**$_3$N), 4.58 (s, 2 H, C**H**$_2$), 3.59 (s, 3 H, C**H**$_3$); ^{13}C{^{1}H} NMR (CDCl$_3$, ppm): 130.71 (*ipso*-^{c}**C**$_4$H$_3$N), 123.16 (5-^{c}**C**$_4$H$_3$N), 109.19 (3-^{c}**C**$_4$H$_3$N), 106.70 (4-^{c}**C**$_4$H$_3$N), 57.34 (O**C**H$_2$), 33.85 (N**C**H$_3$); ^{29}Si{^{1}H}-DEPT NMR (CDCl$_3$, ppm): 81.6; ESI-MS: ($C_{24}H_{32}N_4O_4Si$) m/z: [M-nH]$^+$ calc. = 467.2109; found: 467.2099.

Synthesis of tetra(pyrrolmethoxy)silane (6). According to the synthesis of **5**, 4.0 g (41 mmol) of **4** and 6.9 mL (50 mmol) of NEt$_3$ were reacted with 1.7 g (10 mmol) of silicon tetrachloride. Appropriate work-up gave solid colorless **6** (yield: 1.8 g, 44 % based on SiCl$_4$). MP: 93 °C. Elemental analysis calculated for $C_{20}H_{24}N_4O_4Si$: C, 58.23, H, 5.86, N, 13.58; found : C, 58.20, H, 5.97, N, 13.46; IR (KBr, cm^{-1}): 3380 s [ν(NH)], 3130 w [ν(CH$_{aromat}$)], 2941 m [ν_{as}(CH$_2$)] , 2873 m [ν_s(CH$_2$)], 1467 m [δ(CH$_2$)], 1091 m [ν(C-O)], 1020 s [ν(Si-O)]; ^{1}H NMR (C$_6$D$_6$, ppm): 7.77 (br. s, 1H, N**H**), 6.39 (m, 1H, 5-^{c}C$_4$**H**$_3$N), 6.17 (m, 2 H, 2- and 3-^{c}C$_4$**H**$_3$N), 4.56 (s, 2 H, C**H**$_2$); ^{13}C{^{1}H} NMR (C$_6$D$_6$, ppm): 129.9 (*ipso*-^{c}**C**$_4$H$_3$N), 119.13 (5-^{c}**C**$_4$H$_3$N), 108.44 (3-^{c}**C**$_4$H$_3$N), 108.39 (4-^{c}**C**$_4$H$_3$N), 58.87 (O**C**H$_2$); ^{29}Si{^{1}H}-DEPT NMR (CDCl$_3$, ppm): 80.9; ESI-MS: ($C_{24}H_{32}N_4O_4Si$) m/z: [M-nH]$^+$ calc.= 413.1640; found: 413.1621.

Thermal-initiated twin-polymerization of 5. Into a 10 mL sample vial 1.0 g (2.1 mmol) of **5** were placed and heated in an oil bath at 150 °C for 20 min. The remaining solid was cooled to ambient temperature and was then extracted twice with dichloromethane (each 10 mL). The hybrid material was obtained as a black solid (yield: 0.3 g, 30 % based on charged **5**).

Acid-initiated twin polymerization of 5. To a refluxing solution of **5** (2.0 g, 4.2 mmol) in 50 mL of dichloromethane, $MeSO_3H$ (0.05 mL, 0.9 mmol) diluted in 0.95 mL of dichloromethane was added in a single portion. After 2 h of refluxing, the material was filtered off and washed twice with dichloromethane (each 10 mL) affording the respective hybrid material as a dark brown solid (yield: 1.27 g, 63 % based on charged **5**).

Co-polymerization of 5 with SBS. A mixture of **5** (1.7 g, 3.6 mmol) and SBS (2.0 g, 7.3 mmol) in 100 mL of dichloromethane was heated to reflux and then $MeSO_3H$ (0.1 mL, 1.8 mmol) diluted in 0.9 mL of dichloromethane was added in a single portion. After 12 h of stirring at 40 °C the hybrid material was filtered off and washed twice with dichloromethane (each 20 mL) giving the corresponding material as a red-brown solid (yield: 2.8 g, 76 % based on charged **5** and SBS).

Thermal-initiated twin polymerization of 6. Twin-monomer **6** (1.5 g, 3.6 mmol) was dissolved in 50 mL of anhydrous toluene and the solution was refluxed for 12 h. The remaining suspension was cooled to ambient temperature and the precipitating hybrid material was obtained as a brown solid after filtration (yield: 0.9 g, 62 % based on charged **6**).

Acid-initiated twin polymerization of 6. This reaction was performed as described for **5**, but using toluene instead of dichloromethane (yield: 1.9 g, 95 % based on charged **6**).

Copolymerization of 6 with SBS. This reaction was performed as described for **5**, but using toluene instead of dichloromethane (Yield: 2 g, 57 % based on the used amount of **6** and SBS).

Acknowledgement. We are grateful to the Deutsche Forschungsgemeinschaft (FOR 1497 Organic-Inorganic Nanocomposites by Twin Polymerization) and the

Cluster of Excellence MERGE (DFG EXC 1075, MERGE Technologies for Multifunctional Lightweight Structures) for generous financial support. We like to thank T. Jagemann and Prof. Dr. M. Hietschold for SEM imaging of different samples and B. Kempe and Dr. R. Buschbeck for mass-spectrometry measurements.

4 Zusammenfassung

Die vorliegende Dissertation hat sich mit der Inkorporation von Metallnanopartikeln während der Zwillingspolymerisation befasst, um Metallnanopartikel beladene poröse Materialien darzustellen. Dazu wurden verschiedene Lösungsansätze beleuchtet, mit denen der Eintrag von Silber- aber auch Eisenoxid-Nanopartikeln gelang. Ebenso wurden neben neuen Hf- und Zr-haltigen Zwillingsmonomeren auch Pyrrol-basierte Monomere synthetisiert und in ihrem Polymerisationsverhalten charakterisiert. Es konnten ebenfalls mit Silber- und Goldnanopartikeln gefüllte Kohlenstoffhohlkugeln mittels Zwillingspolymerisation dargestellt werden und deren katalytische Aktivität wurde anhand von zwei Modellreaktionen demonstriert. Die erhaltenen Ergebnisse sind in den einzelnen Kapiteln vorgestellt und werden nachfolgend entsprechend diskutiert.

- **3.1 A convenient light initiated synthesis of silver and gold nanoparticles using a single source precursor**

- **3.2 Twin Polymerization: A Unique and Efficient Tool for Supporting Silver Nanoparticles on Highly Porous Carbon and Silica**

- **3.3 Zirconium and Hafnium Twin Monomers for Mixed Oxides**

- **3.4 Metal Nanoparticle-loaded Porous Carbon Hollow Spheres by Twin Polymerization**

- **3.5 $Si(OCH_2Fc)_4$: Synthesis, Electrochemical Behavior and Twin Polymerization**

- **3.6 Nitrogen-containing Porous Carbon Materials by Twin Polymerization**

Kapitel 3.1

In diesem Kapitel wurde die Synthese und das photochemische Zersetzungverhalten von Triphenylphosphan stabilisierten Silber(I)- sowie Gold(I)-cinnamaten beschrieben. Dabei zeigte sich, dass durch Bestrahlung mit UV-Licht (2 x 8W, λ = 254 und 366 nm) ein Abbau der entsprechenden Carboxylate beobachtet wurde. Die gebildeten Nanopartikel wurden durch ihre charakteristische Plasmonenbande und TEM bestimmt. Die aus den TEM-Aufnahmen abgeleiteten Größenverteilungen sind für das entsprechende Triphenylphosphan stabilisierte Silber(I)-cinnamat breit, wobei hauptsächlich Partikel im Bereich von 10 ± 5 nm zu finden sind. Eine mögliche Ursache dafür sind photochemisch induzierte Reifungsprozesse, die aufgrund des UV-Lichtes ein Wachstum der Nanopartikel untereinander begünstigt.[118] Ein anderes Ergebnis wurde für das homologe Gold(I)-cinnamat erhalten. Die abgeleitete Größenverteilung zeigt das über 85 % der gebildeten Partikel kleiner als 5 nm sind.

Kapitel 3.2

Gegenstand in diesem Kapitel war die Inkorporation von Silbernanopartikeln in ein Hybridmaterial während der Zwillingspolymerisation. Dazu wurde *O*-(2-Thiophenacetatotriphenylphosphin)-Silber(I) dargestellt und mit 2,2‘-Spirobi[*4H*-1,2,2-benzodioxasilin] in einer säurekatalysierten Zwillingspolymerisation umgesetzt. Die daraus resultierenden Hybridmaterialien unterscheiden sich makroskopisch nicht von vergleichbaren Zwillingspolymeren. Mit Hilfe von HAADF-STEM konnten nur vereinzelt Silbernanopartikel detektiert werden. Dennoch konnte das eingebrachte Silber mittels EDX als homogen verteilt im Zwillingsmonomer nachgewiesen werden. Dabei konnte das Wachstum der entsprechenden Silbernanopartikel, während der Karbonisierung, mittels temperaturabhängiger XRPD beobachtet werden. Poröse Kohlenstoffmaterialien wurden nach Karbonisierung und dem Herauslösen der anorganischen Komponente mittels 5 M NaOH Lösung erhalten. Die so zugänglichen Kohlenstoffe weisen eine spezifische Oberfläche von 1034 m^2/g auf und sind mikroporös. Der Silbergehalt beträgt in diesen Proben 4 % (EDX) und die entsprechenden Nanopartikel ließen sich mittels XRPD und auf HAADF-STEM Abbildungen nachweisen. Analog zu den erhaltenen Kohlenstoffmaterialien konnte durch Oxidation der entsprechenden karbonisierten Hybridmaterialien die anorganische SiO_2-Phase isoliert werden. Diese verfügt über eine spezifische Oberfläche von 666 m^2/g und ist mesoporös. Dabei wurden auch hier Nanopartikel mittels XRPD und HAADF-STEM Analysen nachgewiesen, sowie ein Silbergehalt von 9 % (EDX) ermittelt.

Kapitel 3.3

Um das Polymerisationsverhalten von Zr- und Hf-Zwillingsmonomeren zu verstehen wurden analog des TFOS und des SBS entsprechende Zr- und Hf-haltige Zwillingsmonomere dargestellt. Es zeigte sich, dass aufgrund der freien fünften und sechsten Koordinationstelle am Zirconium bzw. Hafnium noch zusätzliche Moleküle Furfurylalkohl bzw. Salicylalkohol angelagert sind. Dieser Umstand wirkt sich jedoch nicht negativ auf das Polymerisationsverhalten aus. So konnten die TFOS und SBS analogen Zr- und Hf-Zwillingsmonomere unter Zusatz von Trifluormethansulfonsäureanhydrid polymerisiert werden. Im Fall der analogen TFOS-Verbindungen konnten mittels GC-MS Untersuchungen charakteristische Nebenprodukte, welche typisch für die Polymerisation von Furfurylalkohol sind, gefunden werden. Die erhaltenen Hybridmaterialien wurden dann mittels Festkörper-NMR-Spektroskopie untersucht. Dabei zeigte sich, dass das Hafnium-haltige SBS-Analogon nicht vollständig polymerisiert werden konnte, während bei allen anderen Verbindungen die Resonazsignale für die M-O-CH_2-Funktion (~ 60 ppm) im Hybridmaterial nicht mehr zu finden. Ein ähnliches Bild zeigt sich in den HAADF-STEM-Abbildungen. Während für alle Verbindungen eine Zwillingspolymer-typische Nanostrukturierung beobachtet wird, kommt es in dem Hybridmaterial des Hafnium-haltigen SBS-Analogons zu einer starken Phasenseparation zwischen organischer und anorganischer Phase. Aus den entsprechenden Hybridmaterialien ist poröses ZrO_2 und HfO_2 mit spezifischen Oberflächen von maximal 100 m^2/g zugänglich.

Zusätzlich zum reinen Zwillingspolymerisationsverhalten wurde auch die Copolymerisation mit SBS untersucht. Dabei konnten aus den entsprechenden Hybridmaterialien Hf- bzw. Zr-haltige poröse Siliziumdioxide mit spezifischen Oberflächen von 684 m^2/g (Zr) bzw. 550 m^2/g (Hf) erhalten werden. Ein anschließendes Sintern bei 1000 °C ließ die zuvor amorphen ZrO_2- und HfO_2-Partikel kristallisieren. Dabei wurden für das Zr-haltige Material Kristallitgrößen von 12 ± 1 nm gefunden, während eine Größenbestimmung im Hafnium-haltigen Material nicht möglich war.

Kapitel 3.4

Gegenstand in diesem Kapitel war die Darstellung poröser Kohlenstoffhohlkugeln gefüllt mit Silber und Goldnanopartikeln. Dafür wurden zunächst die benötigten Harttemplate (Aerosil® AS90, d ~ 20 nm; Aerosil® OX50, d ~ 40 nm; Stöberpartikel, d ~ 200 nm) mit $[AgO_2C(CH_2OCH_2)_3H]$ und $[(PPh_3)AuO_2C(CH_2OCH_2)_3H]$ beschichtet und anschließend thermisch zersetzt. Das Wachstum von entsprechenden Metallnanopartikeln auf der Oberfläche konnte mittels UV-Vis-Spektroskopie, XRPD und TEM nachgewiesen werden. Die so modifizierten Template wurden dann mit $MeSO_3H$ funktionalisiert und dann unter Zugabe von SBS[73] mit einer Hülle aus Zwillingspolymer umgeben. Nach Karbonisierung und dem Herauslösen der anorganischen SiO_2-Phase wurden die gewünschten Hohlkugeln erhalten. Es zeigte sich, dass der Durchmesser des eingesetzten Harttemplates einen starken Einfluss auf die erfolgreiche Verkapselung der Metallnanopartikel hat. So wurden beim kleinsten Templat (AS90) die Nanopartikel in den Kavitäten zwischen den einzelnen Kohlenstoffhohlkugeln gefunden, während bei den beiden größeren Templaten eine vollständige Verkapslung zu beobachten ist. Die Erreichbarkeit der eingebrachten Nanopartikel wurde durch die katalytische Reduktion von Methylenblau (Ag-Nanopartikel) sowie die Reduktion von 4-Nitrophenol (Au) untersucht. Es konnte so gezeigt werden, dass ein Stofftransport durch die Kapselschale stattfindet.

Kapitel 3.5

Im Mittelpunkt von diesem Kapitel stand die Zwillingspolymerisation von einem Ferrocen-haltigen Zwillingsmonomer. Dieses konnte durch Umsetzung von $SiCl_4$ und Ferrocenylmethanol in Gegenwart von Pyridin dargestellt werden. Neben der Charakterisierung mittels NMR, IR, Elementaranalyse und ESI-MS wurden auch die elektrochemischen Eigenschaften untersucht. Dabei wurden vier voneinander getrennte reversible Ein-Elektronen-Redox-Prozesse beobachtet. Um weitere Einblicke in die elektronischen Eigenschaften zu bekommen, wurden spektroelektrochemische UV-Vis/NIR-Experimente durchgeführt. Aufgrund einer fehlenden IVCT-Bande konnte gezeigt werden, dass die zuvor beobachtete Redoxseparation nicht auf einen Elektronentransfer zwischen Ferrocen bzw. Ferrocenium zurückzuführen ist, sondern durch elektrostatische Abstoßung hervorgerufen wird. Das thermische Verhalten wurde zunächst mittels DSC untersucht. Dabei zeigte sich, dass bei 210 °C eine exotherme Reaktion stattfindet. Mit Hilfe der TG-MS konnte für diesen Prozess die Freisetzung von Wasser beobachtet werden. Daraus lässt sich schlussfolgern, dass eine Kondensationsreaktion thermisch initiiert wird. Um eine Zwillingspolymerisation zu bestätigen, wurde das entsprechende Tetraferocenylmethoxysilan thermisch umgesetzt und der erhaltene unlösliche Feststoff mittels Festkörper-NMR-Spektroskopie untersucht. Es wurde kein Resonanzsignal für eine CH_2OSi-Gruppe beobachtet. Auch HAADF-STEM-Aufnahmen zeigen die für ein Zwillingspolymer typische Nanostrukturierung. Jedoch ist diese nicht so stark ausgeprägt wie für z. B. Zwillingspolymere dargestellt aus SBS, was auf den geringen Anteil an Si zurückzuführen ist. Durch Copolymerisation mit SBS konnte dieser Nachteil ausgeglichen werden und es wurde ein entsprechendes Hybridmaterial synthetisiert aus dem nach Karbonisierung und Herauslösen des SiO_2 ein mikroporöser Kohlenstoff (858 m^2/g) bzw. durch Oxidation mesoporöses Siliziumdioxid (555 m^2/g) erhalten wurde. Mittels HAADF-STEM- und TEM-Abbildungen sowie EDX konnten nanoskaliges Eisen-haltige Strukturen nachgewiesen werden und mittels der Mößbauerspektroskopie, diese als ein Gemisch aus Fe_2O_3 sowie Fe_3C (Kohlenstoff) bzw. Fe_2O_3 (SiO_2) identifiziert werden. Ebenso konnte durch magnetische Messungen gezeigt werden, dass der erhalten Kohlenstoff ein paramagnetisches Verhalten aufweist während die Siliziumdioxidkomponente superparamagentisch ist.

Ebenfalls wurden entsprechende Hohlkugeln analog den Verfahren aus Kapitel 3.4 dargestellt, die über ähnliche magnetische Eigenschaften verfügen wie das entsprechende Bulkmaterial.

Kapitel 3.6

Die Synthese von Stickstoff-haltigen porösen Kohlenstoffen mittels Zwillingspolymerisation stand hier im Mittelpunkt. Dazu wurden zwei neue Zwillingsmonomere auf der Basis von Pyrrol sowie N-Methylpyrrol dargestellt. Das thermische Verhalten dieser Verbindungen wurde mittels DSC untersucht. Dabei zeigte sich eine exotherme Reaktion bei 140 °C (N-Me) bzw. 93 °C (N-H). Auch hier konnten mittels TG-MS-Untersuchungen Kondensationsreaktionen bestätigt werden. Die thermische Zwillingspolymerisation konnte danach für beide Verbindungen in einem Experiment nachvollzogen werden, wobei sich Tetra(*N*-mehtylpyrrol)methoxysilan nur mit schlechten Ausbeuten umsetzen ließ. Eine Säure-induzierte Polymerisation sowie Copolymerisation mit SBS waren uneingeschränkt möglich. Die so zugänglichen Hybridmaterialien zeigten im Festkörper-NMR einen vollständigen Umsatz der CH_2-SiO-Funktionalität. Auch in den angefertigten HAADF-STEM-Abbildungen wird die typische Nanostrukturierung beobachtet, wobei eine Agglomeration der SiO_2-Cluster im kationisch polymerisierten Tetrapyrrolmethoxysilan zu verzeichnen ist. Aus diesen Hybridmaterialien konnten dann durch Karbonisierung sowie dem Herauslösen der SiO_2-Phase poröse Kohlenstoffe dargestellt werden. Dabei reichen die erzielbaren Oberflächen von 310-633 m^2/g für die Kohlenstoffmaterialien erhalten durch Homopolymerisation. Wird hingegen Tetra(N-Mehtylpyrrol)methoxysilan mit SBS copolymerisiert, so können spezifische Oberflächen mit bis zu 840 m^2/g dargestellt werden. Auch der Stickstoffgehalt ist vom Monomer abhängig, so wurden stets geringere N-Gehalte gefunden wenn Tetrapyrrolmethoxysilan verwendet wurde (8.6–6.6 %), wobei die Verwendung der Methylspezies bis zu 9.1–5.0 % Stickstoff erzeugte.

5 Ausblick

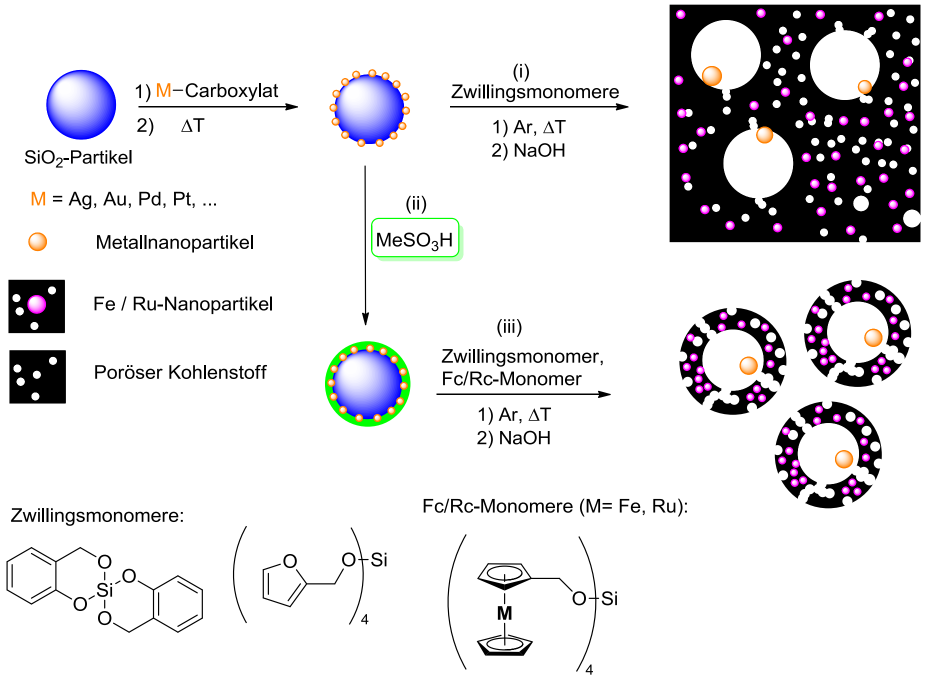

Abbildung 5.1. Hierarchische Materialien durch Zwillingspolymerisation von Metallocenmonomeren und mit Metallnanopartikel beladenen Templaten.

Die in dieser Arbeit enthaltenen Ergebnisse legen den Grundstein für weiterführende Arbeiten. So wurde gezeigt, dass sich Nanopartikel innerhalb der erzeugten Kohlenstoff- bzw. SiO_2-Materialien ausgezeichnet stabilisieren lassen. In weiterführenden Arbeiten soll nun ein universeller Ansatz erarbeitet werden, mit dem Zwillingsmonomere mit entsprechenden Ligandensystemen modifiziert werden können. Somit können weitere Übergangsmetalle für die Zwillingspolymerisation zugänglich gemacht werden. Dabei sollen auch die Ergebnisse aus Kapitel 3.6 einfließen um somit die Stabilisation der gebildeten Nanopartikel in der Kohlenstoffmatrix, zum Beispiel durch zusätzliche *N*-Donoratome, zu erhöhen. Durch Übertragen der erhaltenen Ergebnisse aus Kapitel 3.5 auf andere Metallocene, wie zum Beispiel Ruthenocen, soll ein alternativer Zugang zu neuen Zwillingspolymeren ermöglicht werden. Besonders interessant gestaltet sich dabei die Darstellung von hierarchischen Strukturen. Dabei können die in Kapitel 3.4 verwendeten Template, beladenen mit Metallnanopartikeln, in einer Bulkpolymerisation mit Zwillingsmonomeren und Metallocen-Zwillingsmonomeren eingesetzt werden um bimetallische meso- und mikroporösen

Systeme zu erzeugen. Zum anderen können gezielt die Kohlenstoffhüllen der in Kapitel 3.4 vorgestellten Hohlkugeln mit weiteren Metallen mittels Zwillingspolymerisation funktionalisiert werden. Auch soll die Katalyse in weiterführenden Arbeiten einen größeren Schwerpunkt bilden. Durch Inkorporation von Pd- oder Pt-haltigen Zwillingsmonomeren sollen entsprechende poröse Kohlenstoff- bzw. SiO_2-geträgerte Katalysatoren dargestellt werden, mit deren Hilfe C,C-Kreuzkupplungsreaktionen ermöglicht werden sollen.

6 Danksagung

Als ich im September 2006 nach Chemnitz zog und dort Chemie studieren wollte, war der Wunsch zu promovieren stets da, aber die Erfüllung noch so fern. Nun 9 Jahre später stehe ich kurz vor Ende diese Strebens, dass ich aber allein und ohne den Zuspruch vieler Freunde, Bekannten und Kollegen nie hätte schaffen können.

Deshalb möchte ich an dieser Stelle all denjenigen Danken die zum Entstehen dieser Arbeit direkt oder indirekt beigetragen haben.

Ganz besonderer Dank gilt Prof. Dr. Heinrich Lang für die Vergabe eines außergewöhnlich, abwechslungsreichen und spannenden Themas, sowie für den gewährten Freiraum und die stets konstruktive Kritik bei der Bearbeitung. Darüber hinaus danke ich Prof. Dr. Stefan Spange für das Anfertigen des Zweitgutachtens.

In den modernen Materialwissenschaften kommt es nicht nur auf die Synthese neuer Verbindungen an, sondern es bedarf auch ein großes Repertoire an analytischen Verfahren. Deshalb bedanke ich mich zum Einem ganz herzlich bei Helmut Gnägi von der Diatome AG, der mir stets bei der Ultramikrotom-Präparation half und zum Anderen bei Dr. Thomas Gemming der die HAADF-STEM und TEM Analytik durchgeführt hat. Ebenso möchte ich mich bei Prof. Dr. Michael Hietschold, Dr. Steffen Schulze und Torsten Jagemann für durchgeführte REM und EDX Analysen bedanken. Prof. Dr. Michael Mehring, Dr. Maik Schlesinger und Lutz Mertens danke ich für das Anfertigen einer Vielzahl von PXRD-Analysen. Ebenso möchte ich Dr. Tobias Rüffer und Marcus Korb für das Anfertigen von Röntgeneinkristallstrukturanalysen danken. Dr. Dieter Schaarschmidt danke ich für seine Hilfsbereitschaft bei Einkristallstrukturanalysen und auch für Diskussionen über chemische und nicht chemierelevante Themen. Für das Anfertigen von Elementaranalysen danke ich Janine Fritzsch, Ute Stöß und Katrin Müller. Darüber hinaus danke ich Dr. Roy Buschbeck und Brigitte Kempe für das Anfertigen der Massenspektren. Für die Durchführung von thermischen Analysen und deren ausgiebigen Diskussion danke ich Dr. Colin Georig, Julian Noll sowie Natalia Rüffer.

Insbesondere möchte ich mich bei Dr. Alexander Jakob und Dr. Alexander Hildebrandt für die stete Diskussionsbereitschaft sowie das Korrekturlesen dieser Arbeit bedanken. Auch danke ich meinem Laborkollegen Jürgen Matthäus Speck für die vielen Diskussion und Ausführungen zur waidgerechten Jagd sowie Tobias Graske, der mir als HiWi tatkräftig im Labor geholfen hat. Ebenso möchte ich meinen Kommilitonen Christian Gäbler und Dominique Miesel, sowie den restlichen und ehemaligen

Mitgliedern der Arbeitsgruppe für Anorganische Chemie für ein nettes und entspanntes Arbeitsklima danken.

Meiner Freundin Ulrike, sowie meiner Familie möchte ich für die tatkräftige Unterstützung sowie für den Rückhalt während der Promotionszeit danken. Auch danke ich meinen Freunden: Andreas Laue für die vielen Stunden gemeinsames Bouldern, auch Markus Nentwig, Christian Böhm und Sebastian Thiele für schöne Wander- und Kletterausflüge, aber auch für den Zeitvertreib in der digitalen Welt.

Zum Schluss möchte ich noch allen nicht explizit genannten Personen die zu dieser Arbeit einen Beitrag geleistet haben, meinen Dank aussprechen.

7 Literaturverzeichnis

(1) Plastics Europe; Statista. *Plastics – the Facts 2014/2015*; 2015.

(2) Staudinger, H. *Berichte der Dtsch. Chem. Gesellschaft* **1920**, *53*, 1073–1085.

(3) Schürmann, H. *Konstruieren mit Faser-Kunststoff-Verbunden*; 2., bearb.; Springer: Berlin, Heidelberg, 2007.

(4) Judeinstein, P.; Sanchez, C. *J. Mater. Chem.* **1996**, *6*, 511–525.

(5) Novak, B. M. *Adv Mater.* **1993**, *5*, 422–433.

(6) Soler-Illia, G. J. A. A.; Azzaroni, O. *Chem. Soc. Rev.* **2011**, *40*, 1107–1150.

(7) Carn, F.; Colin, A.; Achard, M.-F.; Deleuze, H.; Sellier, E.; Birot, M.; Backov, R. *J. Mater. Chem.* **2004**, *14*, 1370–1376.

(8) Sanchez, C.; Julián, B.; Belleville, P.; Popall, M. *J. Mater. Chem.* **2005**, *15*, 3559–3592.

(9) Gomez-Romero, P. *Adv. Mater.* **2001**, *13*, 163–174.

(10) Hu, L.-C.; Shea, K. J. *Chem. Soc. Rev.* **2011**, *40*, 688–695.

(11) Cheetham, A. K.; Rao, C. N. R.; Feller, R. K. *Chem. Commun.* **2006**, 4780–4795.

(12) Pavlidou, S.; Papaspyrides, C. D. *Prog. Polym. Sci.* **2008**, *33*, 1119–1198.

(13) Krishnamoorti, R.; A., V. R.; Giannelis, E. P. *Chem. Mater.* **1996**, 1728–1734.

(14) Giannees, B. E. P. *Adv. Mater.* **1996**, *8*, 29–35.

(15) Sinha Ray, S.; Okamoto, M. *Prog. Polym. Sci.* **2003**, *28*, 1539–1641.

(16) Alexandre, M.; Dubois, P. *Mater. Sci. Eng. R Reports* **2000**, *28*, 1–63.

(17) Lebaron, P. C.; Wang, Z.; Pinnavaia, T. J. *Appl. Clay Sci.* **1999**, *15*, 11–29.

(18) Kawasumi, M.; Hasegawa, N.; Kato, M.; Usuki, A.; Okada, A. *Macromolecules* **1997**, *30*, 6333–6338.

(19) Vaia, R. A.; Ishii, H.; Giannelis, E. P. *Chem. Mater.* **1993**, *5*, 1694–1696.

(20) Usuki, A.; Kojima, Y.; Kawasumi, M.; Okada, A.; Fukushima, Y.; Kurauchi, T.; Kamigaito, O. *J. Mater. Res.* **1993**, *8*, 1179–1184.

(21) Messersmith, P. B.; Giannelis, E. P. *Chem. Mater.* **1994**, *6*, 1719–1725.

(22) Hench, L. L.; West, J. K. *Chem. Rev.* **1990**, *90*, 33–72.

(23) Dwivedi, R. K. Drying behaviour of alumina gels. *Journal of Materials Science Letters*, 1986, *5*, 373–376.

(24) David, I. A.; Scherer, G. W. *Chem. Mater.* **1995**, *7*, 1957–1967.

(25) Novak, B. M.; Auerbach, D.; Verrier, C. **1994**, 282–286.

(26) Jackson, C. L.; Bauer, B. J.; Nakatani, a. I.; Barnes, J. D. *Chem. Mater.* **1996**, *8*, 727–733.

(27) Habsuda, J.; Simon, G. P.; Cheng, Y. B.; Hewitt, D. G.; Diggins, D. R.; Toh, H.; Cser, F. *Polymer (Guildf).* **2002**, *43*, 4627–4638.

(28) Novak, B. M.; Ellsworth, M. W. *Mater. Sci. Eng. A* **1993**, *162*, 257–264.

(29) Ellsworth, M. W.; Novak, B. M. *J. Am. Chem. Soc.* **1991**, 2756–2758.

(30) Davies, B. M. N. and C. *Macromolecules* **1991**, 5481–5483.

(31) Grubbs, R. H.; Chang, S. *Tetrahedron* **1998**, *54*, 4413–4450.

(32) Carrado, K. a.; Xu, L.; Csencsits, R.; Muntean, J. V. *Chem. Mater.* **2001**, *13*, 3766–3773.

(33) Minet, J.; Abramson, S.; Bresson, B.; Sanchez, C.; Montouillout, V.; Lequeux, N. *Chem. Mater.* **2004**, *16*, 3955–3962.

(34) Wheeler, P. a.; Wang, J.; Baker, J.; Mathias, L. J. *Chem. Mater.* **2005**, *17*, 3012–3018.

(35) Oviatt, H. W.; Shea, K. J.; Small, J. H. *Chem. Mater.* **1993**, *5*, 943–950.

(36) Shea, K. J.; Loy, D. a.; Webster, O. *J. Am. Chem. Soc.* **1992**, *114*, 6700–6710.

(37) Corriu, R. J. P.; Moreau, J. J. E.; Thepot, P.; Wong Chi Man, M. *Chem. Mater.* **1996**, *8*, 100–106.

(38) Adam, W.; Albert, R. *Tetrahedron Lett.* **1992**, *33*, 8015–8016.

(39) Rahimian, K.; Loy, D. a.; Chen, P. P. *Chem. Mater.* **2005**, *17*, 1529–1534.

(40) Auer, E.; Freund, A.; Pietsch, J.; Tacke, T. *Appl. Catal. A Gen.* **1998**, *173*, 259–271.

(41) Paraskeva, P.; Kalderis, D.; Diamadopoulos, E. *J. Chem. Technol. Biotechnol.* **2008**, *83*, 581–592.

(42) Leofanti, G.; Padovan, M.; Tozzola, G.; Venturelli, B. *Catal. Today* **1998**, *41*, 207–219.

(43) Daud, W. M. A. W.; Houshamnd, A. H. *J. Nat. Gas Chem.* **2010**, *19*, 267–279.

(44) Mishra, V. S.; Mahajani, V. V.; Joshi, J. B. *Ind. Eng. Chem. Res.* **1995**, *34*, 2–48.

(45) Puziy, a. M.; Poddubnaya, O. I.; Martínez-Alonso, a.; Suárez-García, F.; Tascón, J. M. D. *Carbon N. Y.* **2003**, *41*, 1181–1191.

(46) Liu, H.; Zhang, J.; Zhang, C.; Bao, N.; Cheng, C. *Carbon N. Y.* **2013**, *60*, 289–291.

(47) Rambabu, N.; Rao, B. V. S. K.; Surisetty, V. R.; Das, U.; Dalai, A. K. *Ind. Crops Prod.* **2014**, in press.

(48) Raymundo-Piñero, E.; Azaïs, P.; Cacciaguerra, T.; Cazorla-Amorós, D.; Linares-Solano, a.; Béguin, F. *Carbon N. Y.* **2005**, *43*, 786–795.

(49) Nakagawa, K.; Mukai, S. R.; Tamura, K.; Tamon, H. *Chem. Eng. Res. Des.* **2007**, *85*, 1331–1337.

(50) Fang, B.; Kim, M.; Yu, J.-S. *Appl. Catal. B Environ.* **2008**, *84*, 100–105.

(51) Sun, X.; Li, Y. *Langmuir* **2005**, *21*, 6019–6024.

(52) Zhang, Y.; Xu, S.; Luo, Y.; Pan, S.; Ding, H.; Li, G. *J. Mater. Chem.* **2011**, *21*, 3664–3671.

(53) Liang, C.; Li, Z.; Dai, S. *Angew. Chem. Int. Ed.* **2008**, *47*, 3696–3717.

(54) Thomas, A.; Goettmann, F.; Antonietti, M. *Chem. Mater.* **2008**, *20*, 738–755.

(55) Xia, Y.; Yang, Z.; Mokaya, R. *Nanoscale* **2010**, *2*, 639–659.

(56) Choma, J.; Górka, J.; Jaroniec, M. *Microporous Mesoporous Mater.* **2008**, *112*, 573–579.

(57) Wickramaratne, N. P.; Perera, V. S.; Park, B. W.; Gao, M.; McGimpsey, G. W.; Huang, S. D.; Jaroniec, M. *Chem. Mater.* **2013**, *25*, 2803–2811.

(58) Balgis, R.; Ogi, T.; Arif, A. F.; Anilkumar, G. M.; Mori, T.; Okuyama, K. *Carbon N. Y.* **2015**, *84*, 281–289.

(59) Shi, Q.; Zhang, R.; Lv, Y.; Deng, Y.; Elzatahrya, A. a.; Zhao, D. *Carbon N. Y.* **2015**, *84*, 335–346.

(60) Sevilla, M.; Fuertes, A. B. *J. Colloid Interface Sci.* **2012**, *366*, 147–154.

(61) Brun, N.; Prabaharan, S. R. S.; Morcrette, M.; Sanchez, C.; Pécastaings, G.; Derré, A.; Soum, A.; Deleuze, H.; Birot, M.; Backov, R. *Adv. Funct. Mater.* **2009**, *19*, 3136–3145.

(62) Grund, S.; Kempe, P.; Baumann, G.; Seifert, A.; Spange, S. *Angew. Chem. Int. Ed.* **2007**, *46*, 628–632.

(63) Spange, S.; Kempe, P.; Seifert, A.; Auer, A. A.; Ecorchard, P.; Lang, H.; Falke, M.; Hietschold, M.; Pohlers, A.; Hoyer, W.; Cox, G.; Kockrick, E.; Kaskel, S. *Angew. Chem. Int. Ed. Engl.* **2009**, *48*, 8254–8258.

(64) Meyer, H.; Nagorsen, G. *Angew. Chem* **1979**, *91*, 587–588.

(65) Birkofer, L.; Stuhl, O. Siliciumorganische Verbindungen LXIX. 2,4-Dioxa-1,2,4,5-tetrahydro-3H-3-benzosilepine und 3,'-Spiro-bi[2,4-dioxa-1,2,4,5-tetrahydro-3H-3-benzosilepin]. *Journal of Organometallic Chemistry*, 1979, *164*, C1–C5.

(66) Wieber, M.; Schmidt, M. Silicium- und germaniumhaltige 1,3-Benzodioxane. *Journal of Organometallic Chemistry*, 1963, *1*, 93–94.

(67) Kita, Y.; Yasuda, H.; Sugiyama, Y.; Fukata, F.; Haruta, J.; Tamura, Y. O-silylated ketene acetal chemistry1; divinyloxysilane derivatives as novel and useful bifunctional protecting agents for h-acidic materials. *Tetrahedron Letters*, 1983, *24*, 1273–1276.

(68) Cragg, R. H.; Nazery, M. *J. Organomet. Chem.* **1974**.

(69) Kempe, P.; Löschner, T.; Auer, A. a.; Seifert, A.; Cox, G.; Spange, S. *Chem. - A Eur. J.* **2014**, *20*, 8040–8053.

(70) Kitschke, P.; Auer, A. A.; Löschner, T.; Seifert, A.; Spange, S.; Rüffer, T.; Lang, H.; Mehring, M. *ChemplusChem* **2014**, *79*, 1009–1023.

(71) Spange, S.; Grund, S. *Adv. Mater.* **2009**, *21*, 2111–2116.

(72) Löschner, T.; Mehner, A.; Grund, S.; Seifert, A.; Pohlers, A.; Lange, A.; Cox, G.; Hähnle, H.-J.; Spange, S. *Angew. Chem. Int. Ed.* **2012**, *51*, 3258–3261.

(73) Böttger-Hiller, F.; Kempe, P.; Cox, G.; Panchenko, A.; Janssen, N.; Petzold, A.; Thurn-Albrecht, T.; Borchardt, L.; Rose, M.; Kaskel, S.; Georgi, C.; Lang, H.; Spange, S. *Angew. Chem.* **2013**, *125*, 6204–6207.

(74) Böttger-Hiller, F.; Kempe, P.; Baumann, G.; Hietschold, M.; Schäfer, P.; Zahn, D. R. T.; Petzold, A.; Thurn-Albrecht, T.; Spange, S. *Adv. Mater. Sci. Eng.* **2013**, *2013*, 1–8.

(75) Schubert, U. *J. Mater. Chem.* **2005**, *15*, 3701–3715.

(76) Mehner, A.; Rüffer, T.; Lang, H.; Pohlers, A.; Hoyer, W.; Spange, S. *Adv. Mater.* **2008**, *20*, 4113–4117.

(77) Mehner, A.; Rüffer, T.; Lang, H.; Schlesinger, M.; Mehring, M.; Spange, S. *New J. Chem.* **2013**, *37*, 1290–1293.

(78) Böttger-Hiller, F.; Lungwitz, R.; Seifert, A.; Hietschold, M.; Schlesinger, M.; Mehring, M.; Spange, S. *Angew. Chem. Int. Ed. Engl.* **2009**, *48*, 8878–8881.

(79) Leonhardt, C.; Brumm, S.; Seifert, A.; Cox, G.; Lange, A.; Rüffer, T.; Schaarschmidt, D.; Lang, H.; Jöhrmann, N.; Hietschold, M.; Simon, F.; Mehring, M. *ChemplusChem* **2013**, *78*, 1400–1412.

(80) Leonhardt, C.; Brumm, S.; Seifert, A.; Lange, A.; Csihony, S.; Mehring, M. *ChemplusChem* **2014**, *79*, 1440–1447.

(81) Kitschke, P.; Auer, A. A.; Seifert, A.; Rüffer, T.; Lang, H.; Mehring, M. *Inorg. Chim. Acta* **2014**, *409*, 472–478.

(82) Kitschke, P.; Schulze, S.; Hietschold, M.; Mehring, M. *Main Group Met. Chem.* **2013**, *36*, 1–6.

(83) Wright, J. R.; Bolt, R. O.; Goldschmidt, a.; Abbott, a. D. *J. Am. Chem. Soc.* **1958**, *80*, 1733–1737.

(84) Gerrard, W.; Kilburn, K. D. *J. Chem. Soc.* **1956**, 1536–1539.

(85) Amyes, T.; Richard, J. *J. Am.* **1992**, *114*, 8032–8041.

(86) Allcock, H. R.; Nugent, T. a.; Smeltz, L. a. *Synth. React. Inorg. Met. Org. Chem.* **1972**, *2*, 97–104.

(87) Abbott, a. D.; Wright, J. R.; Goldschmidt, A.; Stewart, W. T.; Bolt, R. O. *J. Chem. Eng. Data* **1961**, *6*, 437–442.

(88) Curran, M. D.; Gedris, T. E.; Stiegman, a. E. *Chem. Mater.* **1998**, *10*, 1604–1612.

(89) Kingston, J. V.; Vargheese, B.; Rao, M. N. S. *Main Gr. Chem.* **2000**, *3*, 79–90.

(90) Corriu, R. J. P. *J. Organomet. Chem.* **1990**, *400*, 81–106.

(91) Bradley, D. C.; Wardlaw, W. *J. Chem. Soc.* **1951**, 280–285.

(92) Bradley, C. *J. Orgmet. Chem.* **1982**, *239*, 17–22.

(93) Boyle, T. J.; Rodriguez, M. a.; Alam, T. M. *Dalt. Trans.* **2003**, *4*, 4598.

(94) Boyle, T. J.; Tribby, L. J.; Alam, T. M.; Bunge, S. D.; Holland, G. P. *Polyhedron* **2005**, *24*, 1143–1152.

(95) Baumann, S. O.; Puchberger, M.; Schubert, U. *Dalton Trans.* **2011**, *40*, 1401–1406.

(96) Schierhorn, E.; Brzezinka, K. *Fuel Energy Abstr.* **2000**, *41*, 283.

(97) Trimmel, G.; Gross, S.; Kickelbick, G.; Schubert, U. *Appl. Organomet. Chem.* **2001**, *15*, 401–406.

(98) Link, S.; Beeby, A.; Fitzgerald, S.; Schaaff, T. G.; Whetten, R. L.; El-sayed, M. a. *Luminescence* **2002**, 3410–3415.

(99) L. Feldheim, D.; D. Keating, C. *Chem. Soc. Rev.* **1998**, *27*, 1.

(100) Haruta, M.; Daté, M. *Appl. Catal. A Gen.* **2001**, *222*, 427–437.

(101) Zhang, H.-X.; Wang, H.; Re, Y.-S.; Cai, W.-B. *Chem. Commun.* **2012**, *48*, 8362.

(102) Wilcoxon, J. P.; Abrams, B. L. *Chem. Soc. Rev.* **2006**, *35*, 1162–1194.

(103) Aherne, D.; Ledwith, D. M.; Gara, M.; Kelly, J. M. *Adv. Funct. Mater.* **2008**, *18*, 2005–2016.

(104) Sharma, V. K.; Yngard, R. a.; Lin, Y. *Adv. Colloid Interface Sci.* **2009**, *145*, 83–96.

(105) Fujita, S. *Organic Chemistry of Photography*; Springer, 2004.

(106) Hartlieb, K. J.; Martin, A. D.; Saunders, M.; Raston, C. L. *New J. Chem.* **2010**, *34*, 1834.

(107) Stamplecoskie, K. G.; Scaiano, J. C. *J. Am. Chem. Soc.* **2010**, *132*, 1825–1827.

(108) Sudeep, P. K.; Kamat, P. V. *Chem. Mater.* **2005**, *17*, 5404–5410.

(109) Vollmer, C.; Schröder, M.; Thomann, Y.; Thomann, R.; Janiak, C. *Appl. Catal. A Gen.* **2012**, *425-426*, 178–183.

(110) Vollmer, C.; Janiak, C. *Coord. Chem. Rev.* **2011**, *255*, 2039–2057.

(111) Marquardt, D.; Barthel, J.; Braun, M.; Ganter, C.; Janiak, C. *CrystEngComm* **2012**, *14*, 7607–7615.

(112) Steffan, M.; Jakob, A.; Claus, P.; Lang, H. *Catal. Commun.* **2009**, *10*, 437–441.

(113) Tuchscherer, A.; Schaarschmidt, D.; Schulze, S.; Hietschold, M.; Lang, H. *Inorg. Chem. Commun.* **2011**, *14*, 676–678.

(114) Fields, E. K.; Meyerson, S. Thermal and photochemical decomposition of cis- and trans-3,5-diphenyl-1-pyrazoline. *Journal of Organic Chemistry*, 1976, *41*, 916–920.

(115) Edwards, D. A.; Mahon, M. F.; Molloy, K. C.; Ogrodnik, V. *J. Mater. Chem.* **2003**, 563–570.

(116) Taleb, a; Petit, C.; Pileni, M. *Chem. Mater.* **1997**, *9*, 950–959.

(117) Zeng, J.; Roberts, S.; Xia, Y. *Chem. - A Eur. J.* **2010**, *16*, 12559–12563.

(118) Lee, G. P.; Minett, A. I.; Innis, P. C.; Wallace, G. G. *J. Mater. Chem.* **2009**, *19*, 8294 – .

(119) Daniel, M. C.; Astruc, D. *Chem. Rev.* **2004**, *104*, 293–346.

(120) Akira Taguchi; Ferdi Schüth. *Microporous Mesoporous Mater.* **2005**, *77*, 1–45.

(121) Panella, B.; Hirscher, M.; Roth, S. *Carbon N. Y.* **2005**, *43*, 2209–2214.

(122) Sircar, S.; Golden, T. C.; Rao, M. B. *Carbon N. Y.* **1996**, *34*, 1–12.

(123) Serp, P. *Appl. Catal. A Gen.* **2003**, *253*, 337–358.

(124) Yang, Y.; Chiang, K.; Burke, N. *Catal. Today* **2011**, *178*, 197–205.

(125) Chen, D.; Qu, Z.; Shen, S.; Li, X.; Shi, Y.; Wang, Y.; Fu, Q.; Wu, J. *Catal. Today* **2011**, *175*, 338–345.

(126) Salaev, M. A.; Krejker, A. A.; Magaev, O. V.; Malkov, V. S.; Knyazev, A. S.; Borisova, E. S.; Khanaev, V. M.; Vodyankina, O. V.; Kurina, L. N. *Chem. Eng. J.* **2011**, *172*, 399–409.

(127) Chen, L.; Ma, D.; Bao, X. *J. Phys. Chem. C* **2007**, *111*, 2229–2234.

(128) Chen, L.; Ma, D.; Li, X.; Bao, X. *Catal. Letters* **2006**, *111*, 133–139.

(129) Chen, L.; Ma, D.; Pietruszka, B.; Bao, X. *J. Nat. Gas Chem.* **2006**, *15*, 181–190.

(130) Chen, Y.; Wang, C.; Liu, H.; Qiu, J.; Bao, X. *Chem. Commun.* **2005**, *2*, 5298–5300.

(131) Vinodh, R.; Sangeetha, D. *J. Mater. Sci.* **2011**, *47*, 852–859.

(132) Tapan, N. A.; Kök, A. *Chem. Eng. Commun.* **2008**, *196*, 131–147.

(133) Wang, Y.; Sheng, Z. M.; Yang, H.; Jiang, S. P.; Li, C. M. *Int. J. Hydrogen Energy* **2010**, *35*, 10087–10093.

(134) Sakintuna, B.; Yürüm, Y. *Ind. Eng. Chem. Res.* **2005**, *44*, 2893–2902.

(135) Beck, J. S.; Vartuli, J. C.; Roth, W. J.; Leonowicz, M. E.; Kresge, C. T.; Schmitt, K. D.; Chu, C. T. W.; Olson, D. H.; Sheppard, E. W. *J. Am. Chem. Soc.* **1992**, *114*, 10834–10843.

(136) Kempe, P.; Löschner, T.; Adner, D.; Spange, S. *New J. Chem.* **2011**, *35*, 2735.

(137) Jahn, S. F.; Jakob, A.; Blaudeck, T.; Schmidt, P.; Lang, H.; Baumann, R. R. *Thin Solid Films* **2010**, *518*, 3218–3222.

(138) Jahn, S. F.; Blaudeck, T.; Baumann, R. R.; Jakob, A.; Ecorchard, P.; Rüffer, T.; Lang, H.; Schmidt, P. *Chem. Mater.* **2010**, *22*, 3067–3071.

(139) Donohue, M.; Aranovich, G. *Adv. Colloid Interface Sci.* **1998**, *76-77*, 137–152.

(140) Bahamonde, A.; Mohino, F.; Rebollar, M.; Yates, M.; Avila, P.; Mendioroz, S. *Catal. Today* **2001**, *69*, 233–239.

(141) Park, S. *J. Electrochem. Soc.* **1999**, *146*, 3603–3605.

(142) Perkas, N.; Minh, D. P.; Gallezot, P.; Gedanken, A.; Besson, M. *Appl. Catal. B Environ.* **2005**, *59*, 121–130.

(143) Kapoor, M. P.; Ichihashi, Y.; Shen, W.; Matsumura, Y. *Catal. Letters* **2001**, *76*, 139–142.

(144) Gatica, J. M.; Baker, R. T.; Fornasiero, P.; Bernal, S.; Blanco, G.; Kašpar, J. *J. Phys. Chem. B* **2000**, *104*, 4667–4672.

(145) Wiemhöfer, H.-D.; Göpel, W. *Sensors Actuators B Chem.* **1991**, *4*, 365–372.

(146) Miura, N.; Raisen, T.; Lu, G.; Yamazoe, N. *Sensors Actuators B Chem.* **1998**, *47*, 84–91.

(147) Wilk, G. D.; Wallace, R. M.; Anthony, J. M. *J. Appl. Phys.* **2000**, *87*, 484–492.

(148) Wilk, G. D.; Wallace, R. M. *Appl. Phys. Lett.* **1999**, *74*, 2854–2856.

(149) Wilk, G. D.; Wallace, R. M. *Appl. Phys. Lett.* **2000**, *76*, 112–114.

(150) Parashar, V. K.; Bahl, O. P.; Unit, C. T. *J. Mater. Sci. Lett.* **1996**, *15*, 1625–1629.

(151) Monròs, G.; Martì, M. C.; Carda, J.; Tena, M. A.; Escribano, P.; Anglada, M. *J. Mater. Sci.* **1993**, *28*, 5852–5862.

(152) Zhu, H. Y.; Hao, Z. P.; Barry, J. C. *Chem. Commun.* **2002**, 2858–2859.

(153) Smith, R. C.; Ma, T.; Hoilien, N.; Tsung, L. Y.; Bevan, M. J.; Colombo, L.; Roberts, J.; Campbell, S. A.; Gladfelter, W. L. *Adv. Mater. Opt. Electron.* **2000**, *114*, 105–114.

(154) Kempe, P.; Löschner, T.; Adner, D.; Spange, S. *New J. Chem.* **2011**, *35*, 2735–2739.

(155) Mehner, A.; Pohlers, A.; Hoyer, W.; Cox, G.; Spange, S. *Macromol. Chem. Phys.* **2013**, *214*, 1000–1010.

(156) Armelao, L.; Bertagnolli, H.; Gross, S.; Krishnan, V.; Lavrencic-Stangar, U.; Müller, K.; Orel, B.; Srinivasan, G.; Tondello, E.; Zattin, A. *J. Mater. Chem.* **2005**, *15*, 1954.

(157) Fawcett, A. H.; Dadambaa, W. *Makromol. Chem.* **1982**, *2809*, 2799–2809.

(158) Gonzàlez, R.; Martìnez, R.; Ortìz, P. *Makromol. Chem., Rapid Commun.* **1992**, *523*, 517–523.

(159) Gandini, A. *Prog. Polym. Sci.* **1997**, *22*, 1203–1379.

(160) Mix, R.; Goering, H.; Schulz, G.; Gründemann, E.; Gähde, J. *J. Polym. Sci. Part A Polym. Chem.* **1995**, *33*, 1523–1536.

(161) Löschner, T.; Mehner, A.; Grund, S.; Seifert, A.; Pohlers, A.; Lange, A.; Cox, G.; Hähnle, H.-J.; Spange, S. *Angew. Chem.* **2012**, *124*, 3312–3315.

(162) Monte, F.; Larsen, W.; Mackenzie, J. D. *J. Am. Ceram. Soc.* **2004**, *83*, 628–634.

(163) Neumayer, D. a.; Cartier, E. *J. Appl. Phys.* **2001**, *90*, 1801–1808.

(164) Itoh, T. *J. Cryst. Growth* **1992**, *125*, 223–228.

(165) Withers, R. L.; Thompson, J. G.; Welberry, T. R. *Phys. Chem. Miner.* **1989**, 517–523.

(166) Tartaj, P.; Serna, C. J.; Moya, J. S.; Requena, J.; Ocana, M.; De Aza, S.; Guitian, F. *J. Mater. Sci.* **1996**, *31*, 6089–6094.

(167) Deshmukh, A. a.; Mhlanga, S. D.; Coville, N. J. *Mater. Sci. Eng. R Reports* **2010**, *70*, 1–28.

(168) Hu, J.; Chen, M.; Fang, X.; Wu, L. *Chem. Soc. Rev.* **2011**, *40*, 5472–5491.

(169) Schüth, F. *Chem. Mater.* **2014**, *26*, 423–434.

(170) Büchel, G.; Unger, K. K.; Matsumoto, A.; Tsutsumi, K. *Adv. Mater.* **1998**, *10*, 1036–1038.

(171) Yoon, S. B.; Sohn, K.; Kim, J. Y.; Shin, C.-H.; Yu, J.-S.; Hyeon, T. *Adv. Mater.* **2002**, *14*, 19–21.

(172) Valle-Vigón, P.; Sevilla, M.; Fuertes, A. B. *Chem. Mater.* **2010**, *22*, 2526–2533.

(173) Chai, G. S.; Yoon, S. B.; Kim, J. H.; Yu, J.-S. *Chem. Commun.* **2004**, *1*, 2766.

(174) Hu, F. P.; Wang, Z.; Li, Y.; Li, C.; Zhang, X.; Shen, P. K. *J. Power Sources* **2008**, *177*, 61–66.

(175) Lou, X. W.; Deng, D.; Lee, J. Y.; Archer, L. A. *Chem. Mater.* **2008**, *20*, 6562–6566.

(176) Valle-Vigón, P.; Fuertes, A. B. *RSC Adv.* **2011**, *1*, 1756.

(177) Valdessolis, T.; Vallevigon, P.; Sevilla, M.; Fuertes, A. *J. Catal.* **2007**, *251*, 239–243.

(178) Lou, X. W.; Li, C. M.; Archer, L. A. *Adv. Mater.* **2009**, *21*, 2536–2539.

(179) Zhang, W.-M.; Hu, J.-S.; Guo, Y.-G.; Zheng, S.-F.; Zhong, L.-S.; Song, W.-G.; Wan, L.-J. *Adv. Mater.* **2008**, *20*, 1160–1165.

(180) Kim, M.; Yoon, S. B.; Sohn, K.; Kim, J. Y.; Shin, C.-H.; Hyeon, T.; Yu, J.-S. *Microporous Mesoporous Mater.* **2003**, *63*, 1–9.

(181) Löschner, T.; Mehner, A.; Grund, S.; Seifert, A.; Pohlers, A.; Lange, A.; Cox, G.; Hähnle, H.-J.; Spange, S. *Angew. Chem. Int. Ed. Engl.* **2012**, *51*, 3258–3261.

(182) Böttger-Hiller, F.; Mehner, A.; Anders, S.; Kroll, L.; Cox, G.; Simon, F.; Spange, S. *Chem. Commun.* **2012**, *48*, 10568–10570.

(183) Brückner, J.; Thieme, S.; Böttger-Hiller, F.; Bauer, I.; Grossmann, H. T.; Strubel, P.; Althues, H.; Spange, S.; Kaskel, S. *Adv. Funct. Mater.* **2014**, *24*, 1284–1289.

(184) Struppert, T.; Jakob, A.; Heft, A.; Grünler, B.; Lang, H. *Thin Solid Films* **2010**, *518*, 5741–5744.

(185) Tuchscherer, A.; Schaarschmidt, D.; Schulze, S.; Hietschold, M.; Lang, H. *Dalton Trans.* **2012**, *41*, 2738–2746.

(186) Homola, J.; Yee, S. S.; Gauglitz, G. *Sensors Actuators B Chem.* **1999**, *54*, 3–15.

(187) Kelly, K. L.; Coronado, E.; Zhao, L. L.; Schatz, G. C. *J. Phys. Chem. B* **2003**, *107*, 668–677.

(188) Buffat, P.; Borel, J.-P. *Phys. Rev. A* **1976**, *13*, 2287–2298.

(189) Arcidiacono, S.; Bieri, N. .; Poulikakos, D.; Grigoropoulos, C. P. *Int. J. Multiph. Flow* **2004**, *30*, 979–994.

(190) Lastoskie, C.; Gubbins, K. E.; Quirke, N. *J. Phys. Chem.* **1993**, *97*, 4786–4796.

(191) Anderson, L.; Wittkopp, S. M.; Painter, C. J.; Liegel, J. J.; Schreiner, R.; Bell, J. A.; Shakhashiri, B. Z. *J. Chem. Educ.* **2012**, *89*, 1425–1431.

(192) Jiang, Z.-J.; Liu, C.-Y.; Sun, L.-W. *J. Phys. Chem. B* **2005**, *109*, 1730–1735.

(193) Pradhan, N.; Pal, A.; Pal, T. *Langmuir* **2001**, *17*, 1800–1802.

(194) Wunder, S.; Lu, Y.; Albrecht, M.; Ballauff, M. *ACS Catal.* **2011**, *1*, 908–916.

(195) Cui, J.; Gao, L.; Yan, S.; Zhang, W.; Li, Y.; Gao, L. *Synth. React. Inorganic, Met. Nano-Metal Chem.* **2014**, *45*, 158–163.

(196) Pozun, Z. D.; Rodenbusch, S. E.; Keller, E.; Tran, K.; Tang, W.; Stevenson, K. J.; Henkelman, G. *J. Phys. Chem. C. Nanomater. Interfaces* **2013**, *117*, 7598–7604.

(197) Abad, A.; Almela, C.; Corma, A.; García, H. *Tetrahedron* **2006**, *62*, 6666–6672.

(198) Hou, W.; Dehm, N.; Scott, R. *J. Catal.* **2008**, *253*, 22–27.

(199) Li, H.; Guan, B.; Wang, W.; Xing, D.; Fang, Z.; Wan, X.; Yang, L.; Shi, Z. *Tetrahedron* **2007**, *63*, 8430–8434.

(200) Mitsudome, T.; Noujima, A.; Mizugaki, T.; Jitsukawa, K.; Kaneda, K. *Adv. Synth. Catal.* **2009**, *351*, 1890–1896.

(201) Bolm, C.; Legros, J.; Le Paih, J.; Zani, L. *Chem. Rev.* **2004**, *104*, 6217–6254.

(202) Cao, H.; He, J.; Deng, L.; Gao, X. *Appl. Surf. Sci.* **2009**, *255*, 7974–7980.

(203) Li, Y.; Zhu, C.; Lu, T.; Guo, Z.; Zhang, D.; Ma, J.; Zhu, S. *Carbon N. Y.* **2013**, *52*, 565–573.

(204) Dong, X.; Chen, H.; Zhao, W.; Li, X.; Shi, J. *Chem. Mater.* **2007**, *19*, 3484–3490.

(205) Fuertes, A. B.; Tartaj, P. *Chem. Mater.* **2006**, *18*, 1675–1679.

(206) Hassan, M. F.; Rahman, M. M.; Guo, Z. P.; Chen, Z. X.; Liu, H. K. *Electrochim. Acta* **2010**, *55*, 5006–5013.

(207) Zhang, J.; He, D.; Su, H.; Chen, X.; Pan, M.; Mu, S. *J. Mater. Chem. A* **2014**, *2*, 1242.

(208) Zhironkina, O.; Strelkova, O.; Dianova, V. *J. Mater. Chem. B* **2014**, 4250–4261.

(209) Hu, Y.; Jensen, J. O.; Zhang, W.; Cleemann, L. N.; Xing, W.; Bjerrum, N. J.; Li, Q. *Angew. Chem. Int. Ed. Engl.* **2014**, *53*, 3675–3679.

(210) Schnitzler, M. C.; Oliveira, M. M.; Ugarte, D.; Zarbin, A. J. G. *Chem. Phys. Lett.* **2003**, *381*, 541–548.

(211) Abd-El-Aziz, A. S. *Macromol. Rapid Commun.* **2002**, *23*, 995–1031.

(212) Hudson, R. D. A. *J. Organomet. Chem.* **2001**, *637-639*, 47–69.

(213) Ni, Y.; Rulkens, R.; Manners, I. *J. Am. Chem. Soc.* **1996**, *118*, 4102–4114.

(214) Rulkens, R.; Lough, A. J.; Manners, I.; Lovelace, S. R.; Grant, C.; Geiger, W. E. *J. Am. Chem. Soc.* **1996**, *118*, 12683–12695.

(215) Manners, I. *Chem. Commun.* **1999**, 857–865.

(216) Kulbaba, K.; Manners, I. *Macromol. Rapid Commun.* **2001**, *22*, 711–724.

(217) Gómez-Elipe, P.; Resendes, R.; Macdonald, P. M.; Manners, I. *J. Am. Chem. Soc.* **1998**, *120*, 8348–8356.

(218) Rulkens, R.; Gates, D. P.; Balaishis, D.; Pudelski, J. K.; McIntosh, D. F.; Lough, A. J.; Manners, I. *J. Am. Chem. Soc.* **1997**, *119*, 10976–10986.

(219) Jäkle, F.; Rulkens, R.; Zech, G.; Foucher, D. A.; Lough, A. J.; Manners, I. *Chem. - A Eur. J.* **1998**, *4*, 2117–2128.

(220) Buretea, M. A.; Tilley, T. D. *Organometallics* **1997**, *16*, 1507–1510.

(221) Schliebe, C.; Gemming, T.; Noll, J.; Mertens, L.; Mehring, M.; Seifert, A.; Spange, S.; Lang, H. *ChemplusChem* **2014**, 1–10.

(222) Schliebe, C.; Gemming, T.; Mertens, L.; Mehring, M.; Lang, H. *Eur. J. Inorg. Chem.* **2014**, 3161–3163.

(223) Davis, W. L.; Shago, R. F.; Langner, E. H. G.; Swarts, J. C. *Polyhedron* **2005**, *24*, 1611–1616.

(224) Germaneau, R.; Chavignon, R.; Tranchier, J.; Rose-Munch, F.; Rose, E.; Collot, M.; Duhayon, C. *Organometallics* **2007**, *26*, 6139–6149.

(225) Kalita, D.; Morisue, M.; Kobuke, Y. *New J. Chem.* **2006**, *30*, 77.

(226) Günther, H. *Angew. Chem. Int. Ed.* **1972**, *11*, 861–874.

(227) Barrière, F.; Geiger, W. E. *J. Am. Chem. Soc.* **2006**, *128*, 3980–3989.

(228) LeSuer, R. J.; Buttolph, C.; Geiger, W. I. *Anal. Chem.* **2004**, *76*, 6395–6401.

(229) Hildebrandt, A.; Lang, H. *Organometallics* **2013**, *32*, 5640–5653.

(230) Gritzner, G.; Kuta, J. *Pure Appl. Chem.* **1984**, *56*, 461–466.

(231) Pfaff, U.; Filipczyk, G.; Hildebrandt, A.; Korb, M.; Lang, H. *Dalt. Trans.* **2014**, *43*, 16310–16321.

(232) Pfaff, U.; Hildebrandt, A.; Schaarschmidt, D.; Rüffer, T.; Low, P. J.; Lang, H. *Organometallics* **2013**, *32*, 6106–6117.

(233) Krejčik, M.; Daněk, M.; Hartl, F. *J. Electroanal. Chem. Interfacial Electrochem.* **1991**, *317*, 179–187.

(234) C. Böhm, M.; Gleiter, R.; L. Morgan, G.; Lusztyk, J.; Starowieyski, K. . *J. Organomet. Chem.* **1980**, *194*, 257–263.

(235) Paul, F.; Toupet, L.; Thépot, J. Y.; Costuas, K.; Halet, J. F.; Lapinte, C. *Organometallics* **2005**, *24*, 5464–5478.

(236) Atwood, C. G.; Geiger, W. E. *J. Am. Chem. Soc.* **1994**, *116*, 10849–10850.

(237) Robin, M. B.; Day, P. *Adv. Inorg. Chem. Radiochem.* **1968**, *10*, 247–422.

(238) Suzaki, Y.; Yoshigoe, Y.; Osakada, K. *J. Polym. Sci. Part A Polym. Chem.* **2013**, *51*, 3627–3635.

(239) Liu, K.; Ryan, D.; Nakanishi, K.; McDermott, A. *J. Am. Chem. Soc.* **1995**, *117*, 6897–6906.

(240) Bakhmutov, V. I.; Shpeizer, B. G.; Clearfield, A. *Magn. Reson. Chem.* **2006**, *44*, 861–867.

(241) Ennas, G.; Musinu, A.; Piccaluga, G.; Zedda, D.; Gatteschi, D.; Sangregorio, C.; Stanger, J. L.; Concas, G.; Spano, G. *Chem. Mater.* **1998**, *10*, 495–502.

(242) Bernas, H.; Campbell, I. A.; Fruchart, R. *J. Phys. Chem. Solids* **1967**, *28*, 17–24.

(243) Shylesh, S.; Schünemann, V.; Thiel, W. R. *Angew. Chemie - Int. Ed.* **2010**, *49*, 3428–3459.

(244) Kim, B. H.; Lee, N.; Kim, H.; An, K.; Park, Y. Il; Choi, Y.; Shin, K.; Lee, Y.; Kwon, S. G.; Na, H. Bin; Park, J.-G.; Ahn, T.-Y.; Kim, Y.-W.; Moon, W. K.; Choi, S. H.; Hyeon, T. *J. Am. Chem. Soc.* **2011**, *133*, 12624–12631.

(245) Tartaj, P.; Morales, M. a del P.; Veintemillas-Verdaguer, S.; Gonzalez-Carre o, T.; Serna, C. J. *J. Phys. D. Appl. Phys.* **2003**, *36*, R182–R197.

(246) Laurent, S.; Forge, D.; Port, M.; Roch, A.; Robic, C.; Vander Elst, L.; Muller, R. N. *Chem. Rev.* **2008**, *108*, 2064–2110.

(247) Fan, N.; Ma, X.; Ju, Z.; Li, J. *Mater. Res. Bull.* **2008**, *43*, 1549–1554.

(248) Chong, D.; Slote, J.; Geiger, W. E. *J. Electroanal. Chem.* **2009**, *630*, 28–34.

(249) Gericke, H. J.; Barnard, N. I.; Erasmus, E.; Swarts, J. C.; Cook, M. J.; Aquino, M. a S. *Inorg. Chim. Acta* **2010**, *363*, 2222–2232.

(250) Nemykin, V. N.; Rohde, G. T.; Barrett, C. D.; Hadt, R. G.; Sabin, J. R.; Reina, G.; Galloni, P.; Floris, B. *Inorg. Chem.* **2010**, *49*, 7497–7509.

(251) Nemykin, V. N.; Rohde, G. T.; Barrett, C. D.; Hadt, R. G.; Bizzarri, C.; Galloni, P.; Floris, B.; Nowik, I.; Herber, R. H.; Marrani, A. G.; Zanoni, R.; Loim, N. M. *J. Am. Chem. Soc.* **2009**, *131*, 14969–14978.

(252) Fourier, E.; Swarts, J. C.; Lorcy, D.; Bellec, N. *Inorg. Chem.* **2010**, *49*, 952–959.

(253) Swarts, J. C.; Nafady, A.; Roudebush, J. H.; Trupia, S.; Geiger, W. E. *Inorg. Chem.* **2009**, *48*, 2156–2165.

(254) Noviandri, I.; Brown, K. N.; Fleming, D. S.; Gulyas, P. T.; Lay, P. a; Masters, a F.; Phillips, L. *J. Phys. Chem. B* **1999**, *103*, 6713–6722.

(255) Ruiz, J.; Daniel, M. C.; Astruc, D. *Can. J. Chem.* **2006**, *84*, 288–299.

(256) Gritzner, G.; Kuta, J. *J. Pure Appl. Chem.* **1984**, 461–466.

(257) Nafady, A.; Geiger, W. E. *Organometallics* **2008**, *27*, 5624–5631.

(258) Golberg, D.; Bando, Y.; Huang, Y.; Terao, T. *ACS Nano* **2010**, *4*, 2979–2993.

(259) Shen, W.; Fan, W. *J. Mater. Chem. A* **2013**, 999–1013.

(260) Lee, Y. J.; Radovic, L. R. *Carbon N. Y.* **2003**, *41*, 1987–1997.

(261) Da Silva, R. R.; Torres, J. H. S.; Kopelevich, Y. *Phys. Rev. Lett.* **2001**, *87*, 1–4.

(262) Paraknowitsch, J. P.; Thomas, A. *Energy Environ. Sci.* **2013**, *6*, 2839.

(263) Matter, P. H.; Ozkan, U. S. *Catal. Letters* **2006**, *109*, 115–123.

(264) Bezerra, C. W. B.; Zhang, L.; Lee, K.; Liu, H.; Marques, A. L. B.; Marques, E. P.; Wang, H.; Zhang, J. *Electrochim. Acta* **2008**, *53*, 4937–4951.

(265) Tuaev, X.; Paraknowitsch, J. P.; Illgen, R.; Thomas, A.; Strasser, P. *Phys. Chem. Chem. Phys.* **2012**, *14*, 6444.

(266) Yun, Y. S.; Kim, D.; Park, H. H.; Tak, Y.; Jin, H. J. *Synth. Met.* **2012**, *162*, 2337–2341.

(267) Sevilla, M.; Valle-Vigõn, P.; Fuertes, A. B. *Adv. Funct. Mater.* **2011**, *21*, 2781–2787.

(268) Hao, G. P.; Li, W. C.; Qian, D.; Lu, A. H. *Adv. Mater.* **2010**, *22*, 853–857.

(269) Jeon, J. W.; Sharma, R.; Meduri, P.; Arey, B. W.; Schaef, H. T.; Lutkenhaus, J. L.; Lemmon, J. P.; Thallapally, P. K.; Nandasiri, M. I.; McGrail, B. P.; Nune, S. K. *ACS Appl. Mater. Interfaces* **2014**, *6*, 7214–7222.

(270) Chen, X. Y.; Xie, D. H.; Chen, C.; Liu, J. W. *J. Colloid Interface Sci.* **2013**, *393*, 241–248.

(271) Xu, B.; Zheng, D.; Jia, M.; Cao, G.; Yang, Y. *Electrochim. Acta* **2013**, *98*, 176–182.

(272) Li, T.; Yang, G.; Wang, J.; Zhou, Y.; Han, H. *J. Solid State Electrochem.* **2013**, *17*, 2651–2660.

(273) Chen, Z.; Higgins, D.; Yu, A.; Zhang, L.; Zhang, J. *Energy Environ. Sci.* **2011**, *4*, 3167.

(274) Jaouen, F.; Proietti, E.; Lefèvre, M.; Chenitz, R.; Dodelet, J.-P.; Wu, G.; Chung, H. T.; Johnston, C. M.; Zelenay, P. *Energy Environ. Sci.* **2011**, *4*, 114.

(275) Chen, T.; Pan, L.; Loh, T. A. J.; Chua, D. H. C.; Yao, Y.; Chen, Q.; Li, D.; Qin, W.; Sun, Z. *Dalton Trans.* **2014**, *43*, 14931–14935.

(276) Chen, X. Y.; Chen, C.; Zhang, J. Z.; Xie, dong H. *Powder Technology* **2013**, *246*, 201–209.

(277) Silverstein, R. M.; Ryskiewicz, E. E.; Willard, C.; Koehler, R. C. *J. Org. Chem.* **1955**, *20*, 668–672.

(278) Ryppa, C.; Senge, M. O.; Hatscher, S. S.; Kleinpeter, E.; Wacker, P.; Schilde, U.; Wiehe, A. *Chem. - A Eur. J.* **2005**, *11*, 3427–3442.

(279) Göring, M.; Seifert, a.; Schreiter, K.; Müller, P.; Spange, S. *Chem. Commun.* **2014**, *50*, 9753–9756.

(280) Modak, A.; Mondal, J.; Bhaumik, A. *Appl. Catal. A Gen.* **2013**, *459*, 41–51.

(281) Abraham, R. J.; Lapper, R. D.; Smith, K. M.; Unsworth, J. F. *J. Chem. Soc. Perkin Trans. 2* **1974**, 1004.

(282) Choy, J.; Jaime-Figueroa, S.; Jiang, L.; Wagner, P. *Synth. Commun.* **2008**, *38*, 3840–3853.

(283) Bellur, E.; Görls, H.; Langer, P. *J. Org. Chem.* **2005**, *70*, 4751–4761.

(284) Gossauer, A.; Neidhart, W.; Scott, A. I. *J. Chem. Soc. Chem. Commun.* **1983**, *94*, 883.

(285) Wang, H.; Zhang, C.; Liu, Z.; Wang, L.; Han, P.; Xu, H.; Zhang, K.; Dong, S.; Yao, J.; Cui, G. *J. Mater. Chem.* **2011**, *21*, 5430.

(286) Pillai, S. K. T.; Kretschmer, W. P.; Denner, C.; Motz, G.; Hund, M.; Fery, A.; Trebbin, M.; Förster, S.; Kempe, R. *Small* **2013**, *9*, 984–989.

8 Appendix

8.1 Abstracts und Supporting Information

8.1.1 Kapitel 3.1

A Convenient Light Initiated Synthesis of Silver and Gold Nanoparticles using a Single Source Precursor

Christian Schliebe[a], Kun Jiang[b], Steffen Schulze[c], Michael Hietschold[c], Wen-Bin Cai[b] and Heinrich Lang*[a]

[a] Faculty of Natural Sciences, Institute of Chemistry, Inorganic Chemistry, Technische Universität Chemnitz, Straße der Nationen 62, 09111 Chemnitz, Germany. Fax: +49371531-21219; Tel: +49371-53121210; E-mail: heinrich.lang@chemie.tu-chemnitz.de
[b] Shanghai Key Laboratory for Molecular Catalysis and Innovative Materials, and Department of Chemistry, Fudan University, Shanghai 200433, China.
[c] Authors, to whom correspondece pretaining TEM studies should be adressed: Faculty of Natural Sciences, Department of Solid Surfaces Analysis, Technische Universität Chemnitz, Reichenhainer Strasse 70, 09126 Chemnitz, Germany.

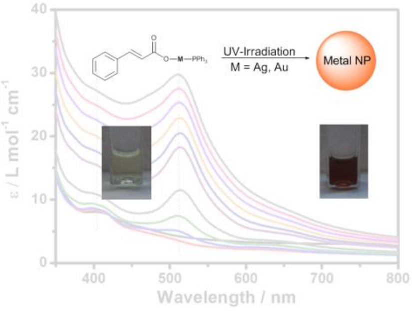

Abstract

A photochemical approach is reported for the straightforward synthesis of silver and gold nanoparticles using a single source precursor under very mild conditions.

8.1.2 Kapitel 3.2

Twin Polymerisation: A Unique and Efficient Tool for Supporting Silver Nanoparticles on Highly Porous Carbon and Silica

Christian Schliebe,[a] Thomas Gemming,[b] and Heinrich Lang*[a]

[a]Faculty of Natural Sciences, Institute of Chemistry, Inorganic Chemistry, Technische Universität Chemnitz, 09107 Chemnitz, Germany. Fax.: +49371531-21219; Phone: +40371531-21210; Email: heinrich.lang@chemie.tu-chemnitz.
[b]Author, to whom correspondence pertaining STEM studies should be addressed: IFW Dresden, Helmholtzstraße 20, 01069 Dresden, Germany. Phone: +49351-4659298; Email: t.gemming@ifw.dresden.de.

Abstract

A convenient approach for the straightforward synthesis of highly dispersed silver nanoparticles (below 5 nm) in a carbon or silicon dioxide matrix through twin polymerization is reported. The obtained mainly microporous carbon (type I isotherm) and mesoporous silica materials (type IV isotherm) exhibit a rather high surface area (carbon = 1034 $m^2\,g^{-1}$, SiO_2 = 666 $m^2\,g^{-1}$).

8.1.3 Kapitel 3.3

Zirconium and Hafnium Twin Monomers for Mixed Oxides

Christian Schliebe,[a] Thomas Gemming,[b] Julian Noll,[a] Lutz Mertens,[c] Michael Mehring,[c] Andreas Seifert[d], Stefan Spange[d] and Heinrich Lang[a]*

[a]Technische Universität Chemnitz, Faculty of Natural Sciences, Institute of Chemistry, Inorganic Chemistry, 09107 Chemnitz, Germany. Fax.: +49 (0)371-531-21219; Phone: +49 (0)371-531-21210; Email: heinrich.lang@chemie.tu-chemnitz.

[b]Author, to whom correspondence pertaining STEM studies should be addressed: IFW Dresden, Helmholtzstraße 20, 01069 Dresden, Germany. Phone: +49 (0)351-465-9298; Email: t.gemming@ifw.dresden.de

[c]Technische Universität Chemnitz, Faculty of Natural Sciences, Institute of Chemistry, Coordination Chemistry, 09107 Chemnitz, Germany.

[d]Technische Universität Chemnitz, Faculty of Natural Sciences, Institute of Chemistry, Polymer Chemistry, 09107 Chemnitz, Germany.

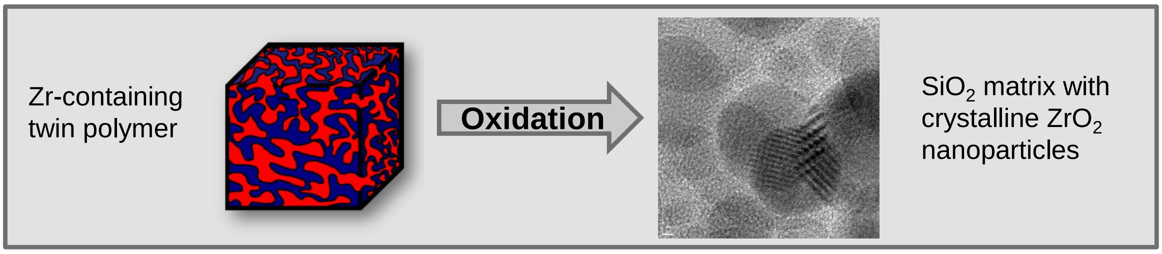

Abstract

The synthesis of Zr and Hf twin monomers of type $[M(2\text{-}OCH_2{}^cC_4H_3O)_4(x\ HOCH_2{}^cC_4H_3O)]$ (**3**, M = Zr, x = 0; **4**, M = Hf, x = 1) and $M[(2\text{-}OCH_2\text{-}C_6H_4O)_2(2\text{-}HOCH_2\text{-}C_6H_4OH)]$ (**5**, M = Zr; **6**, M = Hf) by reacting $M(OR)_4$ (M = Zr, R = $^nC_3H_7$, **1**; M = Hf, R = $^nC_4H_9$, **2**) with 2-furanmethanol or 2-hydroxybenzyl alcohol is discussed. Complexes **3**-**6** were homo-polymerized under acidic condition. Additionally, **5** and **6** were copolymerized with 2,2'-spiro-bi[4H-1,3,2-benzodioxasiline] (= SBS). Under acidic conditions SBS forms a phenolic resin/SiO_2 nano-structured material. The resulting hybrid materials from the homo-polymerization of **3**-**6** and the copolymerized materials from **5** and **6** were characterized by standard solid state analytics. The in-

organic lattice of the MO_2 materials from the homo-polymerized complexes **3**–**6** and SiO_2/MO_2 from the copolymerization of **5** and **6** with SBS was obtained by air-oxidation. The oxide materials were characterized by XRPD and EDX proofing their identity. The inner surface area was determined by N_2 adsorption/desorption studies revealing surface areas of 100 m^2/g for MO_2. The mixed oxides SiO_2/MO_2 were additionally investigated by DSC and VT-XRPD to study the thermal behavior. It was found that crystallization of tetragonal MO_2 nanoparticles is characteristic within the SiO_2 matrix, while higher sintering temperatures caused crystallization of the SiO_2 lattice.

8.1.4 Kapitel 3.4

Die diesem Kapitel zu grundliegenden Ergebnisse noch nicht Online verfügbar sind finden sich im Anhang des Abstracts die Supporting Electronic informations wieder.

Metal Nanoparticle-loaded Porous Carbon Hollow Spheres by Twin Polymerization

Christian Schliebe,[a] Tobias Graske, [a] Thomas Gemming,[b] and Heinrich Lang[a]*

[a]Technische Universität Chemnitz, Faculty of Natural Sciences, Institute of Chemistry, Inorganic Chemistry, 09107 Chemnitz, Germany. Fax.: +49 (0)371-531-21219; Phone: +49 (0)371-531-21210; Email: heinrich.lang@chemie.tu-chemnitz.

[b]Author, to whom correspondence pertaining STEM studies should be addressed: IFW Dresden, Helmholtzstraße 20, 01069 Dresden, Germany. Phone: +49 (0)351-465-9298; Email: t.gemming@ifw.dresden.de.

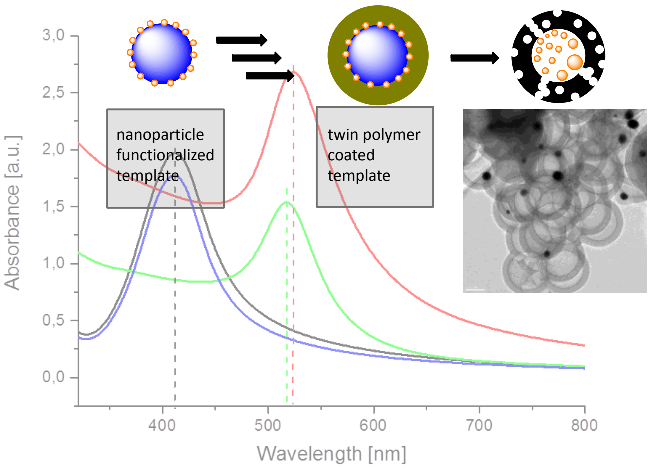

Abstract

The generation of silver and gold nanoparticle-encapsulated hollow carbon spheres (= HCS) by twin polymerization is reported. Silica spheres with different diameters (Aerosil® AS90, d ~ 20 nm; Aerosil® OX50, d ~ 40 nm; Stöber particles, d ~ 200 nm) were coated with metal carboxylates $[AgO_2C(CH_2OCH_2)_3H]$ (**1**) or $[(PPh_3)AuO_2C(CH_2OCH_2)_3H]$ (**2**). Thermal treatment of these templates produced the respective metal nanoparticle-functionalized systems, which were characterized by

X-ray powder diffraction (= XRPD) and transmission electron microscopy (= TEM). The plasmon resonance of the surface-bonded particles was determined by using UV-Vis spectroscopy showing absorptions at 412 nm for silver and 524 nm for gold. The thus metal-modified templates were then coated with a twin polymer layer as result of the acid-catalyzed twin polymerization of 2,2‘-spiro-bi[4H-1,3,2-benzodioxasiline] (= SBS) (**3**). This coating consists of a phenolic resin and *in situ* formed silicon dioxide nano-cluster. After carbonization and removal of the SiO_2 phase by refluxing with a sodium hydroxide solution, the appropriate metal-loaded HCS were obtained. The thus prepared carbon materials were characterized by XRPD, electron microscopy and nitrogen adsorption-desorption isotherms. Mainly micro-porous materials (IUPAC Type I) were obtained with a surface area between 910 – 1110 m^2/g. These HCS materials were used on the catalytic reduction of methylene blue and 4-nitrophenol, respectively, proving the accessibility of the incorporated nanoparticles. A size dependent influence of the used carbon hull was found.

Electronic Supporting Information

General

Aerosil OX50 and AS90 were provided by the Overlack AG (Leipzig). The metal carboxylates $[AgO_2C(CH_2OCH_2)_3H]$ (**1**),[112] $[(PPh_3)AuO_2C(CH_2OCH_2)_3H]$ (**2**)[113] and 2,2‘-spiro-bi[4H-1,3,2-benzodioxasiline] (= SBS)[63] were prepared according to literature procedures[184]. X-ray powder diffraction analyses were carried out with a STOE-STAD-IP diffractometer (Cu K_α $\lambda = 0.154$ nm). SEM images and EDX analyses were performed with a Phillips NanoNovaSEM. TEM images were recorded with a Fecnai FC20 equipment with 200 kV accelerating voltage. Gas absorption-desorption measurements were carried out using an Autosorb IQ2 system. Thermal analyses were performed with a Mettler Toledo TGA/DSC1/1600 equipment with a MX1 scale. All thermal operations were carried out in a Carbolite Tube Furnace MTF 12/38/400.

Experimental Section

Ag-Nanoparticles generation. In a typical procedure, 0.28 g (0.975 mmol) of **1** were diluted in 150 mL of acetonitrile and 2.0 g of the specific template (AS90, OX50 or Stöber Particles) was added in a single portion and the mixture was stirred for 30 min at ambient temperature. Afterwards, all volatiles were evaporated under reduced pressure and the loaded template was transferred to a tube furnace and heated under a continuous flow of argon for 1 h at 250 °C, whereby the initial off-white solid has changed his colour to bright yellow.

Au-Nanoparticle generation. The preparation follows the previous described method for the Ag particles and a red coloured product was obtained after thermal treatment (metal precursor **2**: 0.62 g, 0.975 mmol).

Template coating with twin polymer. 1.0 g of the metal nanoparticle-loaded template was coarsely grinded in an agate mortar and then suspended in 200 mL of dichloromethane and sonicated until a homogenous suspension was achieved. Afterwards, 0.162 mL (2.5 mmol) of methanesulfonic acid was added in a single portion and the mixture was stirred for 15 min at ambient temperature. Then, all volatiles were evaporated *in vacuo* and the remaining solid was suspended in toluene (200 mL) and sonicated until a homogenous suspension was formed. To this mixture, 2.0 g (7.3 mmol) of 2,2‘-spiro-bi[4H-1,3,2-benzodioxasiline] dissolved in 50 mL of toluene were added drop-wise. After 15 min of stirring at ambient temperature the suspension turned deep violet indicating the beginning of the twin polymerization process and stirring was conducted for 8 h, whereby the hybrid material-coated templates precipitated. The solid was collected by filtration and washed thrice with dichloromethane (50 mL each) and were then dried *in vacuo*, yielding 2.5 – 3.0 g of a pink colored solid.

Carbonization and template removal. In a typical procedure, 2.0 g of the twin polymer-coated templates were placed in a tube furnace and carbonized at 800 °C (50 K/min) for 15 min under a continuous flow of argon. The removal of the silica template and SiO_2 component of the twin polymer was achieved by refluxing the carbonized material in 50 mL of a 5 M NaOH solution for 8 h. Afterwards, the SiO_2-free capsules were filtered off and washed with hot water (at least 300 mL until pH ~ 7 is reached) and then with 50 mL of deionized water followed by 30 mL of acetone and 50 mL of diethyl ether. The metal nanoparticle-loaded carbon hollow spheres where then dried *in vacuo*.

(1) Steffan, M.; Jakob, A.; Claus, P.; Lang, H. *Catal. Commun.* **2009**, *10*, 437–441.

(2) Tuchscherer, A.; Schaarschmidt, D.; Schulze, S.; Hietschold, M.; Lang, H. *Inorg. Chem. Commun.* **2011**, *14*, 676–678.

(3) Spange, S.; Kempe, P.; Seifert, A.; Auer, A. A.; Ecorchard, P.; Lang, H.; Falke, M.; Hietschold, M.; Pohlers, A.; Hoyer, W.; Cox, G.; Kockrick, E.; Kaskel, S. *Angew. Chem. Int. Ed. Engl.* **2009**, *48*, 8254–8258.

(4) Struppert, T.; Jakob, A.; Heft, A.; Grünler, B.; Lang, H. *Thin Solid Films* **2010**, *518*, 5741–5744.

8.1.5 Kapitel 3.5

Si(OCH_2Fc)$_4$: Synthesis, Electrochemical Behavior and Twin Polymerization

Christian Schliebe,[a] Ulrike Pfaff,[a] Thomas Gemming,[b] Charles Lochenie,[c] Birgit Weber[c] and Heinrich Lang[a]*

[a]Technische Universität Chemnitz, Faculty of Natural Sciences, Institute of Chemistry, Inorganic Chemistry, D-09107 Chemnitz, Germany. Fax.: +49 (0)371-531-21219; Phone: +49 (0)371-531-21210; Email: heinrich.lang@chemie.tu-chemnitz.de
[b]Author, to whom correspondence pertaining STEM studies should be addressed: IFW Dresden, Helmholtzstraße 20, D-01069 Dresden, Germany. Phone: +49 (0)351-465-9298; Email: t.gemming@ifw.dresden.de
[c]Authors, to whom correspondence pertaining magnetical characterization should be addressed: Universität Bayreuth, Institute of Chemistry, Inorganic Chemistry II, D-95440 Bayreuth, Germany.
Keywords: Twin polymerization, Hybrid material, Iron(III) oxide nanoparticles, Superparamagnetism, Electrochemistry

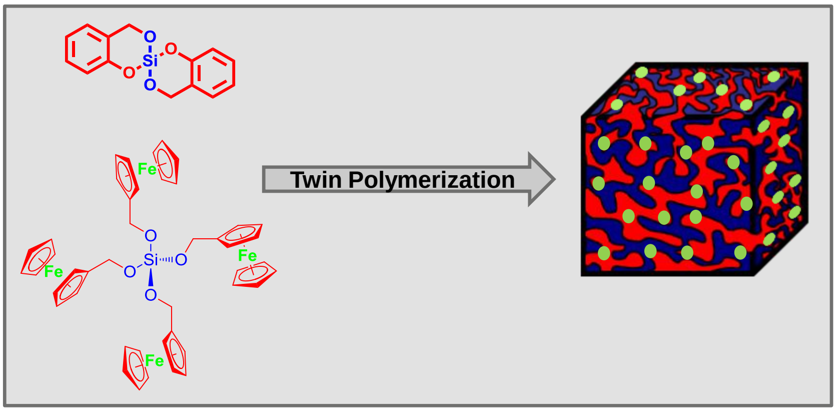

Abstract

The preparation and twin polymerization of the twin monomer Si(OCH_2Fc)$_4$ (Fc = Fe(η^5-C_5H_4)(η^5-C_5H_5)) (**2**) by the reaction of $FcCH_2OH$ (**1**) with $SiCl_4$ in presence of pyridine is reported. The electronic properties of **2** were investigated by cyclovoltammetry, square-wave voltammetry and UV-Vis/NIR spectroelectrochemistry showing a redox separation caused by electro-static repulsion. A thermally induced condensation of **2** is characteristic as evidenced by differential scanning calorimetry and thermogravimetry-coupled mass-spectrometry. Upon heating **2** to 210 °C, twin polymerization occurred and a hybrid material was formed showing similarities with known systems derived from 2,2‘-spiro-bi[4H-1,3,2-benzodioxasiline] (= SBS) like the nanopatterning of the formed silicon dioxide clusters, typical for twin polymerization. Elec-

tron microscopy of this material revealed the absence of the typical micro-structuring found for other twin polymers and hence the herein presented system can be characterized as a borderline system, when compared to known twin monomers such as SBS. The copolymerization of **2** and SBS afforded a hybrid material from which porous carbon or silica materials containing iron oxide nanoparticles could be obtained. The oxidation state of the incorporated particles was examined by Mössbauer experiments, confirming that only Fe(III) was incorporated within the porous carbon and silica materials, respectively. The preparation of iron oxide containing porous carbon capsules was achieved by applying the mixture of **2** and SBS to silicon dioxide spheres (d = 200 nm). After twin polymerization and carbonization, porous carbon capsules with incorporated iron oxide nano-structures were obtained.

8.1.6 Kapitel 3.6

Nitrogen-containing Porous Carbon Materials by Twin Polymerization

Christian Schliebe,[a] Julian Noll,[a] Thomas Gemming,[b] Andreas Seifert[c], Stefan Spange[c] and Heinrich Lang[a]*

[a]Technische Universität Chemnitz, Faculty of Natural Sciences, Institute of Chemistry, Inorganic Chemistry, 09107 Chemnitz, Germany. Fax.: +49 (0)371-531-21219; Phone: +49 (0)371-531-21210; Email: heinrich.lang@chemie.tu-chemnitz.de
[b]Author, to whom correspondence pertaining STEM studies should be addressed: IFW Dresden, Helmholtzstraße 20, 01069 Dresden, Germany. Phone: +49 (0)351-465-9298; Email: t.gemming@ifw.dresden.de
[c]Authors, to whom correspondence pertaining solid state NMR studies should be addressed: Technische Universität Chemnitz, Faculty of Natural Sciences, Institute of Chemistry, Polymer Chemistry, 09107 Chemnitz, Germany.

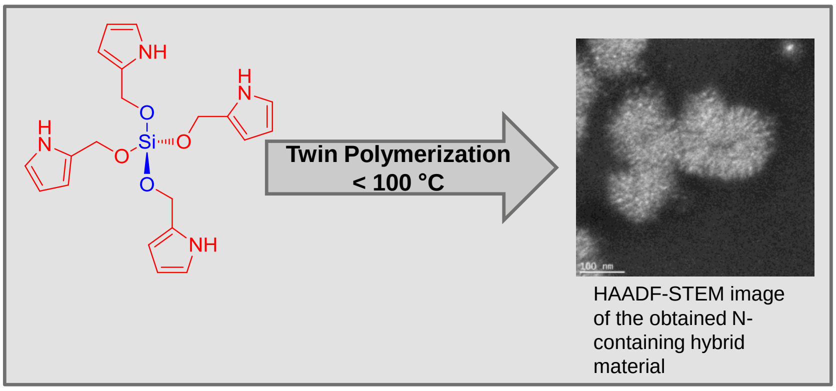

HAADF-STEM image of the obtained N-containing hybrid material

Abstract

The preparation of $Si(OCH_2{}^{c}C_4H_3NR)_4$ (R = Me (**5**), H (**6**)) by the reaction of aldehydes 2-CHO-$^{c}C_4H_3NR$ (R = Me (**1**), H (**2**)) with $SiCl_4$ in the ratio of 4:1 in presence of NEt_3 is described. The thermal behavior of twin monomers **5** and **6** was investigated by thermogravimetry and differential scanning calorimetry. Compound **6** shows with 93 °C the lowest polymerization temperature for twin monomers reported so far. In addition to the thermal induced twin polymerization of **5** and **6**, the acidic-initiation and copolymerization with 2,2'-spiro-bi[4H-1,3,2-benzodioxasiline] was investigated. The resulting hybrid materials were characterized by ^1H, $^{13}C\{^1H\}$ and $^{29}Si\{^1H\}$ solid state NMR spectroscopy confirming the transformation of the $SiOCH_2$ moieties in to CH_2 groups enabling the formation of the respective polymers. These results are supported by HAADF-STEM studies, showing the typical microstructuring of a twin

polymer. Furthermore, nitrogen-containing porous carbon materials with a surface area between 200 and 800 m^2/g and a nitrogen content of up to 9.1 % were obtained. The chemical nature of the incorporated nitrogen was investigated by XPS spectroscopy, revealing that mostly pyrrolic nitrogen is observed, but also pyridinic species are present.

8.2 Lebenslauf

PERSÖNLICHE DATEN

Name: Dipl.-Chem. Christian Schliebe
Geburtsdatum: 20.03.1986
Geburtsort: Wolfen
Staatsangehörigkeit: deutsch
Familienstand: ledig

PROMOTIONSSTUDIUM AN DER TECHNISCHE UNIVERSITÄT CHEMNITZ

09/2011 – 07/2015	Promotionsstudium am Lehrstuhl für Anorganische Chemie (Prof. Dr. H. Lang), angestrebter Abschluss Dr. rer. nat.
Thema:	*„Zwillingspolymerisation in Gegenwart von Übergangsmetallcarboxylaten / Darstellung neuer Zwillingsmonomere.“*
Lehrtätigkeit:	Betreuung von Grund- und Fortgeschrittenenpraktika, Vorbereitung und Durchführung von Schauexperimenten.

STUDIUM UND SCHULAUSBILDUNG

10/2010 – 08/2011	Diplomarbeit am Lehrstuhl für Anorganische Chemie (Prof. Dr. H. Lang) ***„****Thiole zur Herstellung von SAMs“* . Abschluss: Diplom-Chemiker.
10/2006 – 10/2010	Studium der Chemie an der TU Chemnitz mit den Schwerpunkten: Organische-, Anorganische-, Metallorganische-, Physikalische- und Polymerchemie.
07/2009 – 09/2009	Auslandspraktikum an der Durham University (UK), in der Arbeitsgruppe von Prof. J. W. Steed, Schwerpunkt: Festkörpersynthese/Mechanochemie.
09/1999 – 06/2005	Erwerb der Allgemeinen Hochschulreife, „Anne-Frank-Gymnasium“ Sandersdorf.

8.3 Referenzen

8.3.1 Publikationen

1. C. Schliebe, K. Jiang, S. Schulze, M. Hietschold, W.-B. Cai, H. Lang, *Chem. Commun.* **2013**, *49*, 3991–3993.
2. C. Schliebe, T. Gemming, L. Mertens, M. Mehring, H. Lang, *Eur. J. Inorg. Chem.* **2014**, 3161–3163.
3. C. Schliebe, T. Gemming, L. Mertens, M. Mehring, A. Seifert, S. Spange, H. Lang, *ChemPlusChem*. **2014**, DOI: 10.1002/cplu.201402338.
4. C. Schliebe, T. Graske, T. Gemming, L. Mertens, H. Lang, *J. Mater. Chem. A*. **2015**, submitted.
5. C. Schliebe, U. Pfaff, T. Gemming, C. Lochenie, B. Weber and H. Lang, *J. Organomet. Chem.* **2015**, submitted.
6. C. Schliebe, J. Noll, T. Gemming, A. Seifert, S. Spange and H. Lang, *ChemPlusChem.* **2015**, in preparation.
7. Inkjet Printing of Group-11 Metal Structures (Buchkapitel). C. Gäbler, C. Schliebe, D. Adner, T. Blaudeck, A. Hildebrandt und H. Lang, Nova Science Publishers, Hauppauge, N. Y. (USA), in Comprehensive Guide for Nanocoatings Technology, Volume 1: Deposition and Mechanism, 2015, im Druck. ISBN: 978-1-63482-447-7.

8.3.2 Vorträge

SP7: Poröse Materialien beladen mit Metall-/Metalloxid-Nanopartikeln über Zwillings(co)polymerisation
C. Schliebe, A. Jakob, H. Lang, Eröffnungskolloquium Zwillingspolymerisation, 15.-16.12.2011, Chemnitz.

Twin polymerization of ferrocenes.
C. Schliebe, H. Lang, 13th Ferrocene Colloquium, 22.–24.02.2015, Leipzig.

8.3.3 Poster

Simultane Polymerisation von Zwillingsmonomeren mit Übergangsmetallverbindungen zu porösen Materialien beladen mit Metall-/ Metalloxid-Nanopartikeln.
C. Schliebe, A. Jakob, H. Lang, Eröffnungskolloquium Zwillingspolymerisation, 15.-16.12.2011, Chemnitz.

Hiermit erkläre ich, dass ich die vorliegende Arbeit selbstständig angefertig, nicht anderweitig zu Prüfungszwecken vorgelegt und keine anderen als die angegebenen Hilfsmittel verwendet habe. Sämtliche wissentlich verwendete Textausschnitte, Zitate oder Inhalte anderer Verfasser wurden ausdrücklich als solche gekennzeichnet

Chemnitz, den 07.09.2015

Christian Schliebe